Characterization and Modeling of Highly Anisotropic Materials Behavior: Application to Battery Separators

by

Mustapha Makki

A dissertation submitted in partial fulfillment
of the requirements for the degree of
Doctor of Philosophy
(Industrial and Systems Engineering)
in the University of Michigan-Dearborn
2023

Doctoral Committee:

Associate Professor Georges Ayoub, Co-Chair
Associate Professor Cheol Lee, Co-Chair
Professor Ghassan Kridli
Associate Professor German Reyes-Villanueva

Mustapha J. Makki

mumakki@umich.edu

ORCID iD: 0000-0001-6504-4635

Dedication

This dissertation is dedicated to my incredible parents, Jamal Makki and Siham Rahal. Without their endless love, support, and encouragement this work would not have been possible.

Acknowledgements

This thesis has been accomplished under the supervision of Dr. Georges Ayoub of the College of Engineering and Computer Science at the University of Michigan – Dearborn. Dr. Ayoub first accepted me as a master's student during my time at the American University of Beirut. He worked with me closely and steered me in the right direction to strengthen my knowledge in research. It was an honor and a pleasure joining him at the University of Michigan – Dearborn for my PhD. I am immensely grateful to Dr. Ayoub for his unlimited support and guidance during the past four years. He helped me grow as a scientist and researcher and has taught me invaluable skills during my PhD. I appreciate his help during our weekly meetings and long sessions of scientific debate which were key to my success during my studies.

I would like to thank Dr. Cheol Lee for serving as a co-chair on my committee. He supported me and offered me suggestions and feedback. His input was very helpful and improved the quality of work I was able to do.

I would like to extend my deepest appreciation to Dr. German Reyes-Villanueva and Dr. Ghassan Kridli for taking the time to serve on my committee and thoroughly examining my work.

Finally, my very profound gratitude goes to my family. Special thanks to my wife Ruba Khalifeh for her continuous support and encouragement through my years of study.

Table of Contents

List of Tables

List of Figures

List of Appendices

Abstract

Separators are microporous films sandwiched between the anode and cathode to prevent physical contact and allow the exchange of ions between the two electrodes. Degradation in the separator occurs under charge and discharge cycles affecting its mechanical properties. Failure in this component can cause internal shorting of the battery or thermal runaway. Hence, an accurate characterization and modelling of the separator's mechanical behavior and induced degradation under different charge and discharge cycles is essential for optimal design and life cycle operation of commercial lithium-ion batteries.

In chapter 2, the mechanical behavior of a pristine polyethylene separator was investigated. An anisotropic continuum damage coupled elastic-hyperelastic-viscoplastic model is developed in the framework of the large deformation theory to capture the mechanical and fracture behavior of battery separators. A robust implicit integration scheme is developed then the model is implemented as a user-defined material subroutine (UMAT) in commercial finite-element software to solve boundary-value problems. The capability of the proposed model to predict the anisotropic mechanical behavior up to fracture for two different types of battery separators highlights the versatility of the proposed modeling approach. The model results showed a good agreement with the experimental data. Moreover, the model was able to predict the failure of the polyethylene separators under different loading conditions.

In chapter 3, the effect of cyclic fast charging on the mechanical and physico-chemical properties of the polyethylene separator is investigated. Six lithium-ion battery pouch cells were subjected to cyclic fast charging conditions at 4C (fast) charge rate and 0.5C discharge rate up to 400, 800, and 1600 cycles. Once the cyclic fast charging was completed, the battery pouch cells were fully discharged and carefully disassembled. The physical and chemical microstructural properties of pristine and cycled separators were investigated using scanning electron micrographs (SEM), Xray photoelectron spectroscopy (XPS) and Fourier Transform Infrared Spectroscopy (FTIR). Additionally, the mechanical behavior of the pristine and cycled separators was also investigated using uniaxial tensile tests and biaxial punch tests. While the XPS and FTIR analysis of the cycled separator surfaces did not reveal the presence of chemical degradation, the mechanical properties presented a decrease in the toughness and ductility with increased number of charging cycles. A thorough discussion of the cycled separator degradation mechanisms is provided by combining the results of our analysis and of those reported in the literature.

In chapter 4, the thermal and mechanical behavior of an NMC 622 pouch cell in a battery pack array is characterized and discussed under fast charging conditions. A novel battery cell model for prediction of stress distribution inside a battery pouch cell during fast charging is presented. First, a Multiphysics model is developed to predict the core temperature of the battery, the loads applied, and the displacement behavior in the battery pack array. The thermal and mechanical behavior of an NMC 622 pouch cell in a battery pack array is characterized and discussed under fast charging conditions. A robust parameter identification scheme is proposed to determine the model parameters based on experimental data. The first principal stress in the separator was shown to be around 70 MPa. Creep and fatigue tests were conducted on the separator to generate deformation

damage. The results show that 70 MPa can cause significant damage in the separator after repeated fast charging.

The conducted studies helped in expanding the knowledge about the degradation mechanisms in separators during charge and discharge cycles. Additionally, the continuum damage model and Multiphysics model can provide designers with predictive tools to improve the battery design, life span and safety.

Chapter 1 Introduction

Small portable electronic devices such as smartphones, laptops rely widely on the use of lithium-ion (Li-ion) batteries. Furthermore, Li-ion batteries are the dominantly used technology in electrical vehicles (Iclodean et al., 2017), since they present numerous advantages compared to other battery counterparts such as high energy density, high specific energy, and large number of charge-discharge cycles (Alaoui, 2013; Gerssen-Gondelach and Faaij, 2012; Lu et al., 2013; Lukic et al., 2008). However, ageing mechanisms in Li-ion batteries under charge-discharge cycles poses a challenge for researchers/manufacturers due to safety concerns and battery performance. Lithium-ion batteries consist of an anode, cathode, separator, current collectors, and electrolyte wrapped in a shell casing or plastic cover. Aging mechanisms occurring in the positive and negative electrodes have been the case of study of many researchers (Agubra and Fergus, 2013; Barré et al., 2013; Lin et al., 2015; Vetter et al., 2005), but only recently researchers started studying the degradation of the battery separator during charge-discharge cycles, since failure in this critical component can cause internal shorting of the battery or thermal runaway. Zhang et al., (2017) reported a decrease in strain to failure in separators with increased number of charge-discharge cycles.

Separators in commercial lithium-ion batteries are microporous films consisting of a polymeric membrane such as polyethylene or polypropylene, inorganic composite membranes, and non-woven fabric mats (Zhang, 2007). Polyolefin membranes are the most widely used due to many advantages such as low cost, high safety and high performance (Linden and Reddy, 2002;

Zhang, 2007). Polyolefin membranes are semi-crystalline polymers that have an interconnecting amorphous and crystalline microstructure. The separator is sandwiched between the anode and the cathode typically in spiral wound or prismatic design to prevent physical contact while its porous structure allows the exchange of ions through the liquid electrolyte filled in its pores (Arora and Zhang, 2004). Separators should be chemically inactive, and mechanically robust to withstand large tensile deformation applied during battery assembly and charge and discharge cycles (Huang, 2011). Indeed, the lithium insertion electrochemical process causes large volumetric expansion of the electrode materials (Timmons and Dahn, 2007), which then causes large deformation of the separator. As a result of the chemical reaction, the battery is subjected to a temperature change causing thermal stresses arising from materials with different coefficients of thermal expansion (Shi et al., 2011). Hence, during charge-discharge cycles, both aforementioned processes induce a mechanical and thermal cyclic loading on the battery component and more specifically on the separator. The possible aging mechanisms in the battery separator are divided into: (1) Oxidation due to the electrochemical reaction at the anode-separator or cathode-separator interfaces, (2) thermal aging causing chain scission or cross-linking due to the temperature changes in the battery components, (3) mechanical fatigue due to the expansion and reduction in size of the electrodes causing cyclic stresses. An investigation of these possible aging mechanisms is needed to find which aging mechanism is dominant among the others.

In this chapter, we focus on the properties, manufacturing process, morphology and mechanical behavior of microporous polymeric films up to the present state of knowledge in the field. In order to understand polymeric separator's morphology and mechanical behavior, a literature review about polymer's morphology, mechanical behavior and constitutive models is first given. Furthermore, the chapter expands on the constitutive models implemented in literature

to describe microporous films mechanical behavior. Finally, the problem statement and research objectives are listed.

1.1 Review of Semi-Crystalline Polymers

Semi-crystalline polymers are being used in biomedical, automotive, electronics and many other fields. This wide usage is related to their semi-crystalline nature that allows their mechanical behavior to range between a rubber like material (elastomer) at low crystallinities, and thermoplastic at high crystallinity (G Ayoub et al., 2011).

1.1.1 Morphology of Thermoplastic Polymers

Semi-crystalline polymers are composed of long chains formed by a repeating monomer unit joined by strong covalent bonding. Weak van der Waals bonds are also present between molecules. The bonds along those long chains can bend and rotate in three dimensions, hence creating a lot of twisting. An example of this shown in Figure 1.1 for a long chain. Bending, and kinks leads to intertwining and entanglements between different chains.

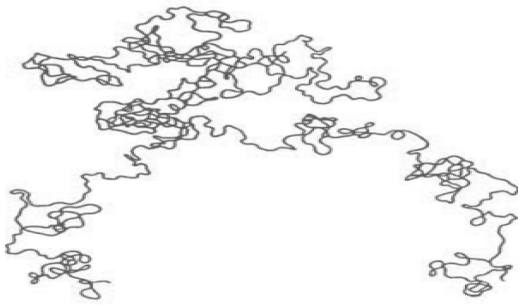

Figure 1.1: Long polymer chain showing twisting and kinks (Callister and Rethwisch, 1996).

Semi-crystalline polymers can have different molecular structure which significantly affects their mechanical properties. These molecular structures shown in Figure 1.2 include: (a) Linear polymers which have long chains that do not have any covalent bonding with other chains,

(b) branched polymers in which long chains have side branches connected to them, (c) crosslinked polymers in which long chains have adjacent chains connected to other long chains, and (d) network polymers in which a monomer forms covalent bonding with other monomers.

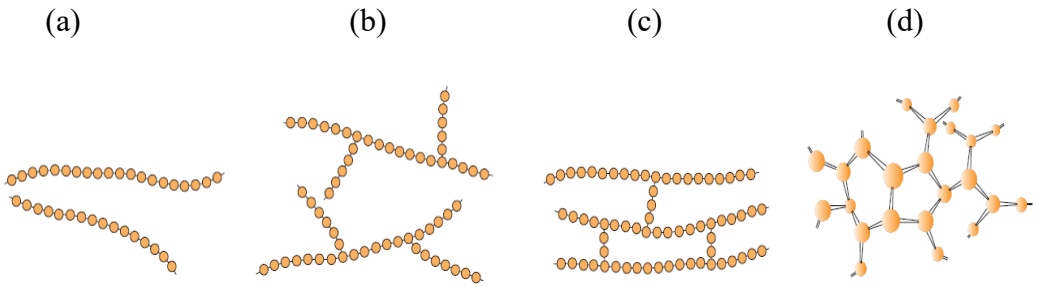

Figure 1.2:Semi-crystalline polymers different molecular structures: (a) Linear, (b) Branched, (c) crosslinked, and (d) Network (Callister and Rethwisch, 1996).

Semi-crystalline polymers have a crystallinity ratio ranging between 5% and 95%, which results in a wide range of mechanical properties. The microstructure of semi-crystalline polymers combines two solid phases: (1) A crystalline phase consisting of an ordered macromolecular structure where chains folds back and forth creating a lamellae and (2) an amorphous phase consisting of interpenetrating chains such as tie chains, cilia, and loops (Peacock, 2000). The crystal content in polymers is highly dependent on the rate of cooling to allow enough time for the chains to achieve an ordered configuration (Bartczak and Galeski, 2010).

1.1.2 Mechanical Behavior of Thermoplastic Polymers

Semi-crystalline polymers exhibit an extremely nonlinear mechanical behavior that depends on structural factors such as crystallinity, molecular weight and cross-linking and loading conditions such as and loading path, temperature, and strain rate. The mechanical behavior of semi-crystalline polymers depends on the proportion of crystalline phase and the size, shape and

orientations of crystalline lamellas. Ayoub et al., (2010) presents the stress-strain experimental data for three different crystallinities of PE materials (Shown in Figure 1.3):

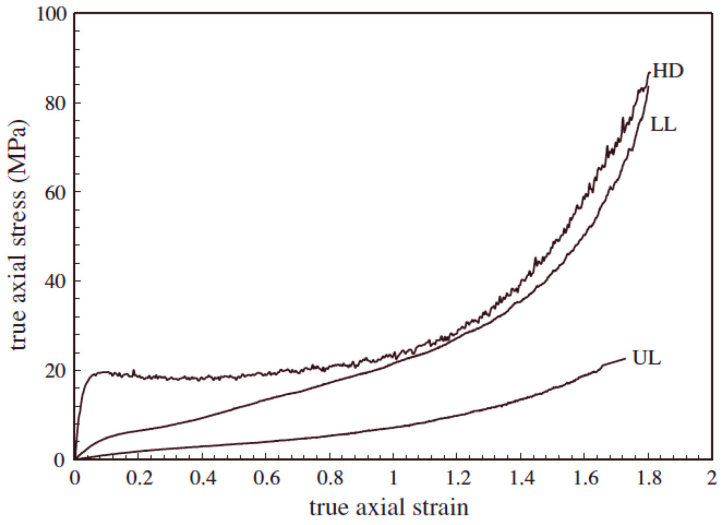

Figure 1.3: Experimental stress-strain data for (UL) Ultra low density polyethylene, (LL) low density polyethylene, (HD) High density polyethylene (Ayoub et al., 2010).

Although these materials are formed from the same monomer, their mechanical behavior is completely different due to a difference in the crystal content.

The yield stress, plastic flow, and strain hardening increase with increasing strain rate while inducing a loss of ductility (G. Ayoub et al., 2011b; El-Qoubaa and Othman, 2016; Rae et al., 2007; J. Richeton et al., 2006; Şerban et al., 2013). Furthermore, the yield stress, stiffness and strain hardening decrease with increasing temperature while inducing a gain of ductility (Brooks et al., 1998; Pampillo and Davis, 1972). The as cast semi-crystalline polymers exhibit isotropic mechanical response, and anisotropy can be induced by additional processing or preliminary deformation.

1.1.3 Constitutive Models Describing the Behavior of Polymers

In general, phenomenological, and physical based models are found in the literature capturing the mechanical behavior of semi-crystalline polymers. Phenomenological models are not directly derived from theory but relates empirical observations to a mathematical expression consistent with the fundamental theory. These models include (Balieu et al., 2013; Bardenhagen et al., 1997; Ben Hadj Hamouda et al., 2007; Cayzac et al., 2013; Colak, 2005; Drozdov, 2009; Drozdov and Gupta, 2003; Dusunceli and Colak, 2008, 2006; Ghorbel, 2008; Haward R. N., 1968; Khan and Zhang, 2001; Krempl and Khan, 2003; Regrain et al., 2009; Zaïri et al., 2008, 2005a, 2005b). Several phenomenological models used the Bodner theory (Bodner and Partom, 1975) as a starting point. Zhang and Moore, (1997) developed a simple mathematical nonlinear viscoelastic and a visco-plastic model based on Bodner's visco-plastic framework to predict the behavior of high-density polyethylene. Additionally, Pyrz and Zairi, (2007), Zaïri et al., (2005b) developed an elastic-viscoplastic model based on the Bodner theory to predict the highly nonlinear behavior and rate dependence of polycarbonate. In other works, Billon, (2012) developed a large strain visco-hyperelastic phenomenological model describing the mechanical behavior of polymers at different strain rate and temperatures. Cayzac et al., (2013) proposed a phenomenological model coupled with damage formulation based on porosity to model the deformation behavior of Polyamide 6. Krairi and Doghri, (2014) coupled viscoelasticity, viscoplasticity, and ductile damage to model different materials' experimental data (Polypropylene, high density polyethylene, …) from the literature. Nguyen et al., (2016) proposed a large strain hyperelastic phenomenological model to capture the mechanical behavior of amorphous glassy polymers. Jordan et al., (2020) proposed a mechanism based coupled machine learning approach to predict the strain rate and temperature mechanical response of polypropylene.

Moving on to physical based models, Haward R. N., (1968) first proposed a one-dimensional model represented by a spring in parallel with a series of Hookean spring and a dashpot, to account for both yielding and strain hardening. This pioneering work inspired the development of three-dimensional models describing the behavior of thermoplastics and cross-linked rubbers (H. Abdul-Hameed et al., 2014; H Abdul-Hameed et al., 2014; Amjadi and Fatemi, 2020; Anand and Gurtin, 2003; G. Ayoub et al., 2011b; Ayoub et al., 2014b; Bahrololoumi et al., 2020; Boyce et al., 1988; Felder et al., 2020 Govaert et al., 2000; Krairi et al., 2016; Krairi et al., 2019; Makki et al., 2017; Makradi et al., 2005; Shojaei and Li, 2013, Wu and Van Der Giessen, 1993). Parks and Ahzi, (1990) proposed a crystalline micromechanical rigid-viscoplastic model to describe the mechanical and texture evolution in polycrystalline materials. B.J. Lee et al., (1993a), B.J. Lee et al., (1993b) proposed a composite model to predict the mechanical behavior and texture evolution of semi-crystalline polymers in which the material is seen as a two-phase composite. The non-crystalline region used a network resistance based on the eight chain model (Arruda and Boyce, 1993) incorporated as a backstress tensor to account for the hardening in the material, while the crystalline phase used a crystallographic slip mechanism of crystal plasticity to model the driving slip mechanism of the crystal block segments (Asaro and Needleman, 1985). Two crystallographic slip mechanisms were considered; the chain slip and transverse slip. Van Dommelen et al., (2003) developed an elasto-viscoplastic model that uses a composite inclusion homogenization technique to divide the material into a collection of layered domains and relates them by an interaction law. Other newer models include the works of Makki et al.,(2017) proposing a viscohyperelastic-viscoelastic-viscoplastic model to capture the mechanical behavior under cyclic loading of three PE materials with different crystallinities. Guo and Zaïri, (2020) proposed

a micro-macro constitutive model for describing the chain network crystallization induced anisotropy.

1.2 Review of Separator Films

As mentioned previously, the separator is a crucial component in the battery. The separator acts as a barrier between the positive and negative electrodes and enables lithium-ions flow. Separator material type can be generally divided into three categories: (1) Inorganic composites, (2) non-woven fabric mats, and (3) microporous polymer membranes (Zhang, 2007). The separator does not contribute in any of the electrochemical reactions occurring in the battery, nevertheless, its mechanical properties and manufacturing process can alter the performance of the battery such as safety, the number of cycles determining the life of the battery, and power and energy density. Several requirements of the separator are needed in order to use it in batteries including: chemical stability against any chemical reaction occurring in the battery, suitable porosity for allowing ion flow between the electrodes, appropriate thickness in order to provide high energy and power densities, permeability, mechanical strength to endure tension and compression arising from the electrochemical and thermal processes in the different battery components, and minimal thermal shrinkage to keep allowing the transfer of ions through its pores.

1.2.1 Separator Properties

In this section, the general properties and requirements for lithium-ion battery separators are given. Thickness, porosity, chemical stability, dimensional stability, pore size and structure tortuosity, wettability, ionic conductivity, mechanical stability, high temperature stability, and shutdown temperature are discussed.

Thickness: Most consumer lithium-ion batteries use separators that are less than 25 μm in thickness (Costa et al., 2013). Additionally, separators should have uniform thickness to support even current distribution during charge and discharge. Thin separators take less space inside the battery cell and promotes the use of longer electrodes which leads to an increase in the overall energy density of the cell (Lee et al., 2014). However, thin separators are mechanically weak, and can rupture during cell assembly or during battery operation (Arora and Zhang, 2004). The thicker the separator, the greater the mechanical strength which reduces the probability of rupture and lead to improved battery safety. However, thick separators decrease the areal power density.

Porosity: Typically, the porosity of separators is around 40% to allow ionic transport in the electrolyte and minimize the internal resistance. Porosity is very important and is one of the separator acceptance criteria. Very high porosity will weaken the separator and decrease its mechanical integrity.

Chemical stability: The separator should be electrochemically stable during charge and discharge cycling. It should be inert under the reductive and oxidative conditions encountered during battery operation (Lee et al., 2014), should not degrade or interfere with the electrochemical reaction. Polyolefin separators exhibit excellent resistance to most chemicals, strong mechanical properties, which makes them ideal for lithium-ion battery separators.

Dimensional stability: The separator should lay flat and not skew or bow as it can affect the cell assembly. Moreover, its dimensional stability should be maintained when exposed to electrolyte. Dimensional instability of the separator can cause problems during the cell assembly, and shrinkage can cause the electrodes to touch at the edges resulting in a short circuit (Francis et al., 2020).

Pore size and structure: Separators should have a tight pore size distribution to prevent dendritic lithium penetration. A uniform morphology is also preferred to allow uniform current distribution within the cell and prevent performance losses.

Tortuosity: Tortuosity represents the average pore conductivity of the solid. An increase in tortuosity can impede dendritic growth but can lead to an increase in ionic resistance. Tortuosity is reflected in the Gurley number of the thickness and porosity are kept constant. The Gurley number quantifies permeability and is usually less than 0.0025 $s\,\mu m^{-1}$ for a separator. A low Gurley value implies high porosity and lower tortuosity (Arora and Zhang, 2004).

Wettability: The separator should wet out completely when exposed to electrolyte. Otherwise, incomplete wetting can cause uneven current distribution. If a part of the separator is not wet or does not contain electrolytes, it can lead to a dry spot which cannot fully utilize the electrodes active materials (Weber et al., 2015).

Ionic conductivity: The separator contains electrolytes which allow the exchange of lithium-ions between the electrodes. The conductivity between both electrodes is mainly related to the transport of the electrolytes. The ionic conductivity of the separator should typically be in the range of 10^{-3} to 10^{-1} S cm^{-1} (Lee et al., 2014).

Mechanical stability: The separator is subjected to mechanical stresses during the battery assembly, battery operation, and under abuse conditions. For this reason, the separator should be mechanical robust to withstand the mechanical stresses. A high tensile stress and a high puncture strength are both required to avoid rupture and penetration of electrode material which can cause short circuits in the battery (Huang, 2011). Additionally, the separator mechanical properties can significantly change when the separator is wet with electrolyte (Sheidaei et al., 2011).

High temperature stability: In addition to the mechanical stresses mentioned previously, the separator is subjected to temperature variations which can cause expansion or shrinkage. The thermal shrinkage of the separator in both the machine and transversal direction should be less than 5% after 60 minutes at 90 degrees Celsius.

Shutdown temperature: Separator can have "shutdown" functionality which stops the current flow when the temperature is very high about 130 degrees Celsius. The separator melts and closes the pores upon reaching the shutdown temperature which stops ionic transport between the electrodes. Moreover, the separator should be mechanically strong to prevent the contact between the electrodes after undergoing shutdown (Arora and Zhang, 2004).

1.2.2 Manufacturing and Morphology of Microporous Polymer Separators

Most of the polymer separators used in lithium-ion batteries are semi-crystalline polymers composed of Polyethylene, Polypropylene, or a mix of both such as PP/PE/PP. Two main processed are used for manufacturing microporous polymer membranes: (1) Dry process and (2) Wet process.

For dry process microporous polymer separators: the manufacturing process is divided into three stages (Johnson and Wilkes, 2002a, 2002b, 2001): (1) Extrusion, (2) annealing, and (3) stretching. Stage 1 is heating up the polymer resins above its melting temperature, then extruding the melt in between two cylindrical shaped tubes. This stage re-arranges the crystalline lamellae and align their direction perpendicular to the rolling direction or (Machine direction). In the second stage annealing of the extruded film is done at a temperature below its melting point. This stage helps in refining the crystalline structure and prepares the material for its microporous properties in the next stage. In the third stage, the film is stretched along the machine direction by a cold stretch creating a porous microstructure using a lower temperature and high strain rate. This

process is followed by a hot stretch to control the pore size using a high temperature with a low strain rate. Finally, the film undergoes heat treatment called relaxation to decrease internal stresses.

For wet process microporous polymer separators is divided into three stages as well (Foley and Celanese, 1993; Ihm et al., 2002): (1) Mixing of the polymer with additives then heating the solution, (2) extrusion of the solution through sheet die, and (3) extracting all additives with a solvent to create the microporous structure. In general, the same step used for dry process is used for the second stage here. Contradictory to dry process, wet process results in a non-oriented structure for both pores and mechanical behavior. Difference between the microstructure of both processes is shown in Figure 1.4.

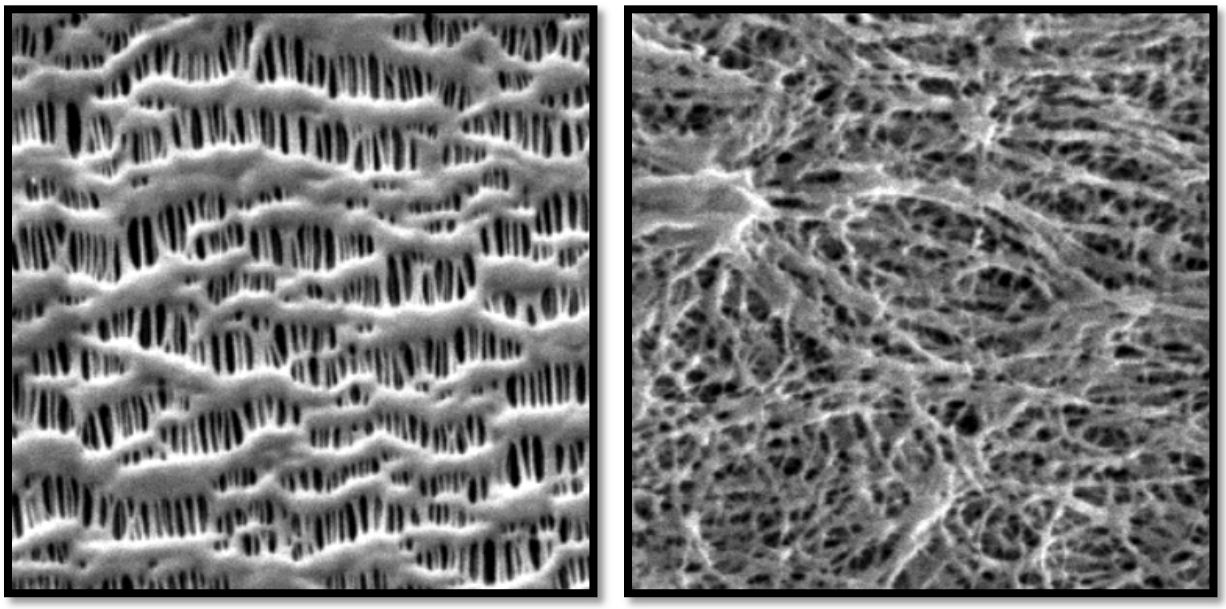

Figure 1.4: Scanning Electron Microscopy of (Left) dry process (Right) Wet process polyolefin films (Arora et al., 2004).

Comparing both processes from a microstructure point of view, dry process is specific to high energy density batteries due to the nature of its open pores, whereas wet process focuses more on the prolonging the battery life due to crosslink structure which helps prevents the development of dendritic Li during charge and discharge cycles.

1.2.3 Mechanical Behavior of Microporous Polymeric Films

Several studies investigated the mechanical behavior and assessed failure mechanisms of separators. Chen et al., (2014) performed tensile tests and in-situ tensile tests using an Atomic Force Microscope (AFM). It was reported that the deformation of dry-processed separators pulled in the machine direction (MD) is associated with crystalline lamellae separation accompanied with fibrils elongation in the amorphous region, followed by the sliding and breakage of the crystallite lamellae. It was also reported that, loading the separator along the transverse direction (TD) causes the breakage of lamellae by chain pull-out. Gor et al., (2014) analyzed the behavior of dry and wet polypropylene (PP) under compression loading and at different strain rates. The results showed that PP exhibited a strain-sensitive, viscoelastic and poroelastic behavior. Zhang et al., (2016a) studied the mechanical properties of two different battery separator films (Polyethylene (PE) and trilayer separators (PP/PE/PP)) and performed uniaxial tensile tests along the diagonal direction (DD), MD, and TD, compression tests and biaxial punch tests. Both dry processed films showed high tensile anisotropy, where loading along MD showed much higher strength than loading along DD and TD. SEM micrographs of tensile specimens revealed the activity of two deformation mechanisms: formation of new fibrils and opening of pores. Moreover, the dry-processed separators had a distinct failure mode in each direction; wrinkled non-smooth surface along MD and smooth failure along TD. SEM images of the through thickness compression tests showed the elongation of the bulk material in width and length causing the buckling of the fibrils. Two different failure modes were observed in the biaxial punch test; formation of cracks featuring large diagonal slit along MD, and a zig-zag surface along TD. Zhu et al., (2018) performed tensile tests on dry-processed microporous PP separator in three different directions. These separators were loaded to different strain levels then fully unloaded. SEM images showed that for small

displacements, both the crystalline lamellas and fibrils were stretched. For larger displacements, lamellae chains slipped past each other and disintegrated into fibrils. Kalnaus et al., (2018b) performed tensile tests along different directions and compression tests on trilayer-separator (PP/PE/PP) under different strain rate and temperatures. The authors reported a significant strain rate and temperature sensitivity and a strong anisotropy in the mechanical response of the separator. Kalnaus et al., (2018a) performed biaxial tension experiments on two grades of polymer separators and studied the critical strain at failure. The strain at failure is an input for a criterion that allows a good estimation for the internal short circuit. However, these tests were done only on as-received specimens. Zhang et al., (2017) studied the mechanical properties of separators, subjected to five different charge-discharge scenarios, under biaxial loading and reported that the strain to failure decreased with increased number of charge-discharge cycles.

1.2.4 Constitutive Models Describing the Behavior of Separators

Few models can be found in the literature on the mechanical behavior modeling of microporous separators. Zhang et al., (2016b) used an anisotropic foam model to approximate the separator behavior in various loading conditions. The model was able to predict the force displacement behavior of the separator subjected to tensile loading in different directions and in compression. However, for the biaxial punch test, the model predicted the force displacement behavior up to a certain punch displacement limit and for different punch diameters. Gor et al., (2014) developed a viscoelastic poroelastic quantitative model that predicts the elastic response of a commercial separator in compression at different strain rates. Xu et al., (2017) used microscopic images of the separator to identify a representative volume element (RVE), The RVE was used as finite element model to predict the stress-strain in a battery separator. Xiao et al., (2010) used a Multiphysics model to predict the stress behavior in battery components and more specifically of

separator materials. In such approach, electrochemical, thermal and mechanical equations are solved simultaneously using three sub-models to predict the stresses in the separator. It was found that the maximum stress in the separator was due to the indentation of electrode particles. Later, Shi et al., (2011) reported that the maximum stress in the separator was observed (numerically) at the contact with the electrode edge. It is worth noticing that all the aforementioned Multiphysics models assumed all the battery components to be linear elastic while ignoring the anisotropic properties of the separator.

1.3 Review Lithium-Ion Batteries

In efforts to reduce the carbon footprint, automotive industries are quickly shifting towards electrical vehicles as a clean source of energy. Lithium-ion batteries provides a clean source of energy storage systems for electrical vehicles. Lithium-ion batteries are the subject of intense research with the aim of improving their properties and characteristics. When compared to other types of battery technologies, lithium-ion batteries are the most suitable for electric vehicles (Dunn et al., 2011; Yang and Tarascon, 2012) due to their higher energy and power output per unit of battery mass (See Figure 1.5). Lithium-ion batteries are lighter and smaller than other battery technologies with the same energy storage capacity.

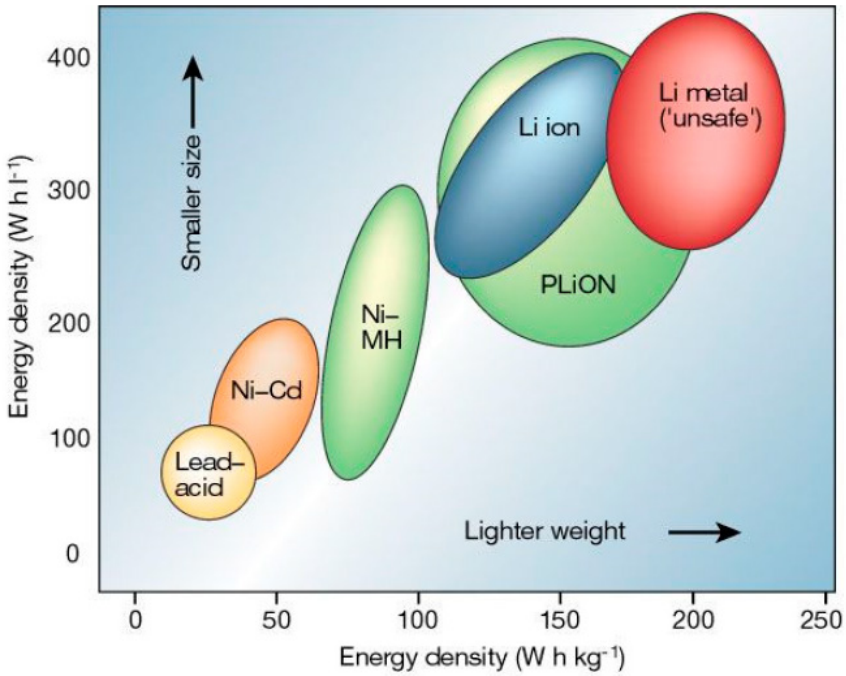

Figure 1.5: Different battery technologies in term of volumetric and gravimetric energy densities (Miao and Yokochi, 2019).

1.3.1 Types of Lithium-Ion Batteries

Lithium-ion batteries consist of an anode, a cathode, a separator, and current collectors submerged in liquid electrolytes. In general, lithium-ion batteries use a carbon negative electrode (graphite) or lithium titanate. Novel materials being developed include Li metal and Li(Si) alloys. The electrolyte choice is based on the choice of electrode materials. Typically, electrolytes are composed of a mixture of lithium salts ($LiPF_6$) and organic solvent (diethyl carbonate) to allow for ion transfer. There are many choices for the positive and negative electrodes materials, the electrolyte, and the separator.

For the positive electrodes, they are intercalation compounds that can diffuse lithium-ion in or out. Some well-known examples include Lithium Cobalt Oxide ($LiCoO_2$), Lithium Nickel Oxide ($LiNiO_2$), Lithium Manganese Oxide ($LiMn_2O_4$), Lithium Iron Phosphate ($LiFePO_4$),

Lithium Nickel Manganese Cobalt Oxide ($Li(Ni_xMn_yCo_{1-x-y})O_2$), and Lithium Nickel Cobalt Aluminum Oxide ($Li(Ni_xCo_yAl_{1-x-y})O_2$). For the negative electrodes, two main types are being used which include carbon-based electrodes, and lithium titanate ($Li_4Ti_5O_{12}$). Other types in development include lithium-metal alloys specifically lithium-silicon and conversion electrodes (Miao and Yokochi, 2019).

1.3.2 Comparison of Different Types of Lithium-Ion Batteries Used in Electrical Vehicles

The main factors considered in lithium-ion batteries used in electrical vehicles are specific power, specific energy, performance, safety, life span, and cost. Specific power of a battery represents the ability to provide high current on demand and demonstrates potential vehicle acceleration. Specific energy represents how much energy a battery contains per unit weight which reflects in the driving range. Safety is a very important feature in lithium-ion batteries as it can affect public opinion. Performance represents the ability of a battery to perform in harsh temperature conditions. Life span represents the longevity of the battery. Finally, cost represents the feasibility of using the technology. Figure 1.6 shows a comparison between different types of lithium-ion batteries. NMC batteries which are used in this research offer high specific power, safety, performance, and life span and excellent specific energy. Other types of batteries such as lithium-ion phosphate (LFP) have a better life span, however lower specific energy.

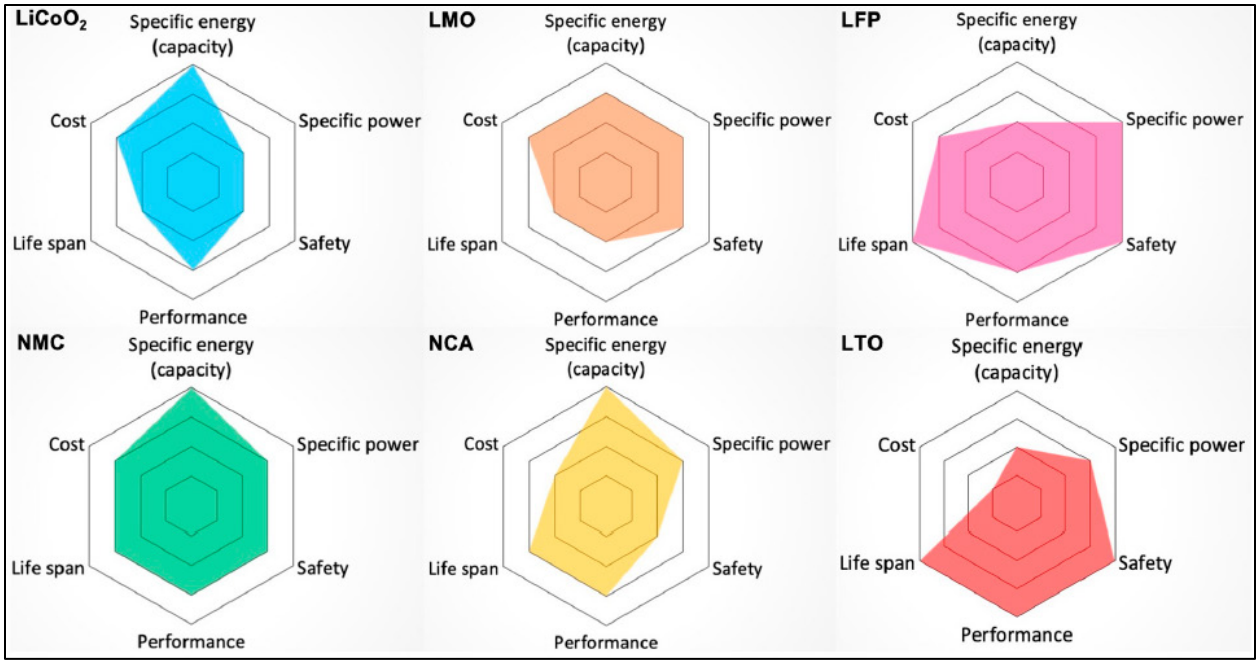

Figure 1.6: Comparison between different types of lithium-ion batteries used in Electrical Vehicles (Miao and Yokochi, 2019).

1.4 Research Objectives

The literature review pointed out the limited knowledge on the degradation of battery separators induced by normal charge-discharge cycles. Additionally, there is no research describing the mechanisms of degradation in the separator under fast charge and discharge cycles. Indeed, there is a lack of knowledge when it comes to the separator degradation under normal and fast charging. While there is an abundance of models developed to predict the mechanical behavior of polymers, very few models were developed to predict the mechanical behavior of microporous films and up to the author's knowledge, no models were developed to predict the degradation behavior of separator under different number of charge and discharge cycles. An accurate characterization and modelling of the separator's mechanical behavior and induced degradation under charge and discharge cycles is essential for optimal design and operation of commercial lithium-ion batteries.

The specific objectives of this dissertation are:

(1) Understand the mechanisms behind the chemical and mechanical degradation of separators under charging and discharging cycles, specifically fast charging conditions.

(2) Identify the effect of cell operations including the number of cycles on the separator degradation.

(3) Provide designers with predictive tools that allow them to improve the battery life efficiency and safety.

To attain those objectives the following work will focus on two main tasks:

I. Study the changes in mechanical behavior, microstructural features, and chemical characterization of separators at different numbers of charge discharge cycles.

II. Develop a separator aging model based on:

   i. The aging mechanisms behind strength degradation of a lithium-ion battery separator.

   ii. The effect of fast charging on the separator aging.

   iii. Multiphysics modeling of the battery cell to understand stress and temperature conditions during charge and discharge cycles.

1.5 Chapter Distribution

This dissertation is presented in five chapters as described below:

Chapter 1 is an introductory chapter containing a general review about polymers; Morphology, mechanical behavior, and constitutive models describing their mechanical behavior. Moreover, the problem statement and research objectives are presented.

Chapter 2 investigates the mechanical behavior of the pristine separator under uniaxial tension and biaxial loading tests. A finite element model using continuum damage mechanics was

developed to predict the mechanical behavior of the separator. Additionally, the capabilities of the model to predict the mechanical behavior of other types of porous separators was assessed using experimental data from the literature.

Chapter 3 examines the physico-chemical degradation mechanisms occurring in the cycled separators under fast-charging conditions. The experimental plan for the lithium-ion battery charging is first presented. Moreover, the physical and chemical microstructural changes in the cycled separators were investigated using a series of tests such as scanning electron micrographs, X-ray photoelectron spectroscopy, Fourier Transform Infrared Spectroscopy, and mechanical tests such as uniaxial tension and biaxial loading. The degradation mechanisms occurring in the separator under fast charging conditions are presented and discussed.

Chapter 4 discusses the development of a Multiphysics model created using COMSOL and MATLAB to predict the stresses inside the battery and specifically the separator under fast charging conditions. The model is described in details and the equations used are provided. The model parameters are identified, and the results are provided and discussed.

Chapter 5 summarizes the findings from the previous chapters and discusses the intellectual merit and broader impact of this research.

Chapter 2 Modeling the Anisotropic Behavior of Highly Orthotropic Polymer Separators in Lithium-Ion Batteries

Separators in commercial lithium-ion batteries are microporous polymeric films characterized by highly anisotropic mechanical behavior. An accurate characterization of their mechanical and fracture behavior is essential for optimal design, performance, and safety of lithium-ion batteries. In this chapter, the mechanical and fracture behavior of battery separators subjected to uniaxial tension and punch tests are characterized and discussed. An anisotropic continuum damage coupled elastic-hyperelastic-viscoplastic model is developed in the framework of the large deformation theory to capture the mechanical and fracture behavior of battery separators. A robust implicit integration scheme is developed then the model is implemented as a user-defined material subroutine (UMAT) in commercial finite-element software in order to solve boundary-value problems. The capability of the proposed model to predict the anisotropic mechanical behavior up to fracture for two different types of battery separators highlights the versatility of the proposed modeling approach. The model results showed a good agreement with the experimental data. Moreover, the model was able to predict the failure of the separators under different loading conditions.

2.1 Introduction

Small portable electronic devices such as smartphones and laptops rely widely on lithium-ion (Li-ion) batteries as power sources. Furthermore, Li-ion batteries are the dominantly used

technology in electric vehicles (Iclodean et al., 2017), since, compared to other battery counterparts, they present numerous advantages such as high energy density, high specific energy, and ability to undergo large numbers of charge-discharge cycles (Alaoui, 2013; Gerssen-Gondelach and Faaij, 2012; Lu et al., 2013; Lukic et al., 2008). Lithium-ion batteries consist of an anode, cathode, separator, current collectors, and electrolyte wrapped in a shell casing or plastic cover. In this study, we focused on understanding the mechanical behavior up to fracture of different types of separators and adequately developed a modeling framework with a robust numerical implementation for use in commercial finite element software.

Separators in commercial lithium-ion batteries are microporous films consisting of a polymeric membrane such as polyethylene or polypropylene, inorganic composite membranes, and non-woven fabric mats (Zhang, 2007). Polyolefin membranes are the most widely used due to their many advantages such as low cost, high safety, and high performance (Linden and Reddy, 2002; Zhang, 2007). Polyolefin membranes are semi-crystalline polymers consisting of an interconnecting amorphous and crystalline microstructure. The separator is sandwiched between the anode and the cathode, typically in a spiral-wound or prismatic design, to prevent physical contact while its porous structure allows the exchange of ions (Arora and Zhang, 2004). Separators should be chemically inactive and mechanically robust to withstand the large tensile deformation applied during battery assembly and the charge and discharge cycles (Huang, 2011). Indeed, the lithium insertion electrochemical process causes large volumetric expansion of the electrode materials (Timmons and Dahn, 2007), which then causes large deformation of the separator.

Semi-crystalline polymers are available in a wide range of mechanical properties induced by crystallinity ratio ranging between 5% and 90%. Semi-crystalline polymers exhibit an extremely nonlinear mechanical behavior that depends on structural factors such as crystallinity,

molecular weight, and cross-linking and on loading conditions such as loading path, temperature, and strain rate. The microstructure of semi-crystalline polymers combines two solid phases: the crystalline phase, consisting of an ordered macromolecular structure, and the amorphous phase, consisting of disordered interpenetrating chains. An increasing strain rate increases the yield stress, plastic flow, and strain hardening while inducing a loss of ductility (G. Ayoub et al., 2011b; El-Qoubaa and Othman, 2016; Rae et al., 2007; J. Richeton et al., 2006; Şerban et al., 2013). Furthermore, increasing temperature decreases the yield stress, stiffness, and strain hardening while inducing a gain of ductility (Brooks et al., 1998; Pampillo and Davis, 1972). The as-cast semi-crystalline polymers exhibit isotropic mechanical response, and anisotropy can be induced by additional processing or preliminary deformation.

Several studies investigated experimentally the mechanical behavior and assessed the failure mechanisms of battery separators. Chen et al. (2014) performed tensile tests and in-situ tensile tests using an atomic force microscope (AFM). It was reported that the deformation of dry-processed separators pulled in the machine direction (MD) is associated with crystalline lamellae separation accompanied by fibrils elongation in the amorphous region, followed by the sliding and breakage of the crystallites lamellae. It was also reported that, loading the separator along the transverse direction (TD) causes the breakage of lamellae by chain pull-out. Gor et al. (2014) analyzed the behavior of dry and wet polypropylene (PP) separators under compression loading and at different strain rates. The results showed that PP separators exhibited a strain-sensitive viscoelastic and poroelastic behavior. Zhang et al. (2016a) studied the mechanical properties of two different battery separator films, polyethylene (PE) and trilayer (PP/PE/PP) separators, and performed uniaxial tensile tests along the diagonal direction (DD), MD, and TD; compression tests; and punch tests. Both dry-processed films showed high tensile anisotropy, where loading

along MD showed higher strength than loading along DD and TD. SEM micrographs of tensile specimens revealed the activity of two deformation mechanisms: formation of new fibrils and opening of pores. Moreover, the dry-processed separators had a distinct failure mode in each direction: a wrinkled non-smooth surface along MD and smooth failure along TD. SEM images of the through-thickness compression tests showed the elongation of the bulk material in width and length causing the buckling of the fibrils. Two different failure modes were observed in the punch test: formation of cracks featuring a large diagonal slit along MD and a zig-zag surface along TD. Zhu et al. (2018) performed tensile tests on dry-processed microporous PP separators in three different directions. These separators were loaded to different strain levels and then fully unloaded. SEM images showed that for small displacements, both the crystalline lamellae and fibrils were stretched. For larger displacements, lamellae slipped past each other and disintegrated into fibrils. Kalnaus et al. (2018b) performed tensile tests along different directions and compression tests on a trilayer (PP/PE/PP) separator under different strain rates and temperatures. The authors reported a significant strain rate and temperature sensitivity and a strong anisotropy in the mechanical response of the separator.

Few models were specifically developed for predicting the mechanical and fracture behavior of battery separators. However the literature is rich with models developed for capturing the behavior of semi-crystalline polymers that we categorize as phenomenological or physical based models. Haward R. N. (1968) first proposed a one-dimensional model represented by a spring in parallel with a series of Hookean springs and a dashpot to account for both yielding and strain hardening. This pioneering work inspired the development of three-dimensional models describing the behavior of thermoplastics and cross-linked rubbers (H. Abdul-Hameed et al., 2014; Amjadi and Fatemi, 2020; Anand and Gurtin, 2003; G. Ayoub et al., 2011b; Ayoub et al., 2014b;

Bahrololoumi et al., 2020; Boyce et al., 1988; Felder et al., 2020 Govaert et al., 2000; Krairi et al., 2016; Krairi et al., 2019; Makki et al., 2017; Makradi et al., 2005; Shojaei and Li, 2013, Wu and Van Der Giessen, 1993; Parks and Ahzi 1990; Kweon and Benzerga, 2013; Felder et al., 2020; Shojaei and Wedgewood, 2017; Shojaei and Volgers, 2017). Modeling the mechanical behavior of microporous separators was the interest of a few investigations found in the literature. Xiao et al. (2010) and Shi et al. (2011) used a Multiphysics model assuming linear elasticity to predict the stress behavior in battery components and more specifically of separator materials. Later, Gor et al. (2014) developed a viscoelastic poroelastic quantitative model that predicts the elastic response of a commercial separator in compression at different strain rates. Zhang et al. (2016b) used an anisotropic foam model to approximate the separator behavior in various loading conditions. However, the fracture behavior of the microporous separators was not studied. Xu et al. (2017) used an image-based microstructure representative volume element (RVE) finite element modeling method to predict the evolution of the mechanical and microstructure properties of a battery separator. The imaged-based finite element modeling was later used in Pan et al., (2020) for theoretical analysis of the microstructural instabilities, and the transparency phenomenon of the separator material under large deformation. Lee et al. (2020) modified the Gurson-Tvergaard-Needleman-Lemaitre and Khan-Huang-Liang models to predict the mechanical behavior of polymeric foams under compression at different strain rates and temperatures, yet the fracture was not studied. Understanding and modeling the mechanical behavior up to fracture of battery separators is very important to guide engineers in designing lithium-ion batteries with optimal structural properties. Modeling the fracture of polymeric foams such as battery separators was not addressed in the literature since the existing models didn't account for damage and damage accumulation mechanisms in their formulations. To address this gap, this work aims to propose a

modeling framework of the mechanical behavior up to fracture of different types of battery separators and develop a robust numerical implementation for use in commercial finite element software.

For that purpose, in this work we first characterized and discussed the mechanical behavior up to fracture of battery separators. Next, an anisotropic continuum damage coupled elastic-hyperplastic-viscoplastic model was developed to capture the mechanical and fracture behavior of battery separators. The model implementation as a user-defined material subroutine (UMAT) in commercial three-dimensional finite-element software was achieved by developing a robust implicit integration scheme. In this chapter, the capability of the proposed model to predict the anisotropic mechanical behavior up to fracture for two different types of battery separators is assessed: a single-layer wet-processed PE (our experiments) and a trilayer dry-processed PE-PP-PE (from the literature). After the model parameters were identified using tensile experiments along different loading directions, the model's predictive capability was assessed with punch experiments.

The chapter is organized as follows: In section 2.2, mechanical characterization of the two types of separators based on both tensile and punch tests are discussed. In section 2.3, the mathematical framework of the anisotropic continuum damage coupled elastic-hyperplastic-viscoplastic model is described. A parameter sensitivity study is conducted and discussed in section 2.4. Additionally, the model parameters identification procedure is presented, and the model capability to predict the structural mechanical and fracture response is assessed. Finally, concluding remarks are provided.

2.2 Mechanical Characterization

In this section, the microstructure and mechanical characterization of different battery separators are presented to investigate the main features of the anisotropic nonlinear elastic-hyperelastic- viscoplastic responses up to fracture.

2.2.1 Materials

A wet-processed polyethylene (PE) separator supplied to us by our project sponsor was used in this study and had a crystallinity range between 60 and 80 %. The films were fabricated through a co-extrusion blowing process. An anisotropic microstructure results from this process, as can be observed from the SEM micrographs of the separator surface (Figure 2.1.a). Figure 2.1.a shows a porous structure with uniformly distributed slightly elliptical pores (with the main axis being along MD). The thickness of the separator film is 12 μm. The separator presents a porosity of 43%. Table 2.1 provides additional separator properties provided by the manufacturer. In this study we assume that skin effects are negligible for thin films.

Table 2.1: Data provided by manufacturer.

Air Permeability (sec/100cc)	170
Film Thickness (um)	12
Basis Weight (g/m^2)	6.4
Puncture Resistance (gf)	570
Porosity (%)	43
Heat Shrinkage MD (% @105°C, 8hr)	4.0
Heat Shrinkage TD (% @105°C, 8hr)	4.5
Tensile Strength MD (kgf/cm^2)	2400 (235 MPa)
Tensile Strength TD (kgf/cm^2)	2300 (225 MPa)

In addition to the aforementioned wet-processed single layer polyethylene (PE) separator, we studied a dry-processed trilayer (PP-PE-PP) separators investigated by Zhang et al. (2017). The

purpose of using published experimental data is to assess the capability of the developed model (described in section 2.3) to predict the mechanical behavior of different types of separators.

2.2.2 Methods and Characterization Results

Tensile specimens were razor cut from as-received separator roll with their major axis being aligned with three different directions, namely, MD for machine direction, DD for diagonal direction, and TD for transverse direction (see Figure 2.1.b). The strip-shaped uniaxial tensile specimens were prepared according to ASTM D882. The strips' geometry is rectangular, with a length of 100 mm and a width of 25 mm. For tensile tests, the gage length was set to 50 mm.

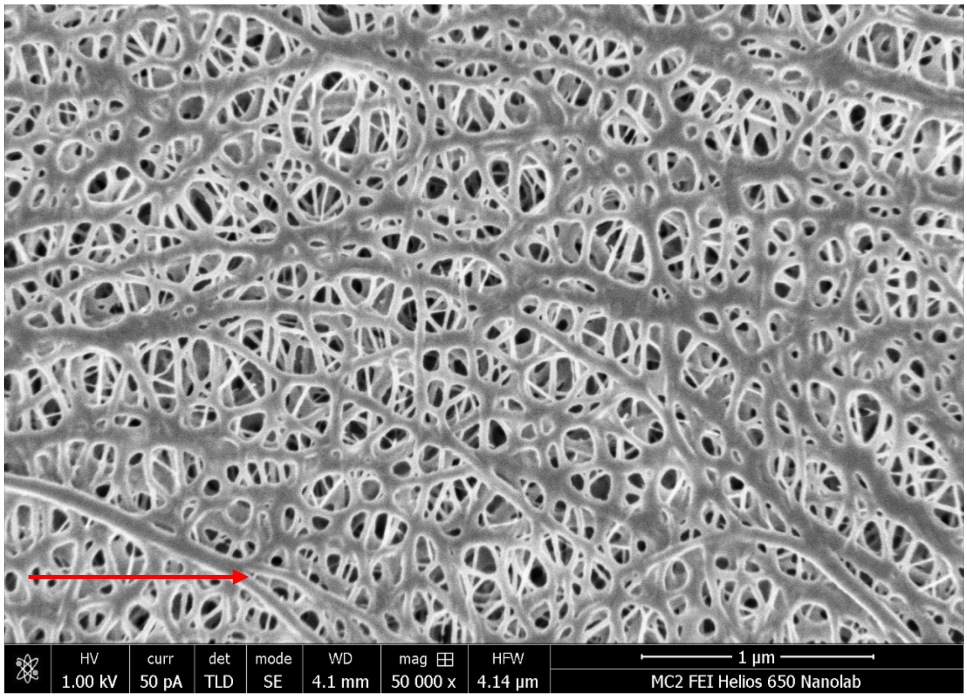

(a)

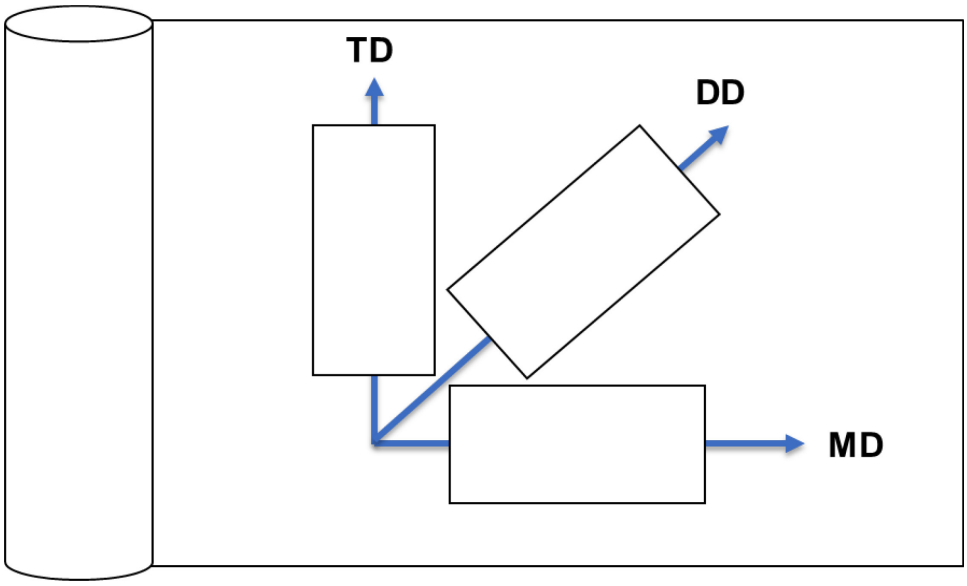

(b)

Figure 2.1: (a) Scanning electron microscope (SEM) micrographs of the PE separator surface. The MD is indicated by the red arrow. (b) Direction of samples from the separator roll.

A TestResource Model TR 100Q225 universal test machine equipped with a 220 N (~50 lb.) load cell was used to perform the tensile tests with a constant crosshead speed of 500 mm/min (selected to mimic the loading condition of battery separator during fast charging) at room temperature. Each tensile test condition was repeated five times and the average was computed. Figure 2.2 presents the engineering stress-strain behavior of the PE films along the three material directions. The engineering stress σ is defined as the ratio between the load F and the original cross-sectional area A of the sample. The engineering strain ε is defined as the ratio between the elongation Δl and the original gauge length l_0.

The overall behavior of the porous PE film shows a faint linear response associated with a steady rollover to the plastic region followed by a slower increase of the stress. The porous PE film shows an anisotropic behavior, with clear differences in the tensile response along the different material directions. We notice that the highest stresses are measured along MD while the lowest stresses are along DD. Although the largest difference in stress is around 46 MPa, the

studied PE separator does not exhibit large anisotropic behavior compared to the ones reported in the literature such as for the trilayer dry-processed PE-PP-PE studied by Zhang et al., (2017). Indeed, it was reported that the trilayer separator presented a highly anisotropic microstructure characterized by elongated pores aligned along MD, which explains the large difference in the mechanical behavior measured along MD and TD.

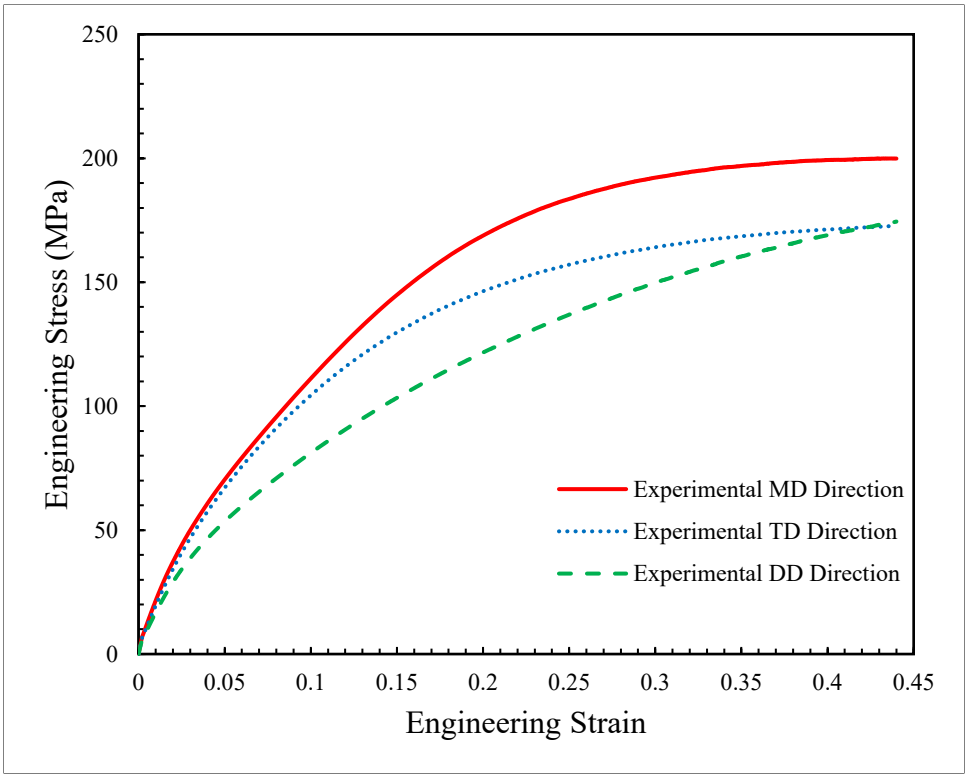

Figure 2.2: Experimental tensile tests in three directions.

The assessment of the fracture behavior of films can be challenging when using uniaxial specimens. Indeed, the edge quality of films is difficult to control and often induces stochasticity in the fracture strain; therefore, punch tests can be used to eliminate the edge quality effect and hence reduce the stochasticity. Moreover, punch tests represent the loading condition separators may undergo during battery charge-discharge scenarios (Zhang et al., 2016a). Separators are rolled around the relatively sharp edges of the anode and the cathode which may subject the separator to

a biaxial loading condition during battery charge-discharge cycles (Chen et al., 2014a). Punch tests were carried out using the same universal test machine as mentioned previously. The punch setup is shown in Figure 2.3.a. The setup consists of a die, a clamping plate, and a punch. The punch head is used to apply biaxial loading to the separator. The recommended punch diameter according to ASTM F1306-90 is 3.2 mm. In this study, two 3D-printed polymer hemispherical punch heads of 3.2 and 12.7 mm diameter were used. The punch diameter of 12.7 mm was used in this study to compare the behavior of the studied PE separator and the trilayer (PP-PE-PP) separators studied by Zhang et al. (2017). Both the die and the clamping plate have an internal radius of 16 mm. Square specimens were cut and then tightly gripped between the die and clamping plate. Two rubber rings placed in grooves machined into the die base and the clamping plate were used to tightly grip the sample and avoid slipping. The die central axis is carefully aligned with the universal test machine axis. The punch head was gripped between two steel jaws. Each test was repeated twice, and the average load displacement curves are shown in Figure 2.3.b. The 3.2 mm punch head load-displacement results present a steady almost linear increase up to failure. The 12.7 mm punch head results, show as expected, higher forces, the load-displacement curves present initially a steady linear increase up to a 3mm displacement followed by a slow counterclockwise rollover to a higher-slop linear increase up to failure. The separator images after failure are shown in Figure 2.3.b. The samples deformed using the 3.2 and 12.7 mm diameter punch heads showed a slit along the machine direction. When the separator is punched, a stress localization develops along MD below the punch head, which will ultimately lead to fracture in the form of a slit along MD. Similar fracture behavior was reported by Zhang et al. (2016b) on single-layer PE separators.

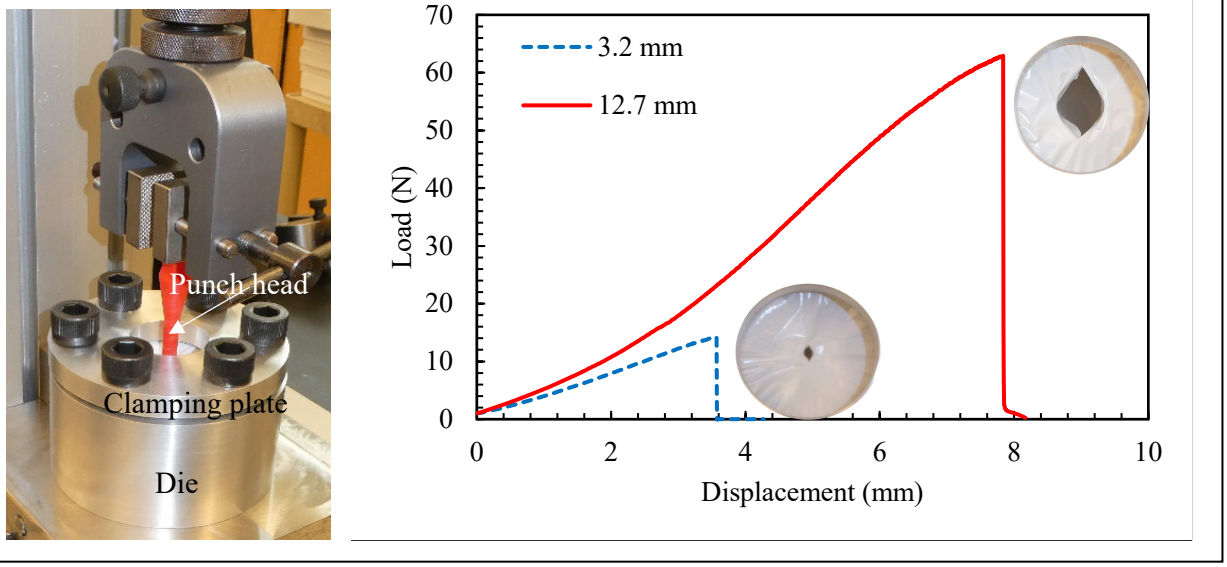

(a) (b)

Figure 2.3: (a) punch test setup, (b) punch test results for PE separator using two different punch diameters. Punch test separators after failure: (left) 3.2 mm punch head diameter, (right) 12.7 mm punch head diameter.

In addition to the aforementioned experimental results, the experimental data on dry-processed trilayer (PP-PE-PP) separators investigated by Zhang et al. (2017) were used in this chapter. Figure 2.4 presents the extracted uniaxial tension and punch tests experimental data. Zhang et al. (2017) used strip-shaped uniaxial tensile test specimens with a uniform width of 10 mm and gage length of 35 mm. The uniaxial tensile test was conducted along different material directions, and the results showed a high anisotropy, with a significantly higher strength along MD compared to the stresses along TD and DD. For the punch tests, specimens were circular and tightly gripped between the die and the clamping plate. In our investigation, we used the punch tests results of only the 12.7 and 3.2 mm punch heads. More details can be found in Zhang et al. (2017).

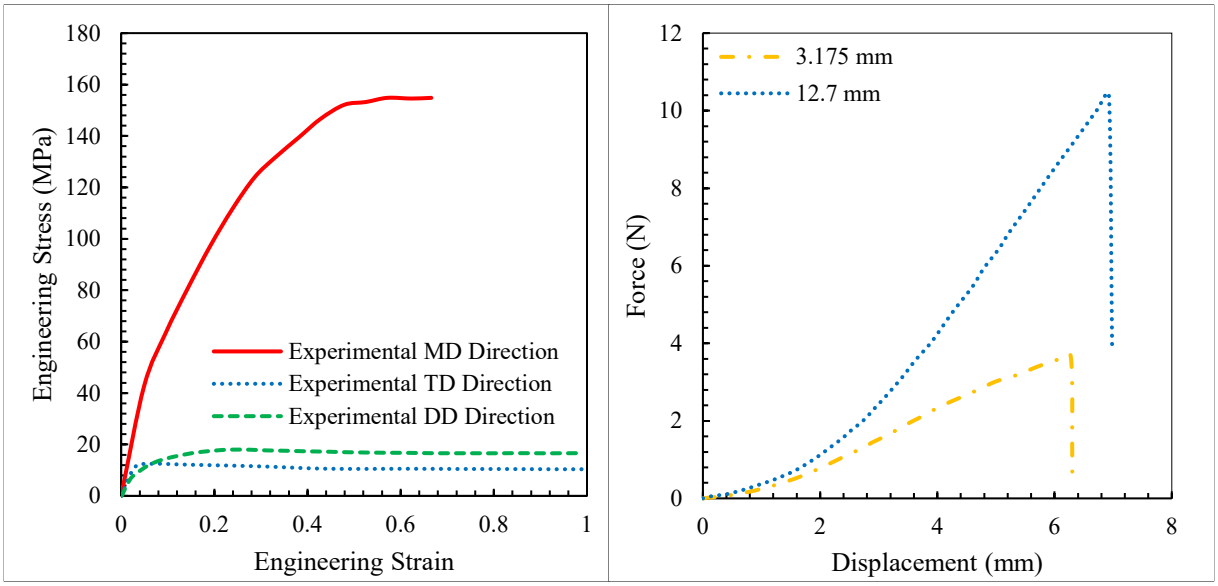

Figure 2.4: Zhang et al. (2017) tri-layer (PP/PE/PP) separator experimental results: (a) engineering stress-strain along different material directions; (b) punch test results for different punch diameters.

2.3 Modeling

In this work, an anisotropic continuum damage coupled elastic-hyperelastic-viscoplastic model was developed in the framework of the large deformation theory to capture the anisotropic mechanical behavior of porous separator structures. Continuum damage mechanics models are based on a damage accumulation principle derived from a thermodynamic dissipation potential (Lemaitre, 1992). In these models, plasticity and damage are coupled to predict the mechanical behavior of the material. The concept of damage was first introduced by Kachanov (1958) and Rabotnov, (1969) who related damage to microstructural alteration associated with cracks, cavities, and voids that result in mechanical properties degradation such as decreases in the stiffness, strength, and toughness. Chaboche (1997) and Lemaitre (1994, 1985) developed continuum damage mechanics models by assuming isotropic elastoplastic behavior of metals. However, the damage initiation and growth is essentially anisotropic, and based on this assumption

Sidoroff introduced an anisotropic damage tensor (Sidoroff, 1981). Theoretical formulations of coupled anisotropic plasticity and continuum damage mechanics were presented in several investigations, with the damage being considered as a second-order tensor (Chow et al., 2001; Chow and Wang, 1988, 1987; Chow and Yang, 2002; Cordebois and Sidoroff, 1982a) or a fourth-order tensor (Armero and Oller, 2000; Chaboche, 1981; Hammi et al., 2004; Krajcinovic, 1985; Kassar et al., 2019). While continuum damage mechanics was essentially used for metals, few investigations used the approach to predict the behavior of polymers (Krairi et al., 2019, 2016; Krairi and Doghri, 2014; Ayoub et al., 2014a, 2011a, 2010; Voyiadjis et al., 2012; Cayzac et al., 2013; Holopainen et al., 2017).

In this chapter, we used the following notation conventions: second-order tensors are represented by boldface symbols (e.g. **A**), while fourth-order tensors are represented by double-struck symbols (e.g. $\mathbb{A}$). A dot on top of a letter refers to the time derivative (e.g. $\dot{A}$). $\boldsymbol{A}^{-1}$ represents the inverse of a tensor while $\boldsymbol{A}^{T}$ represents the transpose of a tensor.

2.3.1 Deformation Kinematics

In this section a brief description of the deformation kinematics defined under finite strain, is provided. The deformation gradient $\boldsymbol{F} = \nabla \boldsymbol{x}(\boldsymbol{X}, t)$ relates the undeformed reference configuration $\boldsymbol{X}$ to the deformed current configuration $\boldsymbol{x}$. The multiplicative decomposition of the deformation gradient was suggested by Lee (1969) as $\boldsymbol{F} = \boldsymbol{F}^{e}\boldsymbol{F}^{p}$, with $\boldsymbol{F}^{e}$ being the elastic deformation gradient and $\boldsymbol{F}^{p}$ the plastic deformation gradient. The velocity gradient $\boldsymbol{L} = \dot{\boldsymbol{F}}\boldsymbol{F}^{-1}$ can also be expressed as:

$$\boldsymbol{L} = \boldsymbol{D} + \boldsymbol{W} \tag{2.1}$$

Where $\boldsymbol{W}$ is the spin component (skew-symmetric part) and $\boldsymbol{D}$ is the total rate of deformation (symmetric part). Additionally, the velocity gradient can be written as $\boldsymbol{L} = \boldsymbol{L}^{e} + \boldsymbol{L}^{p}$ with $\boldsymbol{L}^{e}$ and

$\boldsymbol{L}^p$ being the elastic and plastic velocity gradients respectively. The elastic and plastic velocity gradients can be decomposed additively in terms of their respective elastic symmetric and skew-symmetric:

$$\boldsymbol{L}^e = \boldsymbol{D}^e + \boldsymbol{W}^e \text{ and } \boldsymbol{L}^p = \boldsymbol{D}^p + \boldsymbol{W}^p \tag{2.2}$$

Khan and Huang (1995) suggested decomposing of the total rate of deformation $\boldsymbol{D} = \boldsymbol{D}^e + \boldsymbol{D}^p$ into elastic and plastic rates for finite deformation.

2.3.2 Model Formulation

In this section a unique constitutive model is proposed that for the first time combines between the anisotropic continuum damage theory and the constitutive model of Arruda and Boyce, (1993) that is carefully reformulated using the back-stress approach of Wu and van der Giessen, (1996). Furthermore, the mathematical framework of the constitutive model presents a unique formulation in which the hill anisotropic tensor and the damage tensor are written as fourth-order to present a practical approach for combining the different theories. In this study, to optimize the number of used parameters, the different deformation mechanisms between the crystalline phase and amorphous phase were not considered separately but were modeled as one set of equations combining the contribution of both phases. For more details regarding the modeling of semi crystalline polymers, the reader can refer to the author's previous investigations that account in the proposed models for the different phases contribution (H. Abdul-Hameed et al., 2014; Ayoub et al., 2020, 2010b, 2010c; G. Ayoub et al., 2011b; Makki et al., 2017a).

2.3.2.1 Continuum Damage Elasticity

The ductile fracture in porous polyethylene films is associated with the elongation of amorphous chains along the loading direction and breakage of weak bonds, followed by the formation of crystalline blocks and their alignment along the loading direction. Finally, the

crystalline blocks disintegrate into a fibrillary microstructure before complete fracture (Galeski et al., 2010). A damage variable can be defined to quantify the material microstructure deterioration associated with the breakage of chains and pores growth and coalescence. The continuum damage model scheme used in this work is based on the energy equivalence hypothesis (Cordebois and Sidoroff, 1982b, 1982a). The formulations of the anisotropic continuum damage model under finite strain follow a thermodynamics framework of positive dissipation. In this section, we propose a time-dependent framework that directly incorporates damage in both the elasticity and plasticity formulations. In the hypotheses of isotropic damage, the damage variable is defined as a scalar variable $\varphi = (A - \tilde{A})/A$, with A being the total cross-sectional area of a representative elementary volume (REV) with homogeneously distributed voids, and $\tilde{A}$ is the effective area that represents the total cross-sectional area of the REV excluding micro-voids. The normalized force applied on the effective area is defined as the effective stress $\tilde{\sigma} = F/\tilde{A}$. In the assumption of anisotropic damage, the damage variable is defined as a second order symmetric tensor $\boldsymbol{\varphi}^T = [\varphi_{11}\ \varphi_{22}\ \varphi_{33}\ \varphi_{23}\ \varphi_{13}\ \varphi_{12}]$, expressed in the coordinate system of the material. The effective stress $\tilde{\boldsymbol{\sigma}}$ defined as the stress in the undamaged fictitious configuration is related to stress $\boldsymbol{\sigma}$ in the damaged material configuration through the fourth-order damage effect linear tensor $\mathbb{M}$ as follows $\tilde{\boldsymbol{\sigma}} = \mathbb{M}:\boldsymbol{\sigma}$. The fourth-order damage effect tensor $\mathbb{M}$ is an operator that maps the damaged material configuration to an undamaged fictitious configuration. In previous investigations, $\mathbb{M}$ was mainly expressed in the principal direction of the damage, which is not always aligned with the principal direction of deformation; hence, it is difficult to implement in finite element code. To overcome this challenge, $\mathbb{M}$ is defined in the global coordinate system. In this study we used the explicit formulation proposed by Voyiadjis and Kattan, (2006, 1999, 1992):

$$\mathbb{M} = \frac{1}{2\nabla}\begin{pmatrix} 2\psi_{22}\psi_{33} - 2\varphi_{23}^2 & 0 & 0 \\ 0 & 2\psi_{11}\psi_{33} - 2\varphi_{13}^2 & 0 \\ 0 & 0 & 2\psi_{11}\psi_{22} - 2\varphi_{12}^2 \\ 0 & \varphi_{12}\varphi_{13} + \varphi_{23}\psi_{11} & \varphi_{12}\varphi_{13} + \varphi_{23}\psi_{11} \\ \varphi_{12}\varphi_{23} + \varphi_{13}\psi_{22} & 0 & \varphi_{12}\varphi_{23} + \varphi_{13}\psi_{22} \\ \varphi_{13}\varphi_{23} + \varphi_{12}\psi_{33} & \varphi_{13}\varphi_{23} + \varphi_{12}\psi_{33} & 0 \end{pmatrix}$$

$$\begin{pmatrix} 0 & 2\varphi_{12}\varphi_{23} + 2\varphi_{13}\psi_{22} & 2\varphi_{13}\varphi_{23} + 2\varphi_{12}\psi_{33} \\ 2\varphi_{12}\varphi_{13} + 2\varphi_{23}\psi_{11} & 0 & 2\varphi_{13}\varphi_{23} + 2\varphi_{12}\psi_{33} \\ 2\varphi_{12}\varphi_{13} + 2\varphi_{23}\psi_{11} & 2\varphi_{12}\varphi_{23} + 2\varphi_{13}\psi_{22} & 0 \\ \psi_{11}\psi_{33} + \psi_{11}\psi_{22} - \varphi_{13}^2 - \varphi_{12}^2 & \varphi_{13}\varphi_{23} + \varphi_{12}\psi_{33} & \varphi_{12}\varphi_{23} + \varphi_{13}\psi_{22} \\ \varphi_{13}\varphi_{23} + \varphi_{12}\psi_{33} & \psi_{22}\psi_{33} + \psi_{11}\psi_{22} - \varphi_{23}^2 - \varphi_{12}^2 & \varphi_{12}\varphi_{13} + \varphi_{23}\psi_{11} \\ \varphi_{12}\varphi_{23} + \varphi_{13}\psi_{22} & \varphi_{12}\varphi_{13} + \varphi_{23}\psi_{11} & \psi_{22}\psi_{33} + \psi_{11}\psi_{33} - \varphi_{23}^2 - \varphi_{13}^2 \end{pmatrix} \quad (2.3)$$

Where $\nabla = \psi_{11}\psi_{22}\psi_{33} - \varphi_{23}^2\psi_{11} - \varphi_{13}^2\psi_{22} - \varphi_{12}^2\psi_{33} - 2\varphi_{12}\varphi_{23}\varphi_{13}$ and $\psi_{ij} = \delta_{ij} - \varphi_{ij}$ and $\boldsymbol{\delta}$ is the Kronecker delta.

The damaged configuration elastic strain energy density is expressed assuming $W^e(\boldsymbol{\sigma}, \boldsymbol{\varphi} \neq 0) = W^e(\tilde{\boldsymbol{\sigma}}, \boldsymbol{\varphi} = 0)$ and written as follows:

$$W^e(\boldsymbol{\sigma}, \boldsymbol{\varphi}) = \frac{1}{2}\tilde{\boldsymbol{\sigma}} : \mathbb{C}^{-1} : \tilde{\boldsymbol{\sigma}} = \frac{1}{2}\boldsymbol{\sigma} : \tilde{\mathbb{C}}^{-1} : \boldsymbol{\sigma} \quad (2.4)$$

Where $\mathbb{C}^{-1}$ is the compliance tensor while the effective compliance tensor can be defined as:

$$\tilde{\mathbb{C}}^{-1} = \mathbb{M}^T : \mathbb{C}^{-1} : \mathbb{M} \quad (2.5)$$

2.3.2.2 Continuum Damage Plasticity

The coupling between the viscoplastic constitutive equations and damage is achieved by substituting the stress tensor in the plastic potential of defect-free material by the effective stress (Chow et al., 1997). Furthermore, the yield criterion f^p defined according to Hill (1948) for describing the anisotropic material plasticity is expressed as the difference between the effective equivalent plastic stress $\tilde{\sigma}_{Hard}^{eq}$ and the isotropic hardening term $R(p)$; $f^p = \tilde{\sigma}_{Hard}^{eq} - R(p) = 0$. Moreover, the Hill equivalent stress accounting for the kinematic hardening $\tilde{\sigma}_{Hard}^{eq}$ is defined as:

$$\tilde{\sigma}_{Hard}^{eq} = \left(\frac{1}{2}(\boldsymbol{\sigma} - \boldsymbol{b}) : \tilde{\mathbb{H}} : (\boldsymbol{\sigma} - \boldsymbol{b})\right)^{\frac{1}{2}} \quad (2.6)$$

Where $\boldsymbol{b}$ is the backstress described in section 2.3.2.3 that is used to describe the viscohyperelastic behavior. The stress is integrated from the stress rate, defined as a function of the elastic part of the rate of deformation tensor and the effective stiffness tensor $\tilde{\mathbb{C}}$:

$$\dot{\boldsymbol{\sigma}} = \tilde{\mathbb{C}}: [\boldsymbol{D} - \boldsymbol{D}^p] = \tilde{\mathbb{C}}: \boldsymbol{D}^e \tag{2.7}$$

And the hill effective is given by $\widetilde{\mathbb{H}} = \mathbb{M}^T: \mathbb{H}: \mathbb{M}$, where $\mathbb{H}$ is the Hill symmetric tensor of the fourth order, written as:

$$\mathbb{H} = \begin{bmatrix} h_{11} & h_{12} & h_{13} & 0 & 0 & 0 \\ h_{21} & h_{22} & h_{23} & 0 & 0 & 0 \\ h_{31} & h_{32} & h_{33} & 0 & 0 & 0 \\ 0 & 0 & 0 & h_{44} & 0 & 0 \\ 0 & 0 & 0 & 0 & h_{55} & 0 \\ 0 & 0 & 0 & 0 & 0 & h_{66} \end{bmatrix} \tag{2.8}$$

Where $h_{11} = G + H,\ h_{22} = H + F,\ h_{33} = F + G,\ h_{12} = h_{21} = -H,\ h_{13} = h_{31} = -G,\ h_{23} = h_{32} = -F,\ h_{44} = 2L,\ h_{55} = 2M,\ h_{66} = 2N$, and F, G, H, L, M, and N are the characteristic material constants describing the current state of anisotropy in the material. These constants can be determined from experimental tests as described by Hill (1948). The plastic rate of deformation is derived as:

$$\boldsymbol{D}^p = \boldsymbol{\lambda}^p \frac{\partial f^p}{\partial \boldsymbol{\sigma}} = \frac{\boldsymbol{\lambda}^p}{2\tilde{\sigma}_{Hard}^{eq}} \widetilde{\mathbb{H}}: (\boldsymbol{\sigma} - \boldsymbol{b}) \tag{2.9}$$

where $\boldsymbol{\lambda}^p$ is a directional plastic multiplier approximated by the directional cumulative plastic strain rate $\dot{\boldsymbol{p}}$ that represents the rate dependent plastic flow stress in shear. It accounts for the viscosity associated to chain segment rotation intermolecular barrier and the chain reptation during the alignment of chain along the loading direction through $\boldsymbol{b}$. The original mathematical representation of the plastic shear rate was proposed by Argon, (1973) and later used or modified by many investigation (Ahzi et al., 2003; J Richeton et al., 2006; Arruda et al., 1995; Ayoub et al., 2010c; Bergström and Boyce, 1998; van Dommelen et al., 2003; H. Abdul-Hameed et al., 2014;

Ayoub et al., 2011b, 2010b; Makki et al., 2017). The plastic shear rate is described by the following power law:

$$\dot{\boldsymbol{p}} = \gamma^{p} \left(\frac{\tilde{\sigma}^{eq}_{Hard}}{\boldsymbol{s}} \right)^{\frac{1}{m}} \tag{2.10}$$

Where m is the strain rate sensitivity parameter, γ^{p} represents the initial plastic rate, and $\boldsymbol{s}$ is the directional shear strength resistance that is chosen to evolve according to Stringfellow et al. (1992):

$$\dot{\boldsymbol{s}} = \dot{\boldsymbol{p}} \frac{\boldsymbol{s}}{n^{h}} \left(\frac{\boldsymbol{s}^{s}}{\boldsymbol{s}} \right)^{n^{h}} \tag{2.11}$$

Where n^{h} is a hardening coefficient and $\boldsymbol{s}^{\boldsymbol{s}}$ is the directional hardening saturation limit. The directional shear strength resistance $\boldsymbol{s}$ is equal to s^{0}at the onset of plasticity. The original formulation proposed by Stringfellow et al. (1992) considered the shear strength resistance to be constant. To account for the anisotropic hardening, we propose to consider the shear strength resistance as a tensor. The proposed formulation is intended to describe for some microporous films the different hardening coefficients measured when loading along different material directions. Accordingly, the hardening saturation limit is written as:

$$\boldsymbol{s}^{\boldsymbol{s}} = s^{0} * \begin{bmatrix} cf_{11} \\ cf_{22} \\ cf_{33} \\ cf_{23} \\ cf_{13} \\ cf_{12} \end{bmatrix} \tag{2.12}$$

Where cf denotes the directional coefficient of hardening.

2.3.2.3 Hyperelastic Backstress

Once the intermolecular barriers to chain motion is overcome by the polymeric material under large deformation, the chains of the macromolecular network stretch and tend to align along the direction of principal plastic stretch (Wu and van der Giessen, 1993). It is assumed that the

macromolecular alignment results into a kinematic hardening accounted for by using the back-stress. The evolution of the back-stress was initially proposed by Wu and Van Der Giessen (1993b). Furthermore, the backstress has been used to account for the dissipative behavior of polymers under cyclic loadings (Chowdhury et al., 2008; Cantournet et al., 2009). The Approximation of the full network is achieved by combining the three-chain and the eight-chain non-Gaussian network models in a linear equation.

$$\dot{\boldsymbol{b}} = \mathbb{R}: \boldsymbol{D^p} \tag{2.13}$$

$$\mathbb{R} = (1-\kappa)\mathbb{R}^{3-ch} + \kappa\mathbb{R}^{8-ch} \tag{2.14}$$

Where $\mathbb{R}^{3-ch}$ is the three-chain backstress tensor modulus and $\mathbb{R}^{8-ch}$ is the eight-chain backstress tensor modulus. $\lambda_{\max}$ is the maximum principal stretch, N represents the number of entanglements between crosslinks, and $\kappa = 0.85\frac{\lambda_{\max}}{\sqrt{N}}$,. The eight-chain model $\mathbb{R}^{8-\mathrm{ch}}$ is described as follow:

$$\mathbb{R}^{8-ch}_{ijkl} = \frac{1}{3}C^R\sqrt{N}\left[\left(\frac{\xi_c}{\sqrt{N}} - \frac{\beta_c}{\lambda_c}\right)\frac{B_{ij}B_{kl}}{B_{mm}} + \frac{\beta_c}{\lambda_c}\left(\delta_{ik}B_{jl} + B_{ik}\delta_{jl}\right)\right] \tag{2.15}$$

Where C^R is the rubbery modulus, $\boldsymbol{B} = \boldsymbol{F}.\ \boldsymbol{F}^T$ is the left Caushy-Green tensor, δ_{ij} is the Kronecker delta, $\lambda_c^2 = \frac{1}{3}trace(\boldsymbol{B})$, $\beta_c = \mathcal{L}^{-1}\left(\frac{\lambda_c}{\sqrt{N}}\right)$ where the Langevin function is defined as $\mathcal{L}(x) = \coth x - \frac{1}{x}$, and $\xi_c = \frac{\beta_c^2}{1-\beta_c^2\,\mathrm{csch}^2\,\beta_c}$.

The three-chain model is described as follow:

$$\mathbb{R}^{3-ch}_{IJKL} = \begin{cases} \frac{1}{6}C^R\sqrt{N}\lambda_I^2\left(\frac{\xi_I}{\sqrt{N}} + \frac{\beta_I}{\lambda_I}\right)\left(\delta_{IK}\delta_{JL} + \delta_{JK}\delta_{IL}\right) & if\ I = J \\ \frac{1}{6}C^R\sqrt{N}\frac{\lambda_I^2 + \lambda_J^2}{\lambda_I^2 - \lambda_J^2}\left(\lambda_I\beta_I - \lambda_J\beta_J\right)\left(\delta_{IK}\delta_{JL} + \delta_{JK}\delta_{IL}\right) & if\ I \neq J \end{cases} \tag{2.16}$$

The three-chain model is expressed in terms of the principal stretch, where I, J, and K are the principal directions. In this model, if $\lambda_I = \lambda_J$ with $I \neq J$, then the first equation is used. β_I and ξ_I are given as $\beta_I = \mathcal{L}^{-1}\left(\frac{\lambda_I}{\sqrt{N}}\right)$, and $\xi_I = \frac{\beta_I^2}{1-\beta_I^2 \operatorname{csch}^2 \beta_I}$.

2.3.2.4 Damage Evolution

In this section, the constitutive equations for the damage evolution are described. The concept of damage potential f^d is proposed in analogy to the yield surface with $f^d = Y^{eq} - Z(q) = 0$, with Y^{eq} being the equivalent elastic energy release rate associated with damage, and $Z(q)$ is associated with damage strengthening. The damage evolution rate is expressed according to Kassar et al. (2019) as:

$$\dot{\boldsymbol{\varphi}} = -\frac{\lambda^d}{2Y^{eq}} \mathbb{L}^d : \boldsymbol{Y} \tag{2.17}$$

Where λ^d is the Lagrangian multiplier term approximated by the plastic damage rate accumulation $\dot{q}$ described by power-law. $\mathbb{L}^d$ is a fourth-order plastic damage characteristic tensor:

$$\mathbb{L}^d = \begin{bmatrix} 1 & \eta & \eta & 0 & 0 & 0 \\ \eta & 1 & \eta & 0 & 0 & 0 \\ \eta & \eta & 1 & 0 & 0 & 0 \\ 0 & 0 & 0 & \frac{1}{2}(1-\eta) & 0 & 0 \\ 0 & 0 & 0 & 0 & \frac{1}{2}(1-\eta) & 0 \\ 0 & 0 & 0 & 0 & 0 & \frac{1}{2}(1-\eta) \end{bmatrix} \tag{2.18}$$

Where η is a material constant that can be found experimentally, and the power law describing the plastic damage rate accumulation is as follows:

$$\lambda^d \approx \dot{q} = \gamma^d \left(\frac{Y^{eq}}{Y^0}\right)^{\frac{1}{n}} \tag{2.19}$$

Where γ^d is the reference damage rate, Y^0 is the damage resistance to strengthening, and n is a rate dependence parameter. The viscoplastic deformation contributes to the damage in the associated equivalent elastic energy release rate which is defined as:

$$\boldsymbol{Y} = -\boldsymbol{\sigma}:\left\{\mathbb{C}^{-1}:\mathbb{M}:\frac{\partial \mathbb{M}}{\partial \boldsymbol{\varphi}}\right\}^{s}:\boldsymbol{\sigma} \tag{2.20}$$

Where superscript "s" is used to indicate that only the symmetric part of the tensor within the curly brackets is used. Finally, the effective equivalent elastic energy release rate associated with damage is defined as:

$$Y^{eq} = \left(\frac{1}{2}\boldsymbol{Y}:\mathbb{L}^{d}:\boldsymbol{Y}\right)^{\frac{1}{2}} \tag{2.21}$$

2.3.3 Time Integration Method

The constitutive equations presented in section 2.3.2 were integrated using an implicit integration algorithm. In this section the main elements of the proposed implementation are summarized. The 18 state variable were collected in one vector X such that:

$$\boldsymbol{X}^T = [\sigma_{11}\ \sigma_{22}\ \sigma_{33}\ \sigma_{23}\ \sigma_{13}\ \sigma_{12}\ \varphi_{11}\ \varphi_{22}\ \varphi_{33}\ \varphi_{23}\ \varphi_{13}\ \varphi_{12}\ b_{11}\ b_{22}\ b_{33}\ b_{23}\ b_{13}\ b_{12}] \tag{2.22}$$

The system of nonlinear equations is solved using an implicit time integration scheme. For instance, the stress is approximated as:

$$\sigma_{ij}^{t+1} = \sigma_{ij}^{t} + \dot{\sigma}_{ij}^{t+1}\Delta t \tag{2.23}$$

Where t is the preceding time step and Δt is the time increment. The residuals of each state variable are then computed as follow:

$$R_{\sigma_{ij}}^{t+1} = \frac{\sigma_{ij}^{t+1} - \sigma_{ij}^{t}}{\Delta t} - \dot{\sigma}_{ij}^{t+1} \tag{2.24}$$

$$R_{\varphi_{ij}}^{t+1} = \frac{\varphi_{ij}^{t+1} - \varphi_{ij}^{t}}{\Delta t} - \dot{\varphi}_{ij}^{t+1} \tag{2.25}$$

$$R_{b_{ij}}^{t+1} = \frac{b_{ij}^{t+1} - b_{ij}^{t}}{\Delta t} - \dot{b}_{ij}^{t+1} \tag{2.26}$$

Since the damage is defined in the material coordinate system, all the residuals are collected in one residual vector as:

$$[\boldsymbol{R}]^T = \left[R_{\sigma_{11}} R_{\sigma_{22}} R_{\sigma_{33}} R_{\sigma_{23}} R_{\sigma_{13}} R_{\sigma_{12}} R_{\varphi_{11}} R_{\varphi_{22}} R_{\varphi_{33}}\ R_{\varphi_{23}}\ R_{\varphi_{13}}\ R_{\varphi_{12}} R_{b_{11}} R_{b_{22}} R_{b_{33}} R_{b_{23}} R_{b_{13}} R_{b_{12}}\right] \quad (2.27)$$

The state variables of the previous increment $[\boldsymbol{X}]^t$ are used as initial guesses in the Newton-Raphson constitutive updating method to compute the state variables at the current increment $[\boldsymbol{X}]^{t+1}$ as follows:

$$[\boldsymbol{X}]^{t+1} = [\boldsymbol{X}]^t - inv[\boldsymbol{J}]^{t+1}[\boldsymbol{R}]^{t+1} \quad (2.28)$$

Where inv is the inverse of the Jacobian matrix $\boldsymbol{J}$. The Jacobian 18x18 matrix is expressed as follows:

$$[\boldsymbol{J}]^{t+1} = \left[\frac{\partial[\boldsymbol{R}]}{\partial[\boldsymbol{X}]}\right]_{18\times 18}^{t+1} = \left[\frac{\partial R_{X_i}}{\partial X_j}\right]^{t+1} \quad (2.29)$$

For convergence purposes, a consistent tangent matrix ($\mathbb{Q}$) is calculated as follows:

$$\mathbb{Q} = \frac{1}{\Delta t}\left(-\left[\frac{\partial[\boldsymbol{R}]}{\partial[\boldsymbol{X}]}\right]^{-1}\tilde{\mathbb{C}}\right) \quad (2.30)$$

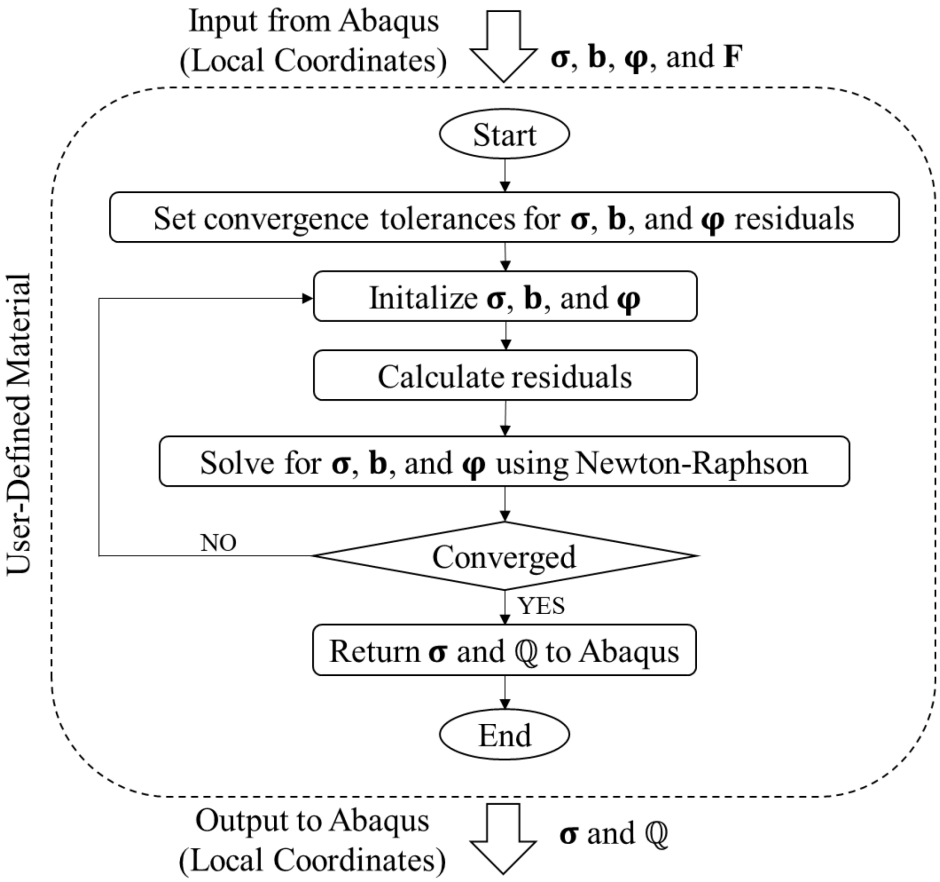

Figure 2.5: Flowchart of the implicit integration algorithm.

The constitutive model was implemented in Abaqus as a user subroutine for modeling battery separator structures. The subroutine flow diagram is shown in Figure 2.5 and the details of the numerical implementation are provided in Appendices A and B. The consistent tangent matrix $\mathbb{Q}$ is computed at each time step after the Newton-Raphson convergence criterion is met and then supplied to Abaqus. All the calculations were conducted in the local material coordinate system then transformed to the global coordinate system of Abaqus.

2.4 Model Validation and Discussion

In this section, a parametric sensitivity analysis is conducted in view of which a parameter identification procedure is proposed. The model parameters were identified on uniaxial tensile

tests along different material's directions and the model prediction capability was validated on punch tests. In this section we first discussed the studied material (PE separator) and then the versatility of the proposed constitutive behavior was verified on a battery separator investigated by Zhang et al. (2017) (trilayer PP-PE-PP separators).

2.4.1 Parameters Sensitivity Analysis and Identification

In the following subsection, the calibration procedure for the constitutive model parameters is explained. The goal is to describe a clear model-parameters identification procedure using tensile load displacement data obtained along different material directions.

The elastic properties of the PE films were identified using the modified rule of mixture relating the elastic modulus and the crystal volume fraction proposed by Ayoub et al., (2011b). The elastic modulus of the base material is estimated to be equal to $E = 1500$ MPa. It is worth noting that the estimated elastic modulus cannot be directly measured from the experimental tensile data since the studied material is porous. Indeed, the studied PE battery separator has a foamy structure with the initial porosity being equal to 43%. The experimentally measured elastic modulus $\tilde{E}$ can be related to the base material elastic modulus E using the following equation $\varphi = 1 - \tilde{E}/E$.

Remark 1: It is worth noting that a direct relationship between the damage (surface property) and the porosity (volume property) does not exist unless the geometry of the pores is well defined. From the engineering stress strain curves presented in Figure 2.2, we notice that the elastic modulus is not the same in the three different directions. The initial damage along the MD direction is estimated to be equal to $\varphi_{11} = 0.18$, while the initial damage along TD is estimated to be equal to $\varphi_{22} = 0.23$. The initial damage in all other directions was taken to be equal to 0.

The anisotropic flow rule described in subsection 2.3.2.2 is used to describe the Hill anisotropic effective stress (Equation 2.6) (Chow et al., 1997; Hill 1948). The Hill symmetric tensor of fourth-order $\mathbb{H}$ is written as a function of six anisotropy parameters, F, G, H, L, M, and N, that are determined from experimental tests as described by Hill (1948). The planar tensile yield stresses in the MD (Z_{11}), TD (Z_{22}), and DD (Z_{12}) were determined experimentally from Figure 2.2. The Hill 48 anisotropic parameters were determined using the following set of equations:

$$\begin{cases} F = \frac{1}{2}\left(\frac{1}{Z_{22}^2} - \frac{1}{Z_{11}^2} + \frac{1}{Z_{33}^2}\right) Z_0^2 \\ G = \frac{1}{2}\left(\frac{1}{Z_{11}^2} - \frac{1}{Z_{22}^2} + \frac{1}{Z_{33}^2}\right) Z_0^2 \\ H = \frac{1}{2}\left(\frac{1}{Z_{11}^2} + \frac{1}{Z_{22}^2} - \frac{1}{Z_{33}^2}\right) Z_0^2 \\ N = \left(\frac{3}{2Z_{12}^2}\right) Z_0^2 \\ M = L = N \end{cases} \tag{2.31}$$

Z_0 is a reference yield stress that is equated with the yield stress in the MD direction. Z_{33} is the yield stress through the thickness that was assumed equal to the Z_{22}. Table 2.2 lists the identified Hill 48 anisotropic parameters.

Table 2.2: The Hill 48 anisotropic parameters.

Parameter	h_{11}	h_{22}	h_{33}	h_{66}
PE	0.2	0.3	0.35	6
PE/PP/PE	0.5	4.3	2.0	6

Remark 2: The anisotropy in the mechanical behavior of battery separators was accounted for through the Hill 48 anisotropic effective stress and through the anisotropic damage tensor. To understand the effect of those approaches on the overall numerical anisotropic response, a parameters sensitivity study was conducted. First, the effect of Hill parameters on the overall

behavior was assessed by evolving only the h_{11}, as shown in Figure 2.6.a. It can be observed that the Hill parameters influence the yielding and the strain hardening but have no effect on the elastic properties. Figure 2.6.b shows the effect of the initial damage on the overall behavior of the material.It can be observed that the initial damage influences the elasticity and yielding but has no effect on the hardening. Indeed, the effective compliance tensor (in the current damaged configuration) is a function of the fourth-order damage effect tensor $\mathbb{M}$ and the compliance tensor (in the fictive undamaged configuration). Hence, with increasing initial damage, the $\mathbb{M}$ decreases, the effective compliance tensor increases, and the stiffness tensor decreases. Furthermore, the plastic rate of deformation is written as a function of the effective stress tensor (in the fictive undamaged configuration) that increases with increasing damage leading to a decrease in the yield stress.

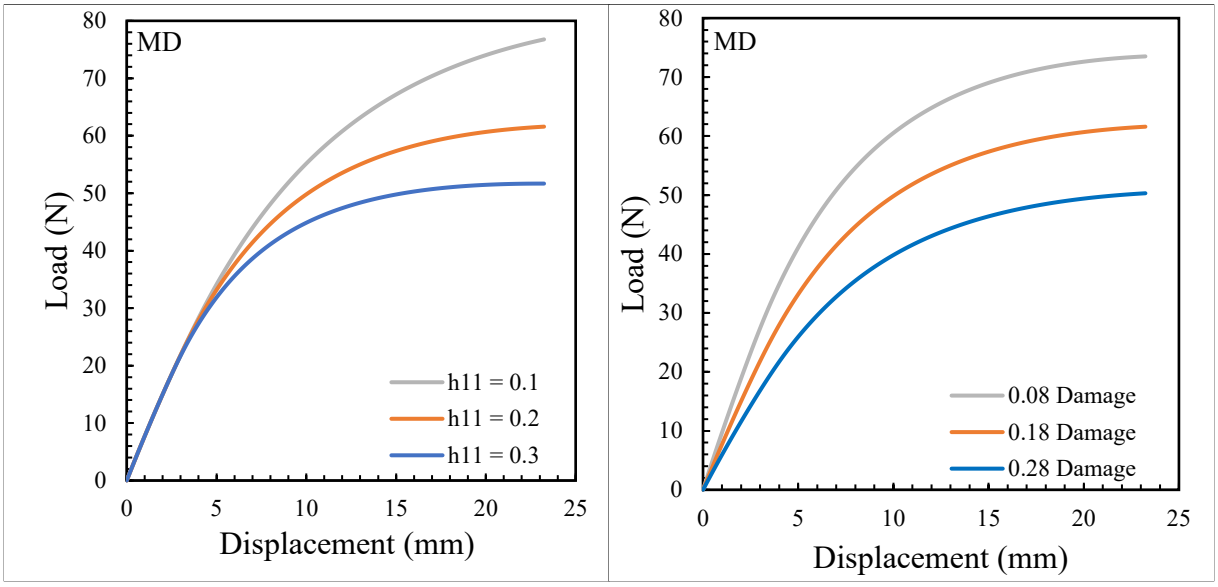

(a) (b)

Figure 2.6: (a) Effect of Hill, (b) effect of initial damage.

The initial shear resistance s^0 can be identified at yielding from the experimental data using Equation 10. To determine the initial shear resistance, Equation 10 is reformulated as follows:

$$s^0 = \sigma_{Hard}^{eq} * \left(\frac{\dot{p}}{\gamma^p}\right)^{-m} \tag{2.32}$$

In which $\tilde{\sigma}_{Hard}^{eq}$ is the experimentally measured stress at yielding divided by $\sqrt{3}$, and at-yielding $\dot{p}$ is approximated as $\sqrt{3} * \dot{\varepsilon}$, where $\dot{\varepsilon}$ is the strain rate.

Remark 3: The mechanical behavior of the battery film presented an anisotropic hardening since variable hardening rates were observed for different loading directions. The anisotropic hardening is associated with the manufacturing process of the films that leads to the alignment of chains in the direction of processing (machine direction). While the hardening along the machine direction is associated with molecular chain stretching and the formation of new fibrils that cause significant strain hardening, the hardening along the transverse direction is associated with enlargement of pores, buckling of molecular chains, and narrowing of the bulk region (lamellae blocks).

The difference in the hardening mechanisms is accounted for through Equation 12, and the parameters were fitted onto the experimental results. To understand the proposed anisotropic hardening approach, a parametric study was conducted to examine the effect of different hardening coefficients on the loading displacement curves. The hardening coefficient for the machine direction was varied between a value of 1 and 5, and the resulting curves are shown in Figure 2.7. At a value of 1, the material behaves as a typical thermoplastic, while increasing the coefficient of hardening directly affects the mechanical behavior after yielding, causing a significant increase in the flow load. These curves show the model's ability to represent the anisotropic hardening for a specific direction by changing the hardening coefficient. Implementing a directional coefficient of hardening representing the material's resistance to deformation allows for a more accurate prediction of the mechanical behavior in a specific material direction. Indeed, we previously mentioned that dry-process separators exhibit significant anisotropic hardening behavior that cannot be depicted by anisotropic yielding and damage. Although the wet-process PE separator

exhibited a lower anisotropic hardening compared with the dry-processed separator, the different deformation mechanisms active along different loading directions need to be considered.

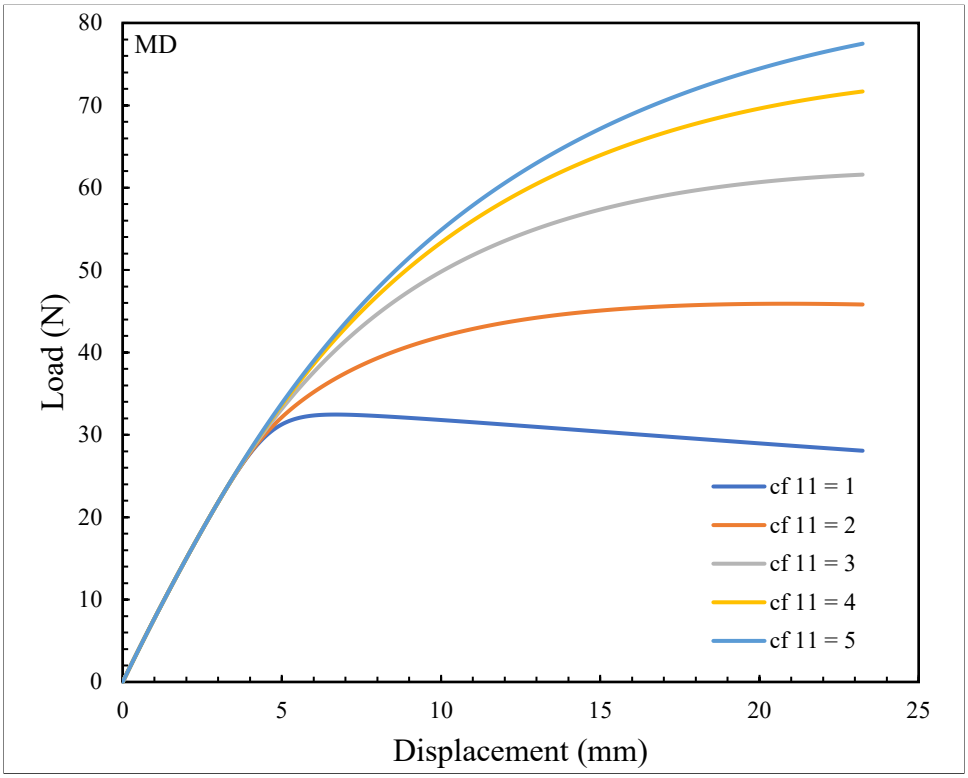

Figure 2.7: Load vs Displacement for different hardening saturation limit.

The deformation mechanisms that lead to fracture in battery separators are associated with (1) the separation of crystalline lamellae into crystal blocks and (2) the elongation of the fibrils along the loading direction, followed by (3) breakages of crystal blocks and (4) disintegration into fibrils at high strains. Furthermore, the existing pores grow and coalesce in addition to the nucleation of new pores. At high strains, voids coalescence is associated with the breakage of fibrils connecting existing pores (Zhang et al., 2016a). Void coalescence results in a macroscopic crack that ultimately leads to fracture. The proposed constitutive model phenomenologically accounts for those mechanisms leading to fracture through the damage evolution equations. The parameters of the damage evolution presented by Equation 17 were identified by fitting the

experimental fracture strain. Three damage parameters were identified: the initial damage rate γ^d, the damage strengthening resistance Y^0, and the rate sensitivity parameter n. The damage rate sensitivity parameter n controls the damage rate evolution at different strain rates. Since the strain rate effect was not assessed in this study the strain rate effect was minimized by taking $n = 0.2$. The initial damage rate γ^d directly controls the rate at which failure occurs, while Y^0 corresponds to the damage yielding threshold. A combination of both Y^0 and γ^d was fitted for each studied material to predict the strain at failure accurately. We used the same backstress parameters (Cr and N) as the one previously identified by the authors on similar material (Ayoub et al., 2011b; Makki et al., 2017). Table 2.3 lists the constitutive model parameters identified for each type of separator based on solely the tensile behavior along different material directions.

2.4.2 Uniaxial Tension Modelling

The presented uniaxial tension experimental results of both polyethylene and trilayer (PP/PE/PP) separators showed distinct properties in the three tested material directions. The dry-processed trilayer separator (Zhang et al., 2017) exhibited distinct anisotropic yielding and anisotropic hardening while a subtle anisotropic behavior was exhibited by the wet-processed PE. The uniaxial tensile specimens of the battery separators were modeled using Abaqus finite element with shell elements. The small thickness of the separator films prompted the use of shell elements. Only a quarter of the sample was modeled; therefore, three sides of the model were assigned symmetry conditions. The UMAT was written in the material coordinate system with X, Y, and Z axes being aligned with MD, TD, and ND (normal through thickness direction). The simulation of the uniaxial loading along different material directions was performed by rotating the material coordinate system along the Z-axis of the global coordinate system of Abaqus (which is equivalent to the Z axis of the material direction). Hence, when loading along the TD direction, the global

and the material coordinate systems are aligned. The different tensorial variables were computed in the material coordinate system and then transformed into the Abaqus global coordinate system.

Table 2.3: Parameters identification.

Material Constants		**PP/PE/PP**	**PE**
Young's modulus (MPa)	E	1200	1500
Poisson's ratio	ν	0.45	0.49
Plasticity Parameters			
Shear resistance (MPa)	s^0	6	14
Hardening saturation limit $s^s = s^0 * cf$ (MPa)	cf_{11}	6.5	3.0
	cf_{22}	1.6	3.5
	cf_{33}	1.0	1.0
	cf_{23}	1.0	1.0
	cf_{13}	1.0	1.0
	cf_{12}	2.0	6.0
Fitted hardening coefficient	n^h	3	5
Strain rate sensitivity parameter	m	0.2	0.1
Initial plastic rate (s^{-1})	γ^p	1e-6	1e-6
Backstress Parameters			
Rubbery modulus (MPa)	C^R	1.45	1.45
Number of entanglements	N	50	50
Damage Parameters			
Initial damage rate	γ^d	5e-19	8e-19
Damage strengthening resistance	Y^0	0.05	0.02
Damage rate sensitivity parameter	n	0.2	0.2

As aforementioned, the plasticity and damage parameters were identified by using the previously described approach and by minimizing the difference between the model results and the tensile engineering stress vs. strain experimental curves. The Hill 48 parameters and the

hardening coefficients were identified using the MD, DD, and TD yielding stress. The comparison between the experimental and the finite element uniaxial tensile test results along three material directions are shown in Figure 2.8. Moreover, the damage evolution along the loading direction is also plotted. In Figure 2.8, the solid lines represent the experimental data, while the dashed lines represent the Abaqus simulation results. The predicted fracture point by the simulation is marked by an x. It is observed that the anisotropic continuum damage coupled elastic-hyperelastic-viscoplastic model is able to capture the mechanical behavior of the PE separator. Indeed, very good fits between the model and the experimental results are observed for the MD and TD tensile loadings. More precisely, the elasticity, yielding, and plastic hardening up to fracture are captured accurately by the model. Although an acceptable fit between the model and the experimental results are observed for the DD tensile test, qualitatively a higher error is noticed when compared with the two other loading directions. Indeed, a lower fitting accuracy is observed between the model and the experiments in the DD direction when capturing the plastic hardening behavior. As previously described, the films' initial porosity was accounted for in the model by inputting the initial damage along the MD $\varphi_{11} = 0.18$ and TD $\varphi_{22} = 0.23$. When separators are stretched/deformed, the model predicts the development of damage that evolves nonlinearly in all material directions, with the highest values being estimated along the loading direction. The damage exhibits a very slow increase followed by a rapid increase just before structural failure is observed. The nonlinear damage evolution can be divided into two zones: (1) a very slow increase in the damage associated at the meso-scale with the elongation of polymer fibers and pores along the loading direction and at the micro-scale with the alignment of the polymer molecular chains in the direction of the applied stress and separation of crystalline lamellae into crystal blocks, and (2) a rapid increase in the damage associated at the micro-scale with sliding and disintegration of

crystal blocks and polymer molecular chains reaching their extensibility limits and rupturing, which result at the meso-scale and macro-scale in voids growth and coalescence that ultimately lead to structural failure.

Remark 4: Numerically, the fracture point (at increment n) coincides with the sudden increase of the damage and the subsequent increment (increment n+1) leads to a damage equal to or higher than 1. Moreover, the sudden increase in the damage causes a decrease in the engineering stress right before the fracture. The time step used in the simulations was optimized, and the simulation results are insensitive to the number of increments or the time step.

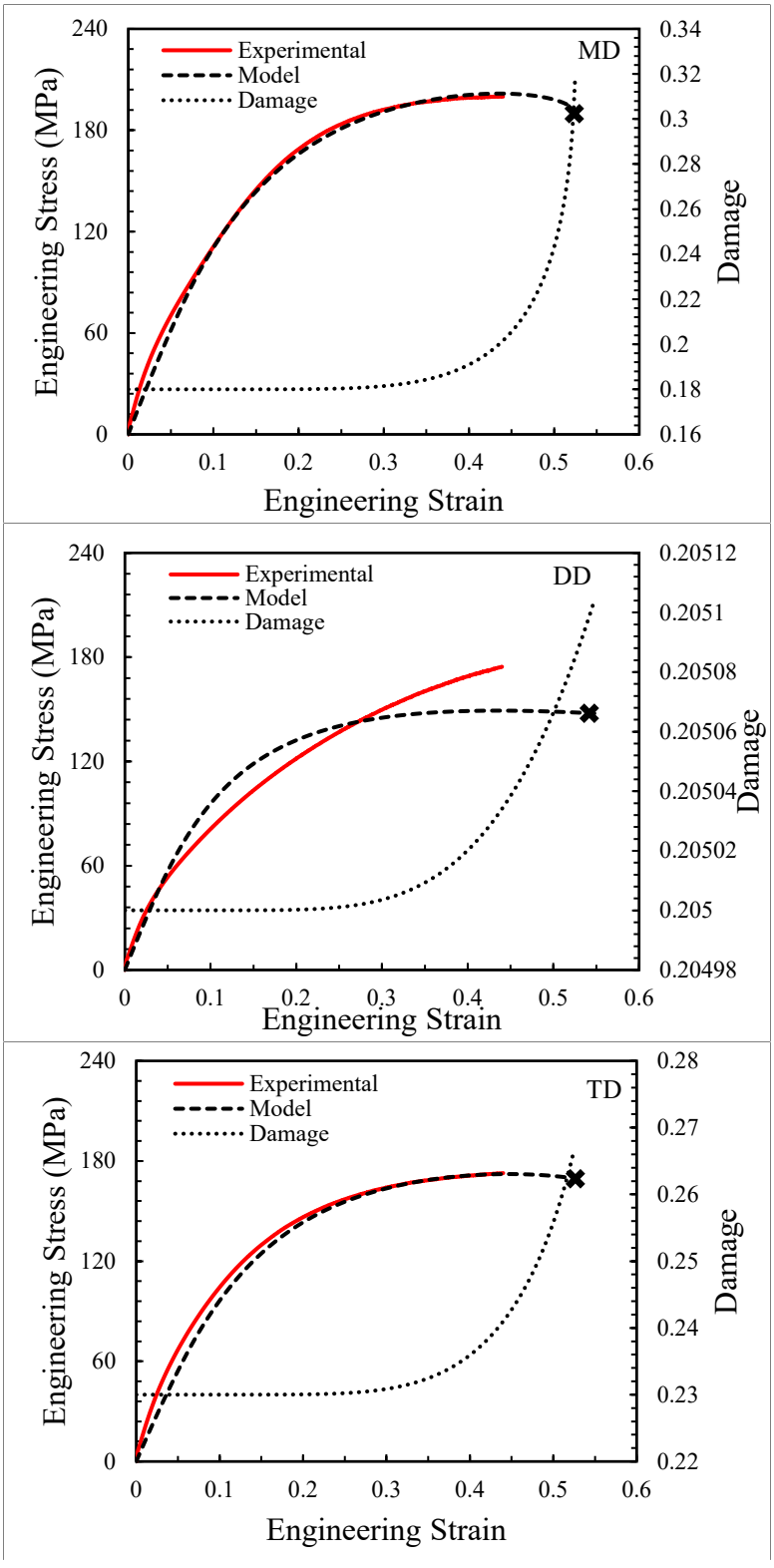

Figure 2.8: Comparison between experimental data and simulation results for the engineering stress-strain of PE separator.

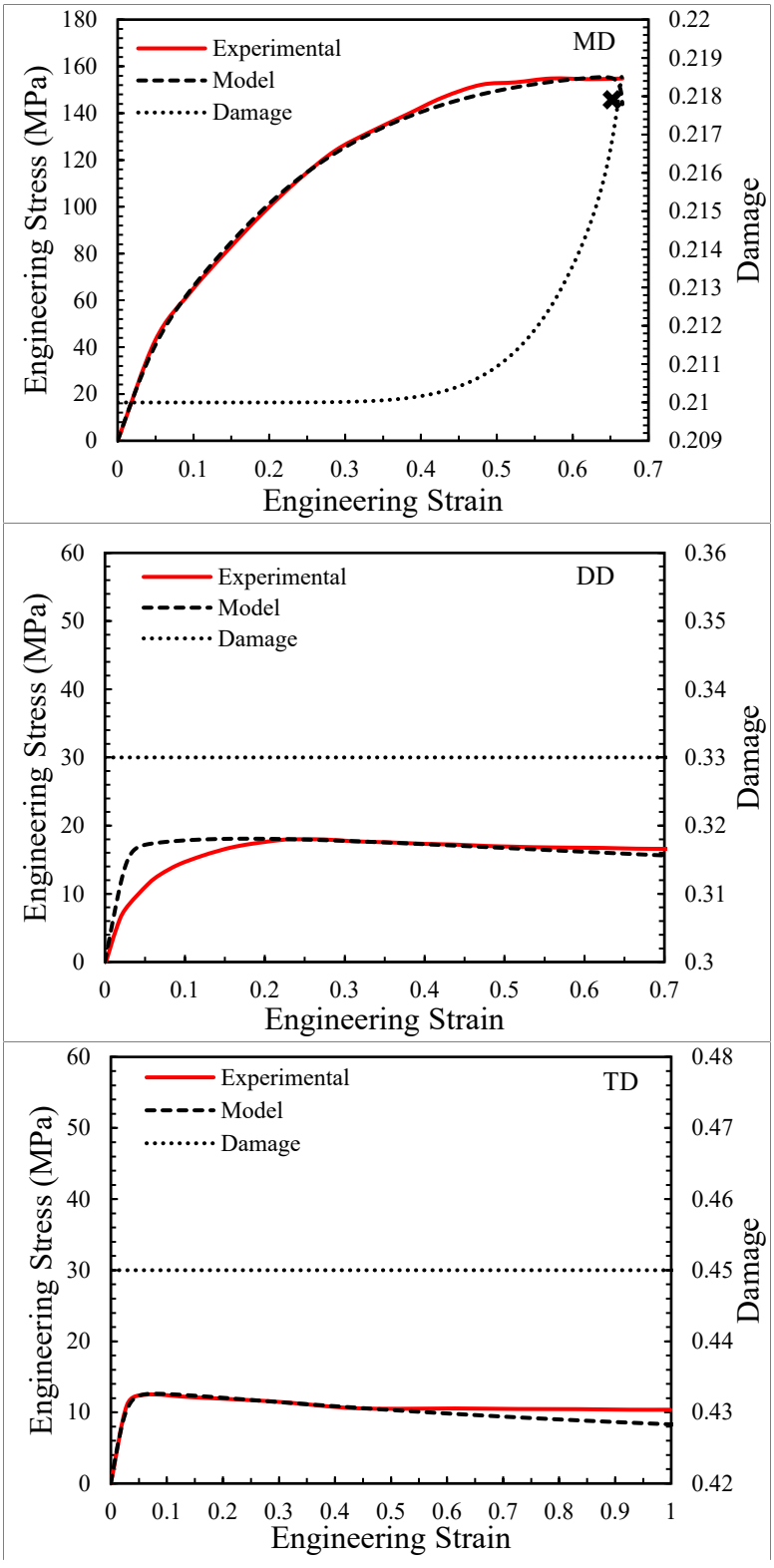

Figure 2.9: Comparison between experimental data and simulation results for the engineering stress-strain of trilayer separator.

The model's capability to capture the behavior of a highly anisotropic trilayer (PP-PE-PP) separator published by Zhang et al. (2017) is now evaluated. The model parameters were calibrated to capture the behavior of the trilayer separator using the process described in section 2.4.1. Figure 2.9 presents the comparison between the experimental and finite element uniaxial tensile test results along three material directions. Moreover, the damage evolution along the loading direction is also plotted. In Figure 2.9, the solid lines represent the experimental data (Zhang et al., 2017) while the dashed lines represent the Abaqus simulation results. The fracture point predicted by the simulation is marked by an x. It is observed that the highly anisotropic behavior of the trilayer (PP-PE-PP) separators was captured adequately by the anisotropic continuum damage coupled elastic-hyperelastic-viscoplastic model. Indeed, very good fit between the model and the experimental results are observed for the MD, DD, and TD tensile loadings. The elasticity, yielding, and plastic hardening up to fracture are captured accurately by the model. The high anisotropy with a significant higher strength along MD compared to the stresses along TD and DD is also captured by the model. Although an acceptable fit between the model and the experimental results is observed for the DD tensile test, qualitatively the error is higher when compared with the two other loading directions. Indeed, a lower fitting accuracy of the elastoplastic rollover transition between the model and the experiments in the DD direction is observed. Fracture was accurately captured in MD, with experimental and modeling fracture strain being ~ 0.66. While the damage accumulation is nonlinear, the damage accumulation rate is very small in the elastic and plastic region and then increases very quickly when fracture is forthcoming. Zhang et al. (2016b) reported that the fracture strain of the trilayer (PP-PE-PP) separators for DD and TD uniaxial tensile tests is around 2.0. Hence, the slight evolution of the damage predicted by the model for the DD and TD uniaxial tensile tests is in compliance with the experimental results.

Remark 5: We would like to point out that the damage results are reported based on boundary-value problems and for only one specific node (presenting the highest damage values). Hence, the reported damage evolutions do not represent the overall damage evolution of the structure which would be very challenging to map with experimental damage assessment. A larger error between the experimental and the model were observed for the DD directions Figure 2.8 and 2.9. The model does not accurately capture the transition from elastic regime to plastic regime for the DD samples. Additional investigations are needed to uncover the mechanisms controlling the deformation of the foam films in the elasto-plastic transmission region. We can only hypothesis that the error is induced by the realignment of the material fibers along the loading direction in the DD samples. Indeed, the pores present a privileged orientation (producing the anisotropic behavior) as can be seen in Figure 2.1. When applying a tensile loading along the DD direction an instability can take place when transitioning from the elastic regime to plastic regime. This phenomenon is not accounted for by the proposed model.

2.4.3 Punch Test Model Validation

In this section the capability of the model to predict the punch test results of both studied separators is assessed. The boundary value problems representing the punch test were solved using Abaqus finite element software. The small thickness of the separator films prompted the use of shell elements, while a rigid shell body was used for the punch. The FEM punch model is divided into two parts: the separator film and the punch (two different punch sizes were used, d_p= 3.2 and 12.7 mm). The punch models for both punch diameters are shown in Figure 2.10. Only a quarter of the separator was modeled; hence, symmetry boundary conditions were used for each side of the separator, and the quarter-circle perimeter was pinned in all directions. This was done to simplify the FEM simulations and decrease the simulation time. Initially, the punch was placed

above the separator with a 1 mm gap and was constrained to upward or downward movements; no rotation was allowed. The punch moves at a constant velocity, simulating the experimental setup. In order to examine the model's ability to predict the mechanical behavior of the separator under punch loading conditions, the parameters identified in section 2.4.1 were used.

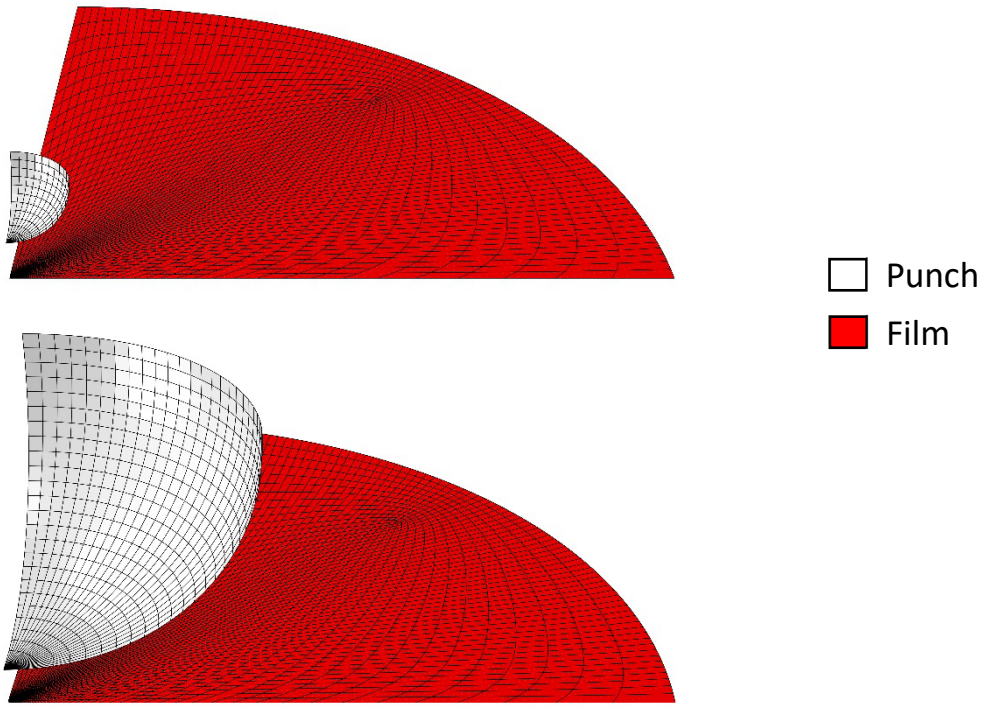

Figure 2.10: Finite element model for punch test: (top) 3.2 mm punch diameter, (bottom) 12.7 mm punch diameter.

The punch test simulation results are shown for the PE and the trilayer separators in Figure 2.11. Experimental load-displacement plots are depicted using solid lines, while dashed lines are used to represent the predicted load-displacement plots. The evolution of the maximum damage is shown using dotted lines, and an x symbol is used to indicate the predicted fracture point, which correlates with the rapid increase in the maximum damage. Figure 2.11 shows that the model is predicting with acceptable accuracy the mechanical and fracture behavior of both separators

subjected to punch loading using two different punch diameters. Indeed, a very good fit between the model and the experimental results is observed. More precisely, for the PE separator, the simulation results show a maximum difference with the experimental results of 1 Newton for the 3.2 mm punch diameter and 1.5 Newton for the 12.7 mm punch diameter. For the trilayer separator, the model predictions are in good agreement with the experimental data for the 3.175 mm punch diameter, while a small deviation with a maximum difference of 1 Newton is observed for the 12.7 mm punch diameter. More precisely, the model is capable of predicting the steady, almost linear increase up to failure of the load-displacement results for the 3.2 mm punch diameter. Additionally, the initial steady linear increase up to a 3mm displacement (for the PE separator) followed by a slow counterclockwise rollover to a higher-slop linear increase up to failure of the load-displacement results was predicted by the model for the 12.7 mm punch diameter.

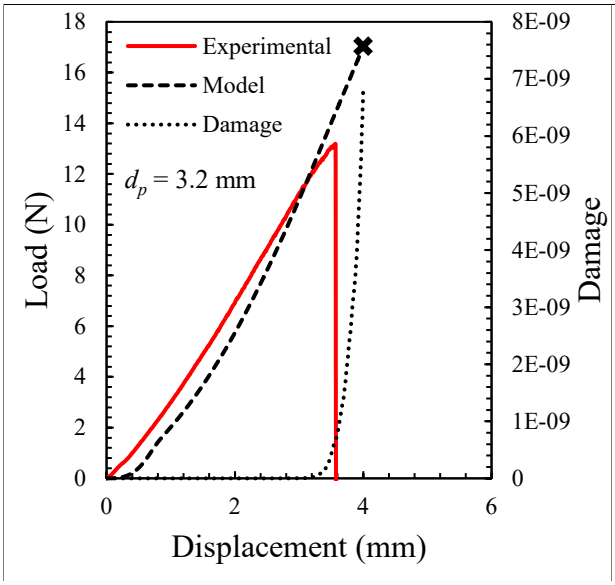

(a)

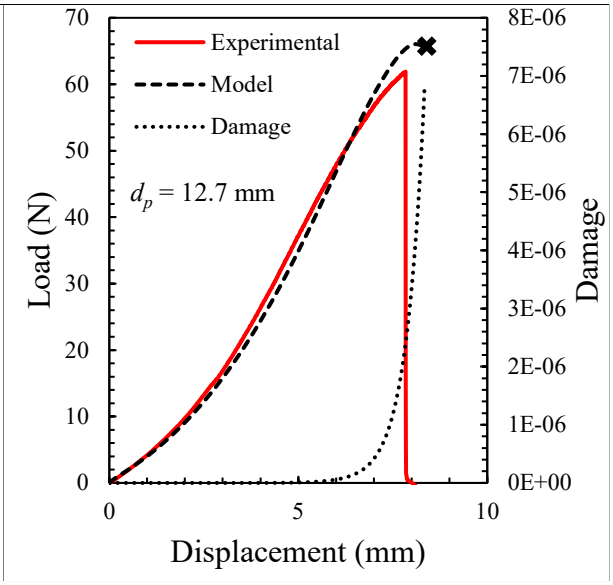

(b)

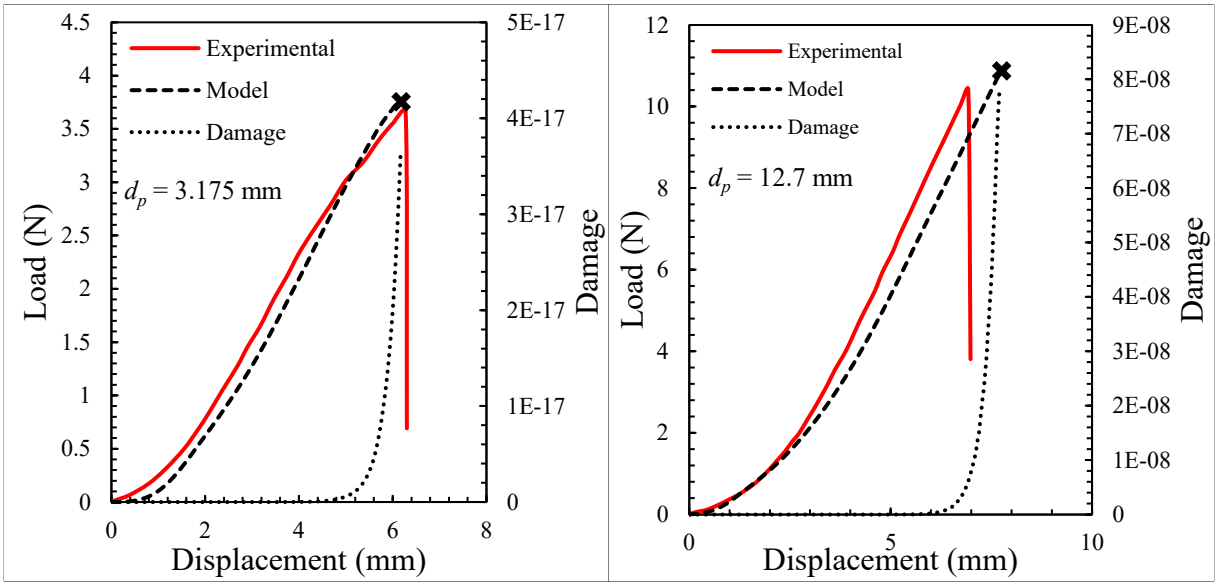

Figure 2.11: Comparison between experimental data and simulation results of the punch test in terms of force vs displacement of (a) and (b) for PE separator (c) and (d) for trilayer separator.

The FE model can predict accurately the mechanical response for both types of separators (dry- and wet-processed). Moreover, the model is also able to predict the fracture of the separator under biaxial punch loading. As mentioned previously, fracture occurs when the maximum damage increases rapidly. Even though the three damage variables are computed (along the 11, 22, and 12 directions), only the damage in the 12 direction is plotted in Figure 2.11. Indeed, the model predicts that the φ_{12} is the maximum damage developed under biaxial punch modeling. The experimental and the model-predicted fracture strains for all punch loading conditions are shown in Table 2.4. The highest percent error between the model fracture prediction and the experimental fracture is ~ 11 % for PE for the punch diameter of 3.2 mm.

Table 2.4: Experimental fracture and model predicted fracture.

Separator	Punch Diameter	Experimental Fracture	Model Predicted Fracture	Percent Error (%)
Polyethylene	3.2 mm	3.57	3.99	11.76
	12.7 mm	7.83	8.34	6.51
Trilayer	3.175 mm	6.30	6.15	2.38
	12.7 mm	6.98	7.69	10.17

Figures 2.12 shows for both punch diameters the deformed configuration of the PE separator just before reaching fracture (the top figures are for the 3.2 mm punch diameter and the bottom figures are for the 12.7 mm diameter). A side view of the punch sample FE model shows the damage distribution just before reaching fracture. While the stress distribution is shown from a top view. The experimental fracture for PE showed a slit along MD. For the 3.2 mm punch diameter, the predicted damage and the stresses are distributed along MD. The fracture in the model is predicted by the fast increase in the damage and fracture is supposed to take place at the nodes exhibiting the highest damage. The 3.2 mm punch simulations show that the highest damage is localized in the middle of the sample with a damage distribution along MD. The location and shape of the damage distribution is in correlation with the shape of the experimental fracture. For the 12.7 mm punch diameter, the stress is localized in the middle of the separator with some distribution in MD. The 12.7 mm punch simulations show that the highest damage is localized in the middle of the sample with a limited damage distribution along MD which is probably resulting from the large punch size. The location and shape of the damage distribution is in correlation with the shape of the experimental fracture.

Damage 12

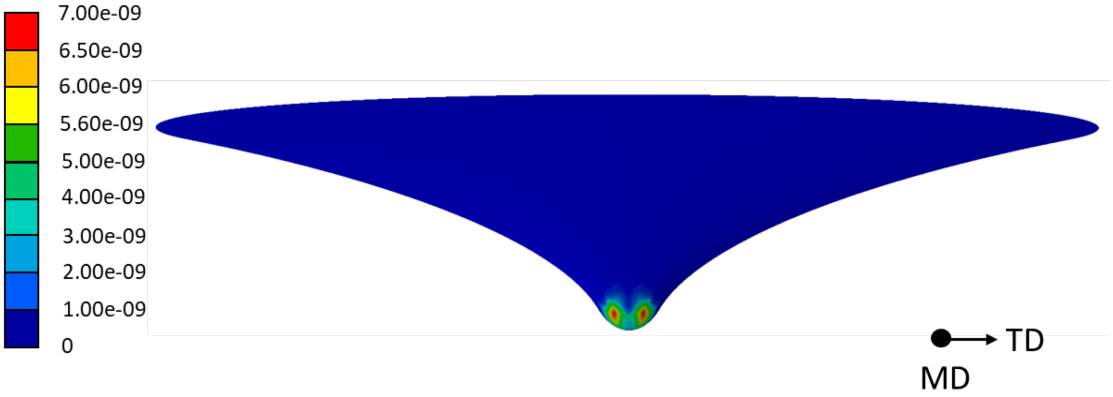

Stress(MPa)

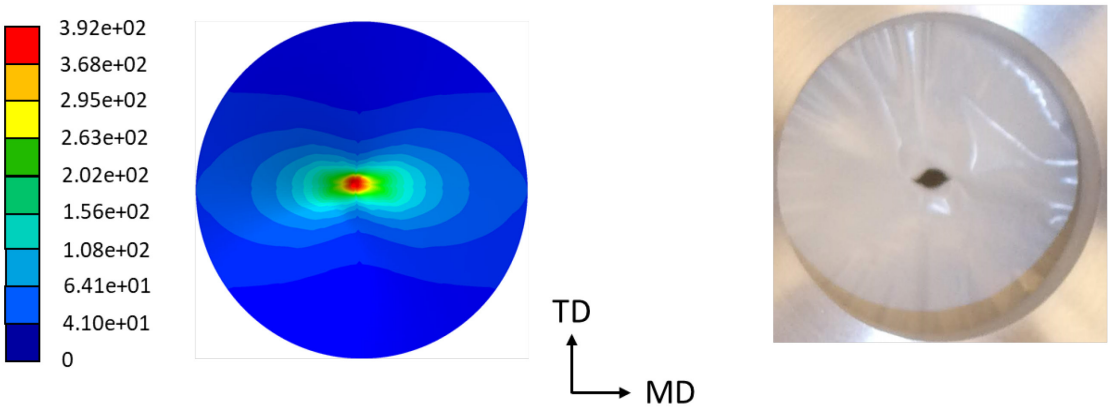

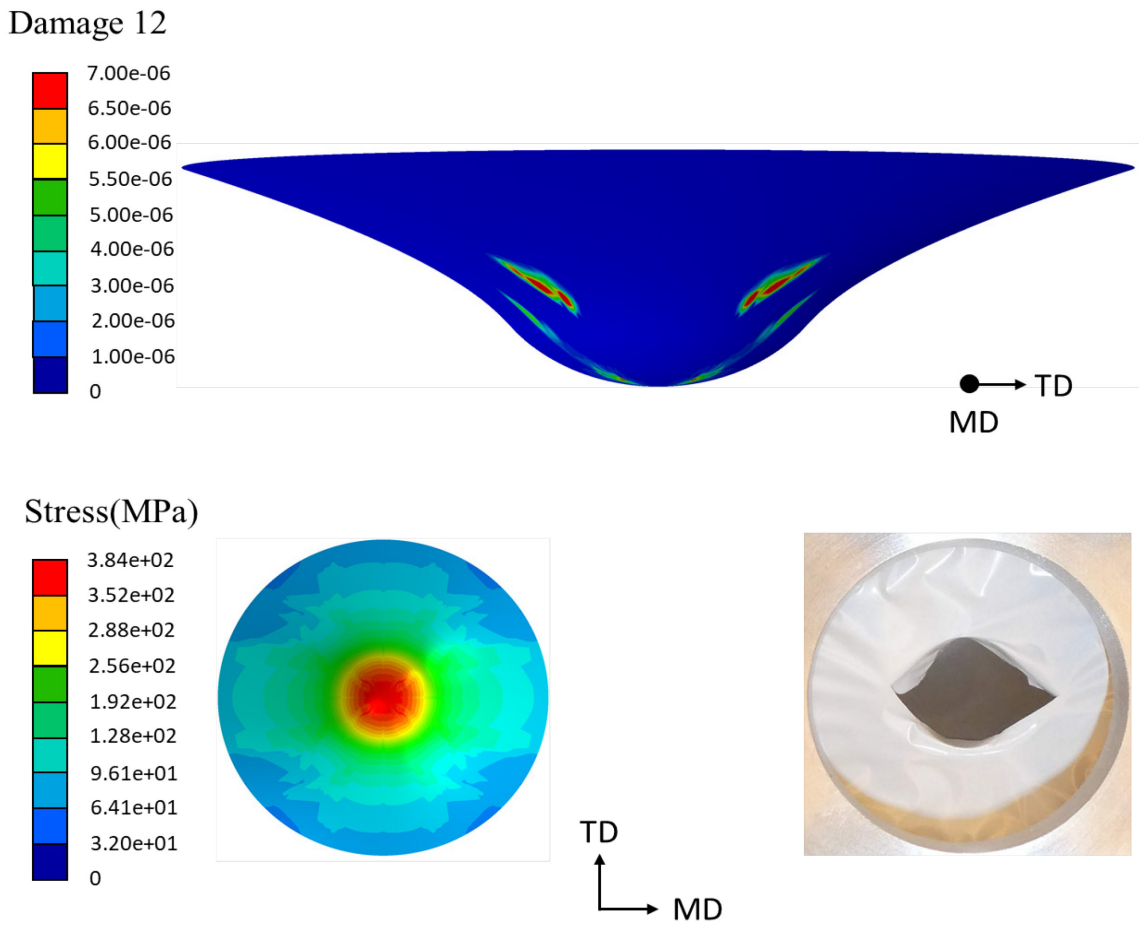

Figure 2.12: Damage and stress distribution for the PE separator at fracture for a punch diameter of (top) 3.2 mm and (bottom) 12.7 mm.

Figures 2.13 shows for both punch diameters the deformed configuration of the trilayer separator just before reaching fracture (the top figures are for the 3.2 mm punch diameter and the bottom figures are for the 12.7 mm diameter). Similarly, on the left side, a side view of the separator shows the damage distribution. On the right side, a top view of the separator shows the stress distribution. Zhang et al. (2016a) and Zhang et al. (2016b) described thoroughly the fracture developed by the trilayer separator and reported that for small punch diameters, the failure was local and round shaped while for large punch heads a slit was along MD. Figure 2.13 highlights the capability of the model to predict the fracture behavior of trilayer separators subjected to punch

loading. Indeed, for the 3.2 mm punch diameter the predicted damage and the stresses are localized in the middle of the sample below the punch. For the 12.7 mm punch diameter, the stress is distributed along MD, which is in correlation with the experimentally reported MD-oriented slit.

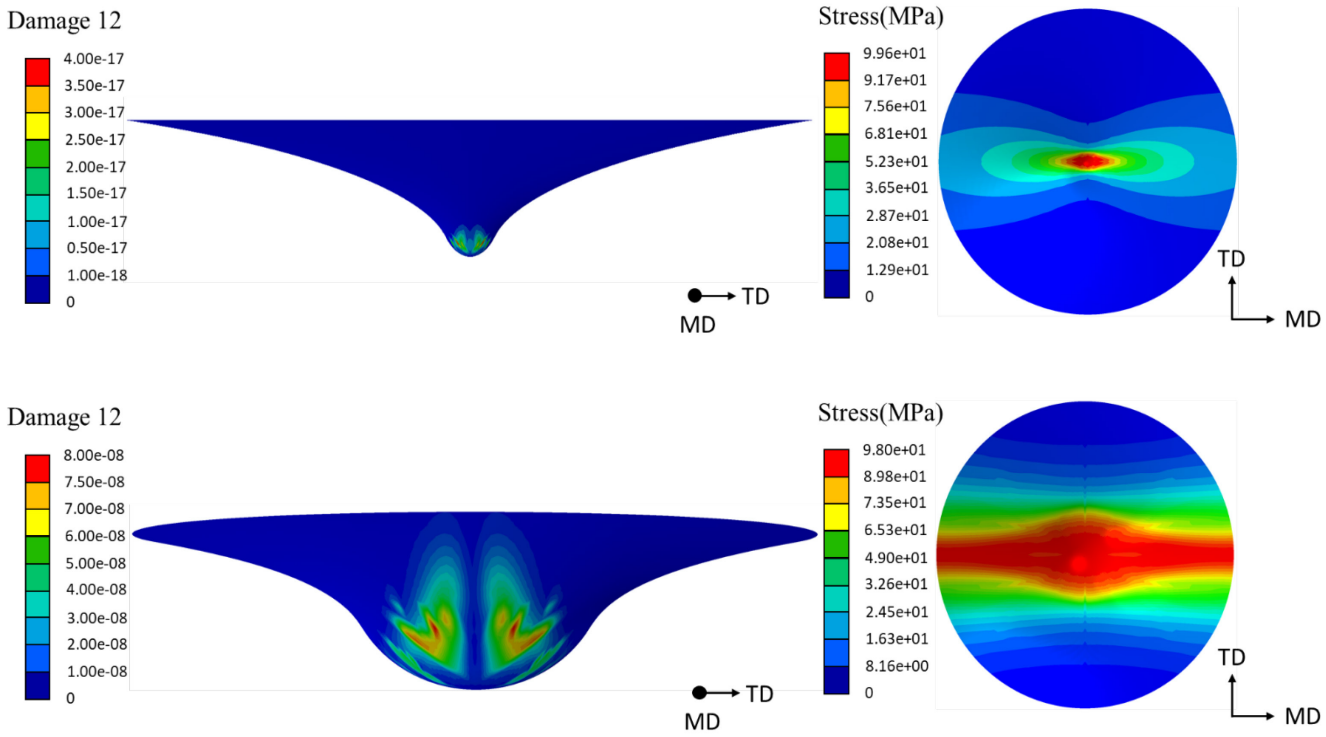

Figure 2.13: Damage (left) and stress distribution (right) for the trilayer separator at fracture for a punch diameter of (top) 3.175 mm and (bottom) 12.7 mm.

2.5 Conclusion

In this chapter, the mechanical and anisotropic behavior of a single-layer polyethylene battery separator was investigated under uniaxial tension and punch tests. The mechanical behavior of the polyethylene battery separator is highly anisotropic with elasticity, yielding, hardening and fracture properties exhibiting high dependency on loading directions. Furthermore, battery separators exhibit cyclic dissipative behavior during battery charge/discharge conditions. A unique constitutive model was proposed that for the first time combines between the anisotropic

continuum damage theory and the non-Gaussian network constitutive model that was carefully reformulated using a back-stress approach to account for the viscohyperelastic behavior. Furthermore, the mathematical framework of the constitutive model presents a unique formulation in which the hill anisotropic tensor and the damage tensor are written as fourth-order to present a practical approach for combining the different theories. The fourth-order damage effect tensor is an operator that maps the damaged material configuration to an undamaged fictitious configuration, it allows computing the damage evolution and the failure prediction. Furthermore, in contrast with existing coupled mechanical and damage models where the damage tensor is expressed in the principal direction of the damage (which is not always aligned with the principal direction of deformation), in this work the damage tensor was defined in the global coordinate system. The anisotropic behavior of the polyethylene battery separator was accounted for using directional coefficients of hardening, Hill symmetric tensor and a fourth-order damage effect tensor.

A robust implicit integration scheme was developed, and the model was implemented as a user-defined material subroutine (UMAT) in commercial finite-element software, which allows boundary-value problem solution. The capability of the proposed model to predict the anisotropic mechanical behavior up to fracture for two different types of battery separators was assessed using the experiments generated on the polyethylene single layer battery separator (Wet-processed), and the experiments reported in the literature on PP/PE/PP trilayer (Dry-processed). The model parameters for each type of separator were identified using tensile experiments along different material directions. The predictive capability of the model was assessed using the identified parameters to predict the mechanical response of the separators under punch experiments. The model results showed a good agreement with the experimental data. Moreover, the model was able

to predict the failure of the separators under different loading conditions. Numerically, the damage tensor was computed on each element; however, failure is induced by the node presenting the highest damage value. Although fracture propagation is not studied, the crack direction is estimated to be along the material direction with the highest damage values. Finally, the model-predicted failure correlated with the rapid increase in the maximum damage.

Separators are microporous films sandwiched between the anode and cathode to prevent physical contact and allow the exchange of ions between the two electrodes. Degradation in the separator occurs under battery charge and discharge cycles, affecting its mechanical properties. Failure in this component can cause internal shorting of the battery or thermal runaway. Hence, an accurate characterization and modeling of the separator's mechanical behavior and induced degradation under different charge and discharge cycles is essential for optimal design and life-cycle operation of commercial lithium-ion batteries. Furthermore, a numerical framework accounting for microstructural and network properties such as porosity, crystallinity, chains density, and chains average length is essential for predicting the mechanical behavior degradation induced by battery charge-discharge cycling. Although the objective of this study does not encompass studying the aging of battery separators, the proposed physical-based model was developed to facilitate such investigation in the future. Indeed, providing engineers with such valuable information will help in designing more efficient batteries. Hence, the authors will be working in the near future on validating the capability of the proposed model to predict the effects of aging in the separators under charge and discharge cycles.

Chapter 3 Effect of Battery Fast Cyclic Charging on the Aging of Lithium-Ion Battery Separator

Lithium-ion batteries (LIB) are widely used in electronics devices and are the dominantly used technology in electrical vehicles. During charge and discharge, LIB undergo stresses due to the electrochemical reaction at the electrodes, causing thermal and mechanical stresses to arise in the battery components and specifically the separator. The separator plays a crucial role in the LIB preventing electrode contact and facilitating ionic transfer. In this chapter, the separator aging mechanisms due to charge and discharge have been investigated under fast charging conditions. Six LIB in total were subjected to 4C charging conditions. Each pair of LIB were cycled to 400, 800, and 1600 cycles. The physical and chemical microstructural changes in the cycled separators were investigated using a series of tests such as scanning electron micrographs, X-ray photoelectron spectroscopy and Fourier Transform Infrared Spectroscopy. Additionally, the mechanical behavior of the as-received and aged separators was also investigated using uniaxial tensile tests and biaxial punch tests. No chemical degradation was observed in the separator even at 1600 cycles. The main mechanism of aging in the battery separator was due to creep-fatigue caused by the battery fast charge and discharge cycling at high operational temperature.

3.1 Introduction

The growing need for electrical vehicles (EVs) that is projected to rise 17-fold by 2030, increased the demand for energy storage using high performant electrochemical energy sources.

Lithium-ion batteries emerged as preferred energy source for EVs driven by their excellent life cycle, lighter weight, affordability, high energy density (100-250 Wh/kg) and high power per mass battery unit (800-2000W/kg) (Iclodean et al., 2017; Alaoui, 2013). A lithium-ion battery comprises a positive electrode (Cathode), a negative electrode (Anode), a separator, and current collectors immersed in an organic solvent of lithium salt mixture as the electrolyte (Lukic et al., 2008). For most lithium-ion batteries carbon active anode is utilized bonded to a copper current-collector to create an electron flow route (silicon, lithium titanate, or tin dioxide anodes can be also found). Active cathodes are made of lithiated transition metal oxides adhered to an aluminum current-collector to create an active path of electrons flow. The electrolyte is composed of a mixture of organic solvents (carbonates like ethylene, propylene, dimethyl, diethyl carbonates) into which lithium hexafluorophosphate (LiPF6) is dissolved (Huang, 2011). The electrolyte allows the movement of lithium ions (Li+) between the anode and cathode. During battery discharging, lithium ions are transferred from the anode to cathode and in the opposite route during charging. Finally, a porous separator facilitates the transport of ionic charge carriers in the cell and prevents the physical contact between the anode and cathode (Barré et al., 2013). While lithium-ion batteries present numerous advantages, the capacity loss under fast charging conditions poses big challenges (Alaoui, 2013; Gerssen-Gondelach and Faaij, 2012; Lu et al., 2013; Lukic et al., 2008). The purpose of this work is to guide future improvement of lithium-ion batteries manufacturing by understanding the effect of cyclic fast charging on the mechanical and physico-chemical properties of the separator.

An integral part of the liquid electrolyte lithium-ion battery is the separator which is a porous membrane positioned between the positive and negative electrodes. Although the separator does not contribute to any of the electrochemical reactions occurring in the battery, it plays a

critical role in enhancing the safety of batteries by impeding physical contact of the electrodes, enhancing free ionic transfer, and isolating electronic flow (Arora and Zhang, 2004). Commercial separators with different compositions and structures are being used such as inorganic composite membranes, non-woven fabric mats, and microporous polymer membrane separators (Arora and Zhang, 2004; Huang, 2011; Shi et al., 2011). Microporous polymer membrane separators are thin films characterized by a high thermal shutdown. Non-woven mat separators are categorized as high porosity and low cost. The composite membrane separators possess tremendous wettability and phenomenal thermal stability (Zhang, 2007). Polyolefin separators have been extensively used in Li-ion batteries used in EVs (Arora and Zhang, 2004; Lee et al., 2014). The mechanical properties of polyolefin separators vary depending on the material and fabrication process. It was reported that the separator mechanical properties, thickness and porosity characteristics strongly influence the battery performance, safety and cyclic charge reliability (Lee et al., 2014, 2016). In lithium-ion batteries mostly semi-crystalline polymer separators are used; Polyethylene (PE), Polypropylene (PP), PE/PP composite such as triple layered PP/PE/PP, polyesters such as polyethylene terephthalate etc. (Xing, 2018). Two main processes are used for fabricating microporous polymer membranes: (1) dry process (Johnson and Wilkes, 2002b, 2002a, 2001) and (2) wet process (Foley and Celanese, 1993; Ihm et al., 2002). While wet processed separators are characterized by a quasi in plane isotropic properties, dry processed separators exhibit a high anisotropy (Arora and Zhang, 2004).

The separator main purpose is preventing direct contact of the electrodes by maintaining stable battery operation conditions at higher temperatures (Vetter et al., 2005). The battery temperature can increase significantly when subjected to fast charging conditions (Goutam et al., 2017; Xu et al., 2015; Ye et al., 2012). Furthermore, some battery separators are designed with

shutdown function to effectively protect against thermal accidents. Indeed, those separators will prevent the cell from catching fire or exploding by melting at a temperature below the thermal runaway; hence, closing the ionic conduction pathway (Huang, 2011). Under normal operating conditions (charge and discharge), the battery components are subjected to electrochemical, thermal, and mechanical aging resulting into battery cells' capacity loss and the degradation of battery separators (Lin et al., 2015). Indeed, a drop in the separators' stiffness and ductility has been reported at high number of charge and discharge cycles (Zhang et al., 2017a). During charge-discharge cycling, separators undergo oxidation on the anode-facing side and reduction on the cathode-facing side. Separators with low oxidation resistance can lead to poor performance at high-temperatures and long-term charge-discharge cycling (Arora & Zhang, 2004). Chemical reaction products can potentially block the separators' pores, leading to increased cell resistance and impedance (Zhang et al., 2017a). Moreover, Shi et al., (2011) also reported that lithium diffusion, electrode induced deformation, and differential thermal expansion between the cell constituents subject the separator to mechanical stresses. Indeed, lithium-ion intercalation causes electrodes expansion and consequently the squeezing of the soft separator (Gor et al., 2014).

In the last decade, several studies investigated the microstructural properties and mechanical behavior evolution of separators with charge discharge cycling. Peabody & Arnold, (2011) studied the role of mechanically induced creep, under normal operation and storage conditions, on accelerating lithium-ion battery loss of capacity and power. SEM analysis of the separators subjected to external compressive stresses (applied on the battery pouch cell) showed separator pore closure. The porosity in the separator decreased with increasing external compressive stresses. Moreover, a noticeable decrease in pores density was observed associated with closing of small pores. The noticeable decrease in the number of pores accompanied with the

shrinking of larger pores reduce ion transfer and as consequence, internal resistance and capacity fade increase. Martinez-Cisneros et al., (2016) investigated the effect of thermal aging on the morphology and thermomechanical behavior of single layer and trilayered polyolefin separators. The comparison between SEM images of pristine and thermally aged separators revealed that wet processed separators had negligible morphology change while pores density decreases in dry processed separators. Xing, (2018) studied the stability of different types of separators against Li metal anode and recorded Fourier-transform infrared (FTIR) spectra for pristine and charge-discharge cycled separators. The analysis of FTIR spectra revealed the presence of an acyl C-O stretching absorption peak associated to the decomposition of the cyclic solvent of ethylene carbonate (EC). Gor et al., (2014) assessed the role of intercalation of lithium ions on battery performance. For that purpose, the performance of separators under compression was studied. It was shown that due to fluid flowing in the pores, the response of separators under compressive loading is influenced by the polymer skeleton viscoelastic and poroelastic behaviors. Zhang et al., (2016b) investigated battery separators deformation and failure mechanisms under mechanical loading. Two distinct failure mechanisms were identified under biaxial loading, and were used to potentially explain the difference in short circuits characteristics. The first failure mode featured a large diagonal slit along the machine direction, and the second mode showed and a zig-zag surface along the transverse direction. The results suggested that some cells undergo thermal runaways under predictable force and displacement levels (First Mode) while others can handle much larger deformations without apparent failure (Second Mode). Similarly, Kalnaus et al., (2018) investigated lithium-ion battery polymer dry-stretched separators' deformation and failure mechanisms under biaxial loading. It was reported that dry-processed polymer separators exhibited anisotropic behavior and fractured along the machine direction in either a single crack or two

symmetrical cracks. Sheidaei et al., (2011) studied the mechanical behavior of lithium-ion battery separators in electrolyte solutions and noticed that the separators were relatively softer under wet testing conditions compared to dry testing. Xu et al., (2016) conducted a series of tensile tests at different strain rate and directions (machine, transversal and diagonal directions) and environmental conditions (Wet vs dry). It was reported that strain rate has a strong effect on the mechanical properties. The flow stress and the failure stress both increases with increasing strain rate while the failure strain decreases with the strain rate. Finally, Plaimer et al., (2016) performed tensile tests, puncture tests and impedance spectroscopy on 10 different types of separators commonly used in lithium-ion batteries (Microporous polymer separators, nonwoven separators and composite separators) in order to compare the trade-off between mechanical and electrochemical properties. The main conclusion of their work was that monolayer and multilayered separators have better mechanical strength and ionic resistance compared to nonwoven and composite separators.

Fast charging of lithium-ion battery is an essential solution for wide adoption of EV but it is often accompanied with significant loss of capacity affecting the battery life performance. While the effect of fast charging on the performance of the cathode and anode was widely studied, it's effect on the performance of the separator still need to be uncovered. Furthermore, although separators were extensively studied and characterized under regular lithium-ion battery operation, there has not been a fully coupled physico-chemical and mechanical characterization of the separators subjected to fast charging conditions. Thus, the purpose of this work is to guide future improvement of lithium-ion batteries manufacturing by understanding the effect of cyclic fast charging on the mechanical and physico-chemical properties of the separator. Indeed, under fast charging condition the separator is subjected to accelerated electrochemical reactions and more

severe thermal and mechanical operation conditions that accelerate its aging. Accordingly, understand the aging mechanisms of the battery separator subjected to cyclic fast charging can help improve battery design to increase life efficiency and safety. The chapter is organized as follows: In section 3.2, the experimental methodology used for characterizing the cyclic fast charging behavior of lithium-ion battery separator is described. The results of the physico-chemical and mechanical properties characterization are presented in section 3.3. In section 3.4, the experimental results are discussed and the separator aging mechanisms under cyclic fast charging conditions are described. Finally, in section 3.5, concluding remarks are provided.

3.2 Experimental Methodology

This section describes the lithium-ion battery cell fabrication method and the cyclic fast charging conditions used in this study. Additionally, the battery separator experimental characterization method is presented.

3.2.1 Lithium-Ion Battery Cells Fabrication and Cyclic Charging Condition

The lithium-ion battery pouch cells were fabricated using double-sided mesophase graphite (SMG) anode, double-sided $LiNi_{0.6}Co_{0.2}Mn_{0.2}O_2$ (NMC 622) cathode, 1 M $LiPF_6$ in ethylene carbonate (EC): ethyl methyl carbonate (EMC) (3:7 by volume) electrolyte, and a wet processed polyethylene single layer separator. The dimensions of the pouch cell were 74 x 110 x 4 mm and the nominal capacity was 3.5 Ah. All the battery pouch cells used in our study were fabricated at the same time. Our collaborators at an original equipment manufacturer (OEM) assembled the lithium-ion battery pouch cells.

The single layer porous polyethylene (PE) separator was fabricated by co-extrusion blowing process to a 12 μm thickness. The semi-crystalline PE separator has a crystal content

range between 60% and 80% and porosity 43%. The PE separator physical and mechanical properties provided by the manufacturer are shown in Chapter 2 Table 2.1.

In total six battery pouch cells were tested in this study. As aforementioned, the purpose of this study is to investigate the effect of cyclic fast charging on the degradation of the battery separator. Consequently, the six lithium-ion battery pouch cells were subjected to cyclic fast charging conditions at 4C (14 Amperes) up to 400, 800, and 1600 cycles. To assess the repeatability of the results each cyclic fast charging conditions was applied on two different pouch cells.

The following paragraph describes the conditions applied on battery pouch cells for conducting the cyclic fast charging. Appendix C contains all the fixture dimensions. In the first stage, all the battery pouch cells were charged to 3.6 volts. Then, the pouch cells were sandwiched between two plates, using an in-house designed fixture. The fixture plates were tightened with a torque of 1.0 N.m. The purpose of the setup was to mimic the loading conditions in battery packs. In the second stage, the batteries were charged to 4.2 volts at 4C and discharged to 3.0 volts at 0.5C. The charging process consisted of two steps: charging of the battery at a constant current (14 Amperes) until reaching a voltage of 4.2 volts, and then holding the cell voltage at 4.2 volts until the current drops to 5% (0.7 Ampere) of its initial value. For the discharge process, it also consisted of two steps: discharging the battery at a constant current until reaching 3.0 volts, then holding the cell voltage at 3.0 volts until the current drops to 5% (0.0875 A) of its initial value. The charge-discharge process ran continuously without a rest time. The experiment was carried out at an ambient temperature of 20 degrees Celsius.

Once the cyclic fast charging process was completed after each specific number of cycles, the batteries were removed from the fixture, tested to verify that they are fully discharged, and

then carefully disassembled. Furthermore, the cycled separators were extracted from the batteries for further analysis.

3.2.2 Characterization Methods

Pristine and cycled separator film coupons were examined in scanning electron microscopy (SEM). The purpose was to detect possible microstructural changes induced by the cyclic fast charging process. Each separator film test coupon was gold coated and observed using Tescan MIRA3 FEG SEM with 5kV accelerating voltage. SEM micrographs of the pristine separator were analyzed to assess pores size and orientation and accordingly constitute a comparison reference to assess damage development in cycled separators. SEM analysis was also conducted on cycled separators at 800 and 1600 cycles. Two different SEM observations were performed for each analyzed separator: at the surface (plane) and through the thickness (Cross-section) (Figure 3.1).

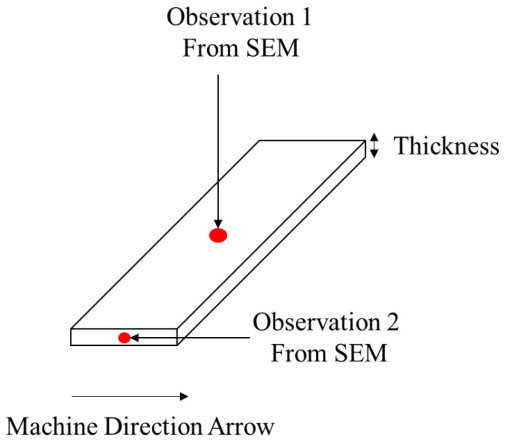

Figure 3.1: Specimen surfaces examined by SEM.

Xray photoelectron spectroscopy (XPS) surface analysis was conducted using Kratos Axis Ultra XPS. The kinetic energy spectra of photoelectrons ejected from the surface of pristine separator and 1600 cycled separator are analyzed. Furthermore, the XPS elemental composition

analyses of three surfaces are done: on the pristine separator, on the anode side of the 1600 cycled separator, and on the cathode side of the 1600 cycled separator.

A Fourier Transform Infrared Spectroscopy (FTIR) was used to assess the effect of cyclic fast charging on the separator by measuring the presence of different organic functional groups. The infrared (IR) spectra of pristine and 1600 cycled separators were recorded with a micro-ATR (diamond cell) sampling within 4000 to 400 cm^{-1} range averaged from 32 scans obtained with at least 4 cm^{-1} resolution. The IR spectra of three different samples were analyzed: pristine separator, anode side of the 1600 cycled separator, and cathode side of the 1600 cycled separator.

3.2.3 Mechanical Testing

Uniaxial tensile tests were conducted on the pristine and cycled separators. The tensile specimens were strip-shaped and cut out from the separator films using a razor. The specimens' major axis was aligned in either the Machine direction (MD), or the transversal direction (TD) (Figure 3.2). These specimens were prepared according to ASTM standard D882. The strip geometry is rectangular with 100 mm in length and 25 mm in width ad during testing the gage length was set to 50 mm. A width of 25 mm was chosen to decrease the standard deviation error. The uniaxial tensile tests were conducted using a TestResource Model TR 100Q225 universal test machine equipped with a 220 N load cell. Rubber jaws were used to clamp the specimen from both sides to prevent slippage. The tensile tests were conducted at three different strain rates: 0.16/s, 0.016/s, and 0.0016/s. Each test scenario was repeated three times and the average load-displacement curves were computed. The tensile tests were achieved on pristine separator and 400, 800, and 1600 cycled separators.

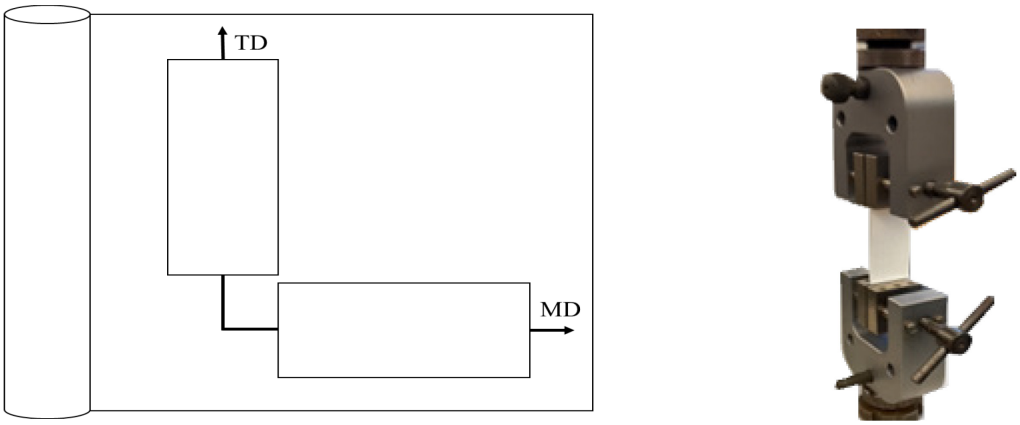

Figure 3.2: (Left) Tensile specimens direction with respect to the separator roll, (Right) uniaxial tensile test setup.

The evaluation of thin films fracture behavior can be challenging with uniaxial tensile test. Indeed, cutting out tensile specimens with consistent edge quality is challenging and a stochasticity in the fracture strain is often observed. Biaxial loading condition applied using a punch test can be used to reduce the uncertainty associated with inconsistent edge quality. Furthermore, it represents loading conditions that the separator may undergo during cyclic charging. Chen et al., (2014) reported that under cyclic charging, separators rolled around the edges of the anode and cathode are subjected biaxial loading. The same TestResource Model TR 100Q225 universal test machine was used for punch testing. The setup consisted of three components (Figure 3.3): the die, the clamping plate, and the punch head. Square specimens with 55 mm side were cut using a razor (Figure 3.3). The specimen was tightly gripped between two rubber rings. The rubber rings placed in grooves machined into the die and the clamping plate were used to eliminate slippage. Four 3D-printed hemispherical punch heads with different punch diameters (3.2 mm, 6.4 mm, 12.7 mm, and 25.4 mm) were used in this study (See Appendix C). The punch heads were gripped by two steel jaws. The central axis of the die was carefully aligned with the universal test machine axis before testing. A crosshead speed of 12 mm/min was used for all tests. The cycled separators were

punched from two sides: the anode side which (the side in contact with the anode electrode), and the cathode side (the side in contact with the cathode electrode). Indeed, as aforementioned, during cyclic charging, different chemical reactions take place at the anode-facing side and the cathode-facing side of the separators. As results, the two sides of the separator will be different chemically (details are presented in section 3.1). The punch testing was conducted on the pristine separator and the 400, 800, and 1600 cycled separators. Two repetitions were done for each test scenario to ensure the reliability of the experimental data.

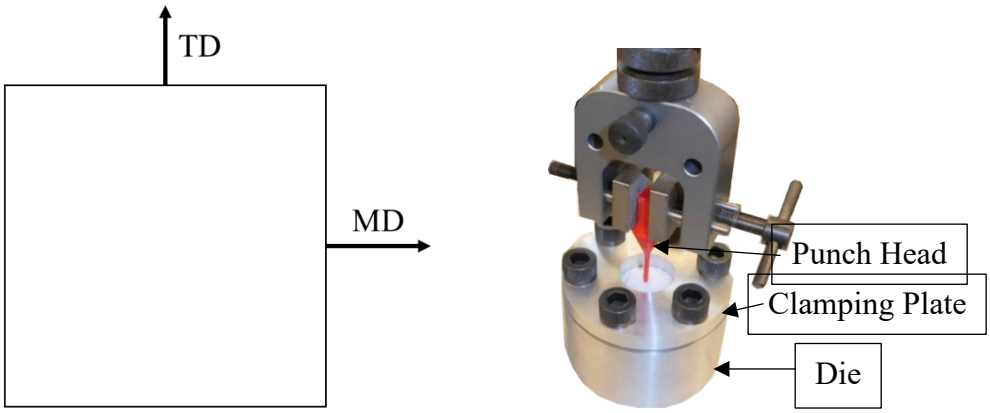

Figure 3.3: (Left) punch specimen geometry, (Right) punch Test Setup.

3.3 Experimental Results

3.3.1 Physico-Chemical Characterization

Once the cyclic fast charging is completed, the battery pouch cells were fully discharged and carefully disassembled in a fume hood. The battery pouch edges were cut to open it up and reveal its components. The components were then removed, the separator was released from the anode and the cathode and allowed to dry. The 400, 800, and 1600 cycled separators anode side after extraction are shown in Figure 3.4. The separators showed an increase in the deposit density with increasing number of charging cycles. The 400 cycled separators showed brownish scattered

spots while the 800 cycled separator was consistently coated, with some scattered uncoated spots. The deposits density is clearly the highest for the 1600 cycled separator, with the deposit covering completely the surface of the separator in contact with the anode electrode. As for the cathode side, the separators did not show any deposits for all three cyclic charging conditions.

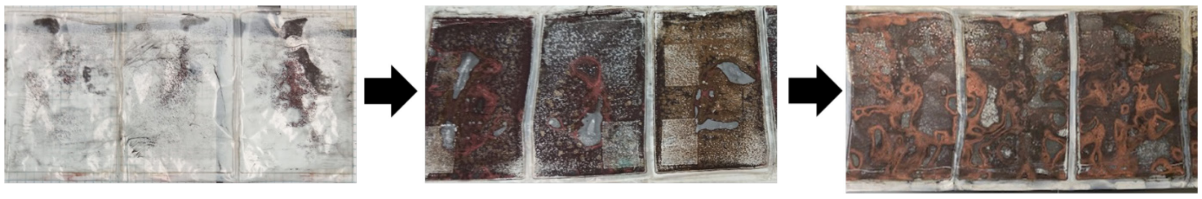

(400 Cycles) (800 Cycles) (1600 Cycles)

Figure 3.4: Cycled separators after extraction showing deposits on the anode side.

The capacity retention vs number of cycles at 4C cyclic charging condition is shown in Table 3.1. The battery lost 27.1% of its capacity after the first 100 charging cycles. Lu et al., (2013) reported similar observations and attributed the capacity loss to the fast-charging conditions which causes high operational temperature affecting the batteries' energetic performance, and life cycle. The sharp decrease is followed by a weak almost linear decrease between 100 and 1600 charging cycles. In what follows, we will continue investigating how the separator physical and chemical properties alteration influence the battery capacity loss.

Table 3.1: Capacity retention per number of charging cycles.

Number of Cycles	Capacity Retention (%)
100	72.90
200	71.75
400	71.71
800	69.09
1000	68.75
1600	68.21

The change in microstructural featured between pristine and 800, 1600 cycled separators were examined with SEM. The cycled separators were examined from both the anode and cathode sides. In all the presented SEM micrographs (surface and cross-section), the machine direction is parallel with the scale bar. The microstructure of the pristine separator exhibits an entangled fibrous structure with randomly oriented equiaxed pores as shown in Figure 3.5 (surface view), with pore size less than 0.5 μm. The morphology of the pristine separator shows that the pores are trapped between three or more nanofibers. Furthermore, a higher fibril alignment is observed along the machine direction compared to the transversal direction. The SEM micrograph of the cross-section shows that the PE separator exhibit a fibrous structure along the thickness. The fibers and the pores are mainly aligned along the machine direction.

(a) Surface view (b) Cross-section

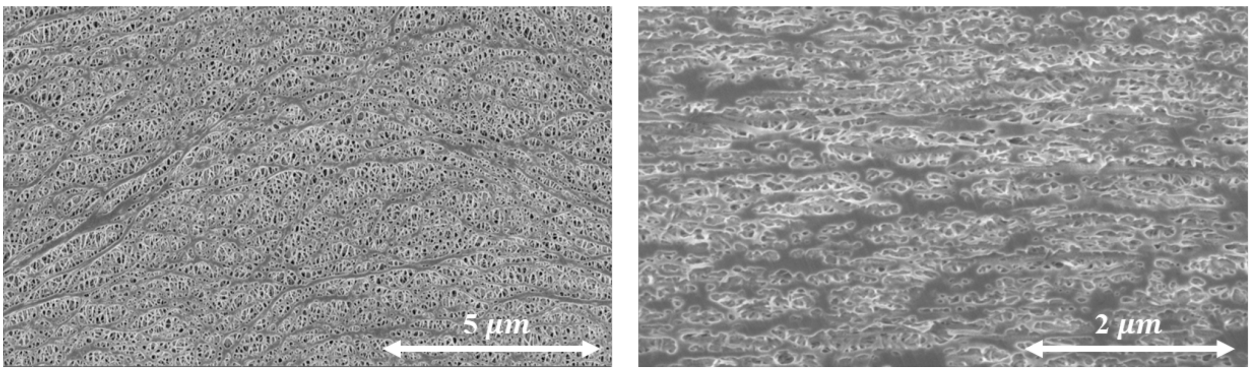

Figure 3.5: SEM micrographs of pristine separator from (a) surface view, (b) cross-section.

A comparison between the SEM micrographs of 800 and 1600 cycled separators is shown in Figure 3.6. The SEM micrographs of the separator anode side showed that the PE film is completely coated and different coating densities are noticed for both the 800 and 1600 cycled separators. In contrast, the SEM micrographs of the separator cathode side did not show that the PE film is coated. The separator cathode side showed scattered small deposits (potentially chemical reaction products) for both the 800 and 1600 cycled separators. The 1600 cycled separator showed a higher density of larger deposits compared to the 800 cycled separator.

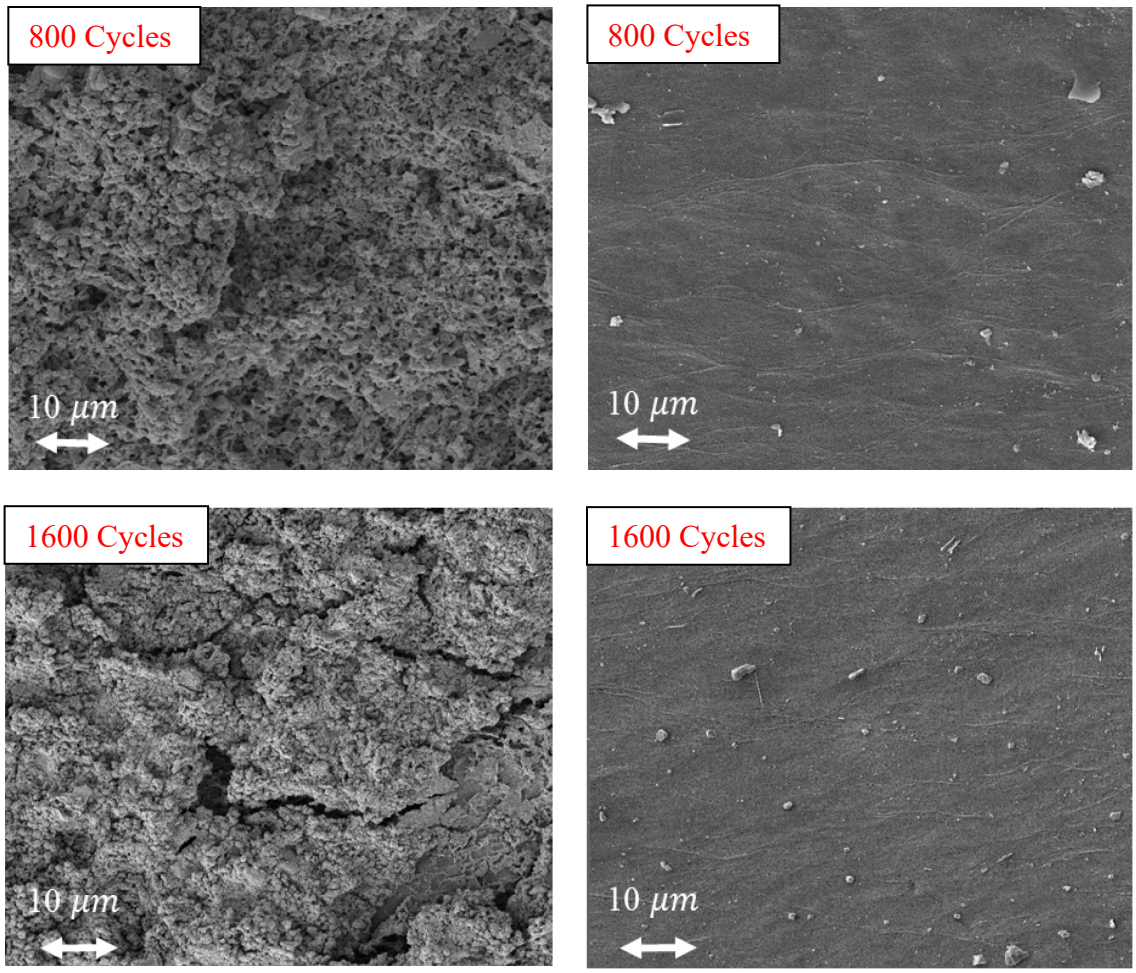

Figure 3.6: Cycled separators at 800 and 1600 cycles, (Left) Anode Side (Right) Cathode Side.

The microstructure of the 1600 cycled separator was also closely investigated at higher magnification from the cathode side (Figure 3.7). In addition to the dispersed deposits, the 1600 cycled separator morphology has the same fibrous structure observed in the pristine separator. Moreover, localized fibers fracture was observed in several locations along the MD-TD plane. The fibers localized fracture occurred mainly in the thinner fibers potentially attributed to is the thermal and mechanical stresses the separator is subjected to during operations.

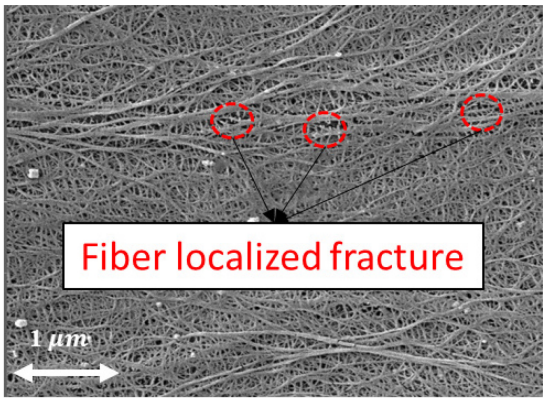

Figure 3.7: Higher magnification SEM micrographs of the 1600 Cycled separators from the cathode side.

For a thorough investigation of the separator microstructure evolution, Figure 3.8 shows the cross-sectional SEM micrographs of the 800 and 1600 cycled separators. Separator pore closure can be clearly observed. Compared to the pristine separator microstructure, a clear reduction in pores length and size is observed for the 800 cycled separator. The through thickness compressive forces and compressive creep during the battery operation can potentially be related to pore closure (Peabody & Arnold, 2011). Furthermore, the SEM micrographs of the 1600 cycled separator shows in addition to pore closure the nucleation of micro-voids, crack growth and coalescence. The observed micro-cracks were aligned along the thickness direction.

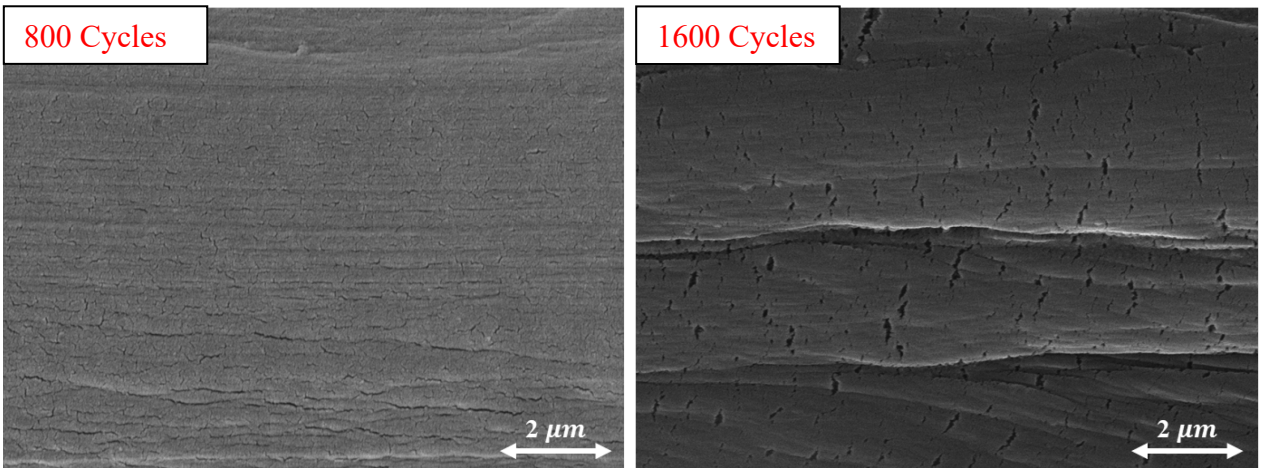

Figure 3.8: Cross-section SEM image for the 800 cycles and 1600 cycled separators.

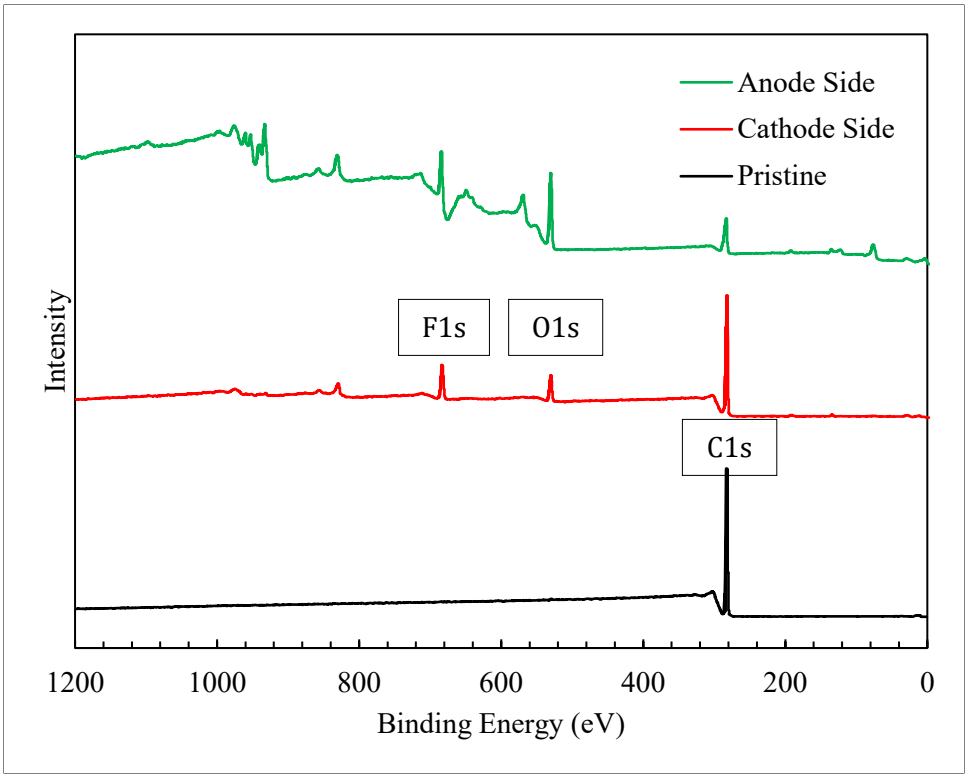

Figure 3.9: XPS spectra of pristine, 1600 cycled anode side, and 1600 cycled cathode side separators.

The XPS spectra of pristine, 1600 cycled anode side and 1600 cycled cathode side separators are shown in Figure 3.9. One characteristic peak corresponding to C 1s at 285 eV is observed for the three characterized surfaces. This peak is associated to the C-C bond of the PE polymer. The lowest intensity is measured at the anode side surface as a result of the deposited layer. Two other characteristic peaks at 530 and 682 eV corresponding to O 1s and F 1s respectively, are observed for both surfaces of the 1600 cycled separator. However, the anode side peaks are stronger than the cathode side. Small traces of P and Cu can also be observed for both surfaces of the 1600 cycled separator. While P can be a deposit from the electrolyte, the Cu might be a deposit from the current collector. Stronger Cu and P peaks can be observed at the anode side of the 1600 cycled separator.

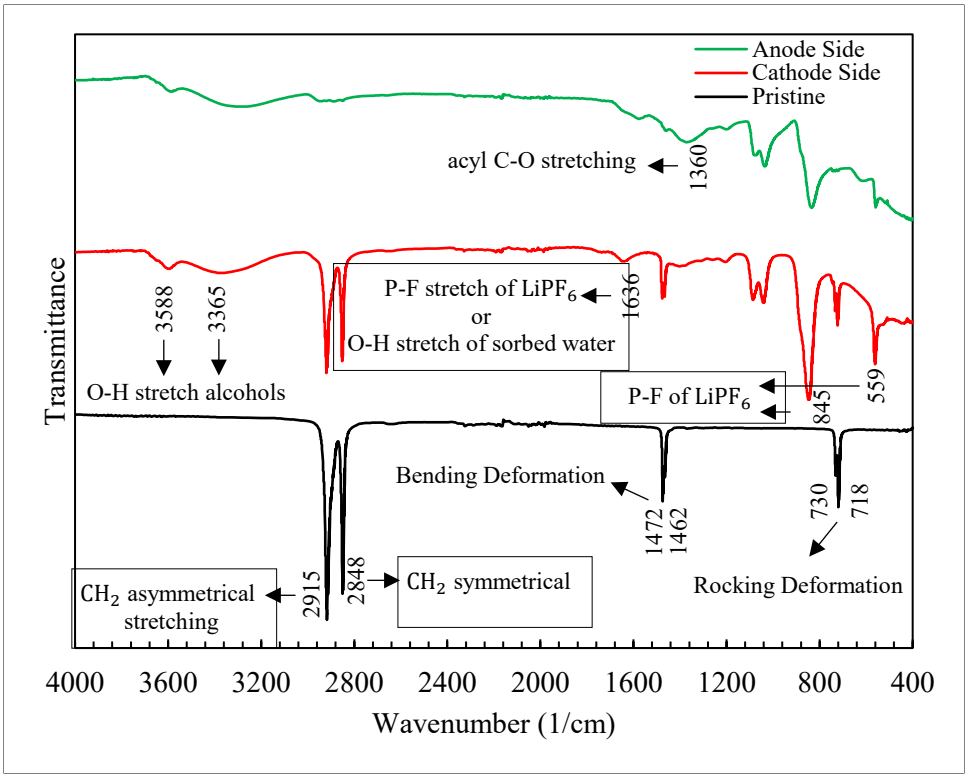

Figure 3.10: FTIR results for the as-received, anode side, and cathode side.

The IR spectra of pristine, 1600 cycled anode side and 1600 cycled cathode side separators are shown in Figure 3.10. Absorption bands are detected better on the pristine and the 1600 cycled cathode side separators. The small apparent difference in the position of several IR bands on the 1600 cycled anode side separator compared to the cathode side is only due to the poorer detection of these bands as a result of the deposited layer. Indeed, the IR bands of the PE are practically not detected on the 1600 cycled anode side separator. Indeed, the bands detected are mainly those of the electrolyte and its degradation products. For the as-received separator, typical HDPE separator characteristics bands appeared at 2915 and 2848 cm^{-1} corresponding to CH_2 asymmetric stretching and symmetric stretching vibrations respectively. Two peaks can be observed at 1472 cm^{-1} and 1462 cm^{-1} corresponding to CH_2 bending due to scissors vibration mode, this behavior is observed in HDPE mostly where the CH_2 chains can orient parallel to each other forming areas

of long ordered range. Two final peaks can be seen at 718 and 730 cm^{-1} corresponding to CH_2 bending due to rocking vibration mode (Jin et al., 2017; K. J. Kim et al., 2014). The 1600 cycled cathode side separator, both the bands of the polymer and electrolyte can clearly be observed. The first conclusion that can be drawn from these results is that the electrolyte was absorbed throughout the thickness of the separator. However, the absorption of the electrolyte is presumably selective because the most intense IR absorption bands of ethylene and vinylene carbonates (i.e. C=O stretches, typically ranged between 1760 and 1860 cm-1), and ethyl methyl carbonate (i.e. O-C-O stretch, at about 1270 cm-1) are not detected. In contrast, several IR absorption bands of lithium hexafluorophosphate (LiPF6) can be observed, in particular at 559 and 1636 cm-1 [Proc. of conference day "Lithium accumulators", 1996; (Kock et al., 2012)]. Interestingly, the IR absorption band of the P-F bond stretch is not detected at its usual position around 830 cm-1 (Aurbach et al., 1994); but at a higher wavenumber, more precisely around 845 cm-1. According to Aurbach et al. (1994), this shift in wave number may be due to the degradation of LiPF6. The second conclusion that can be made is that the IR spectra do not provide proof of obvious chemical degradation taking place in the separator as a result of chain scission. Two bands can be observed at 3588 cm^{-1} and 3364 cm^{-1} which corresponds to O-H bond stretching in free bond and intermolecular bonds respectively. Since traces of fluorine were observed during the XPS analysis, the peak observed at 1360 cm^{-1} was first thought to be CF_2 stretch which generally appears between 1300 to 1000 cm^{-1}, however C-F bonds also have a bending vibration at around 650 cm^{-1} which is not observed in the spectrum. The 1360 cm^{-1} peak corresponds to the acyl C-O stretching which might be due to the decomposition of the cyclic solve of EC (Xing, 2018).

3.3.2 Mechanical Characterization

3.3.2.1 Tensile Testing

The engineering stress-strain curves for the pristine and the cycled separators are shown in Figure 3.11. The engineering stress is defined as the ratio between the load and the original cross-sectional area A of the tensile sample. The engineering strain is defined as the ratio between the elongation Δl of the tensile sample and the original gauge length l_0. The tensile tests were conducted along the machine direction and the transversal direction of the separator using three strain rates 0.0016/s, 0.016/s, and 0.16/s. The plotted engineering stress-strain data are averaged for each tensile test condition over the three times repeated tests results. The repetition with the lowest fracture strain was used as the cut-off in the average data. The engineering stress-strain behavior of the porous PE film displays three stages of deformation: (1) a linear elastic response at lower strains followed by (2) a steady rollover to the plastic region followed by (3) a slower increase of the stress. An anisotropic behavior is exhibited by the porous PE film, with clear differences in the tensile response along the machine and transversal material directions. While wet processed separators typically present comparable mechanical behavior in different directions (Chen et al., 2014b; Zhang et al., 2016b), we noticed that the highest stresses are measured along the machine direction which is attributed to the higher fibers alignment in the machine direction. In addition, the separator stress-strain response is highly dependent on the strain rate applied. Indeed, a clear dependence on the strain rate is exhibited by the modulus of elasticity, the strain hardening and fracture. A decrease of the modulus of elasticity with decreasing strain rate is observed for both tested material directions. The nominal response of the separator at 0.016/s and 0.0016/s strain rates showed a continuous strain hardening until fracture. Similar response can be

observed at 0.16/s except for the pristine separator that showed a softening before fracture. The softening exhibited by the pristine separator at 0.16/s was not observed for the cycled separator.

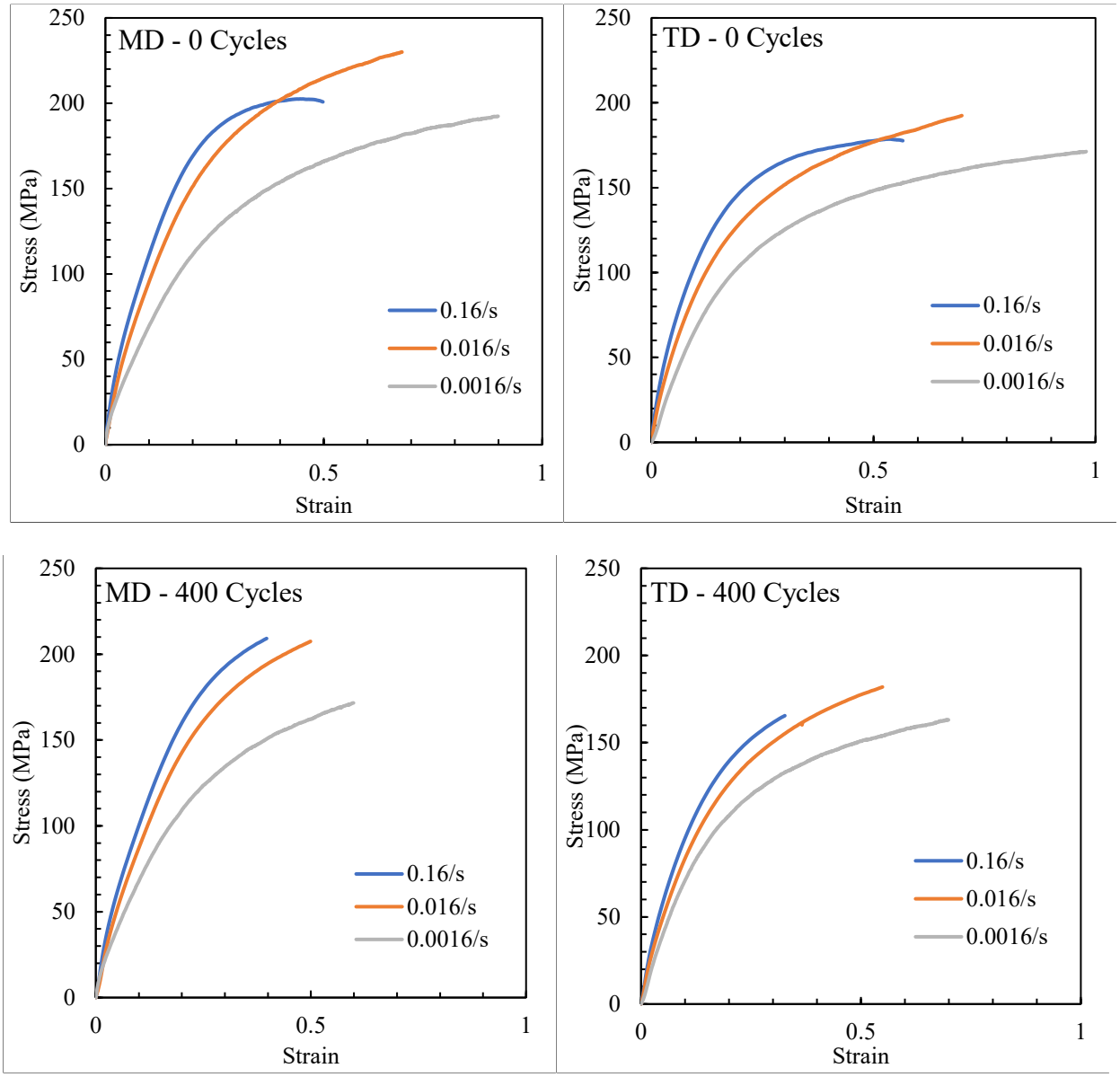

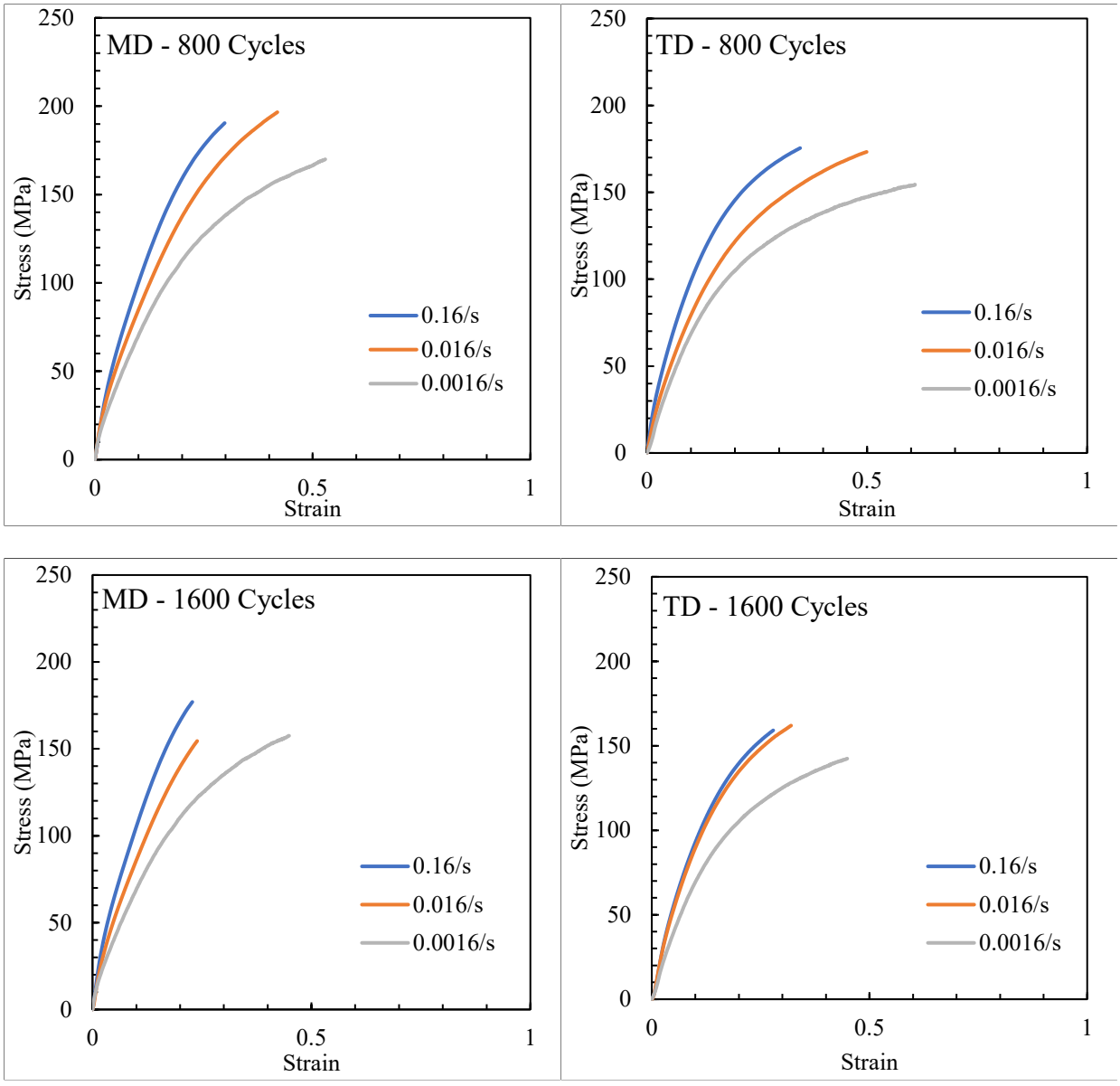

Figure 3.11: Experimental tensile tests in the machine and transversal direction of the pristine and 400, 800, and 1600 cycled separators.

Figure 3.12.a compares the evolution of the modulus of elasticity for different numbers of charging cycles and loading directions. Overall, independently from the loading direction and the cyclic charge history, decreasing the strain rate decreases the modulus of elasticity. For the pristine separator, decreasing the strain rate from 0.16/s to 0.0016/s, significantly decreases the modulus of elasticity from 1835 to 872 MPa in the machine direction, and from 1728 to 745 MPa in the

transversal direction. While for the 1600 cycled separator, decreasing the strain rate from 0.16/s to 0.0016/s, decreases the modulus of elasticity (at a lower rate compared to the pristine one) from 1572 to 843 MPa in the machine direction, and from 1237 to 786 MPa in the transversal direction. While the effect of the cyclic charge history is clearly observed at 0.16/s this effect is subtle for 0.016/s to 0.0016/s. Indeed, at 0.0016/s (MD) the modulus of elasticity decreases only by 29 MPa between the pristine and the 1600 cycled separators compared to a decrease by 490MPa for 0.16/s (TD). Furthermore, the effect of the cyclic charge history on the modulus of elasticity is relatively small after the first large drop between the pristine and the 400 cycled separators. Figure 3.12.b compares the evolution of the strain at yield for different numbers of charging cycles and loading directions. Overall, independently from the loading direction and the cyclic charge history, decreasing the strain rate decreases the strain at yield. This effect is pronounced in the transversal direction. Additionally, the effect of the cyclic charge history on the strain at yield is relatively small. Figure 3.12.c compares the evolution of the toughness for different numbers of charging cycles and loading directions. The toughness is the maximum energy absorbed prior to fracture. It was calculated as the area under the entire engineering stress-strain curve. Overall, an almost linear decrease of the toughness with increasing number of charge cycles is observed. This evolution can be attributed to the accumulation of damage during battery operation. An expected increase of the toughness with decreasing strain rate is also observed. The evolution of the average fracture strain for different numbers of charging cycles and loading directions is shown in Figure 3.12.d. Overall, the failure strain increases with decreasing strain rate and decreases with increased number of charging cycles. While the strains to failure of the 400 and 800 cycled separators are very close, a clear drop of the strain to failure is observed between the pristine and the 1600 cycled separators with an average decrease over all the tested condition of ~50%.

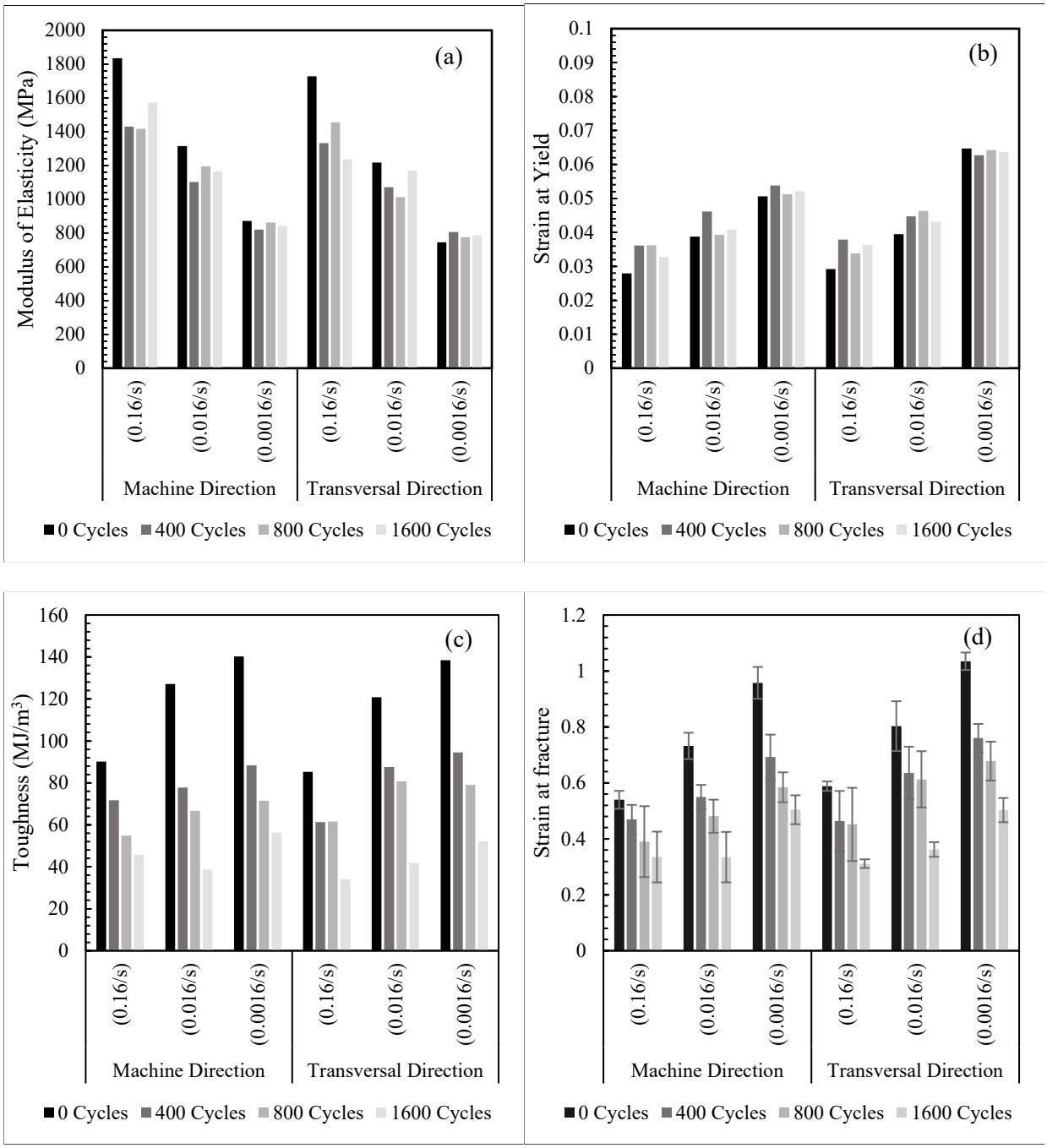

Figure 3.12: The evolution of (a) Modulus of Elasticity, (b) Yield strain, (c) Toughness, (d) Strain at fracture for different directions and strain rates.

3.3.2.2 Punch Testing

Studying the fracture behavior of polymeric film can be challenging with uniaxial tensile tests because of inconsistent edge quality. Biaxial punch tests were performed to eliminate the effect of edge quality and reduce stochasticity. Biaxial test results for the pristine and cycled separators using different punch diameter are shown in Figure 3.13. The load vs displacement curves show an increase in the mechanical load with increasing punch diameter. The 3.2 mm and 6.4 mm punch diameter show a steady almost linear increase up to failure. The 12.7 mm and 25.4 mm punch diameter show an initial steady linear increase followed by a higher-slop linear increase up to failure. Similar behavior was observed in (Zhang et al., 2016b). Additionally, the maximum deformation at fracture increase with increasing the punch diameter. A comparison between the averaged loads vs displacement for the 400, 800, and 1600 cycled separators punched at either the cathode or anode side is also shown in Figure 3.13. The comparison between the anode and cathode side punch results shows that for the 800 and 1600 cycled separators, a higher load is recorded for the anode side. This difference in the punch results is not observed for the 400 cycled separator. Accordingly, we correlate the load needed to punch the surface of the separator with the density of the deposit layer covering it. The punch load-displacement of the pristine/none coated surface is used a reference. Accordingly, the punch load increases with increasing density of the deposit at the punched surface. The SEM micrographs (Figure 3.13) showed that the anode side of the separator is coated, and the deposit density increases with increasing number of charging cycles. Compared to the anode side, the cathode side of the separator is considered not coated (Figure 3.6), indeed very small and scattered deposits were observed. For high cyclic charging conditions, the deposit thickness is comparable to the separator's and hence can't be neglected. Furthermore, since the film is not allowed to slide, we assume that the opposite surface to the punched one

develop higher tensile stresses. Finally, the deposit is a brittle layer consisting of particles not tightly holding together. Accordingly, when the anode side is punched, the deposit layer is compressed and held together while the opposite side (the cathode side) is deforming under tension. Hence, the load in the deposit layer adds up to the load in the separator and overall more force is needed to punch the separator. In contrast, when the cathode side of the separator is punched the deposit layer in under tension and fractures quickly. Hence, the deposits do not contribute to the deformation of the separator (the required punch force is lower) but do affect the ductility of the separator when punched.

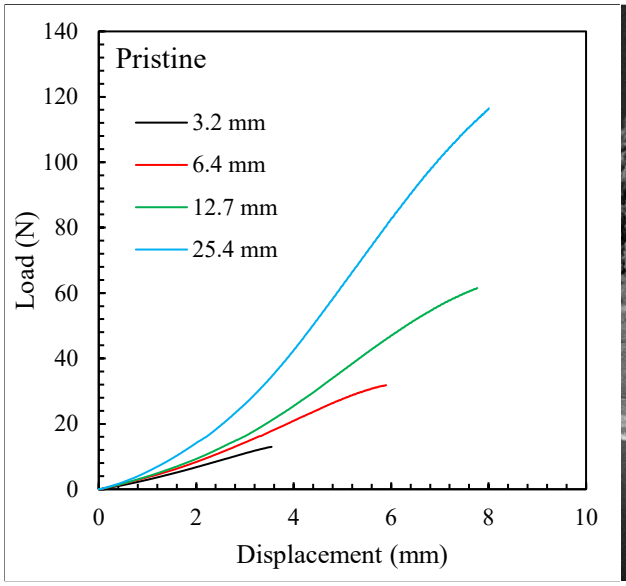

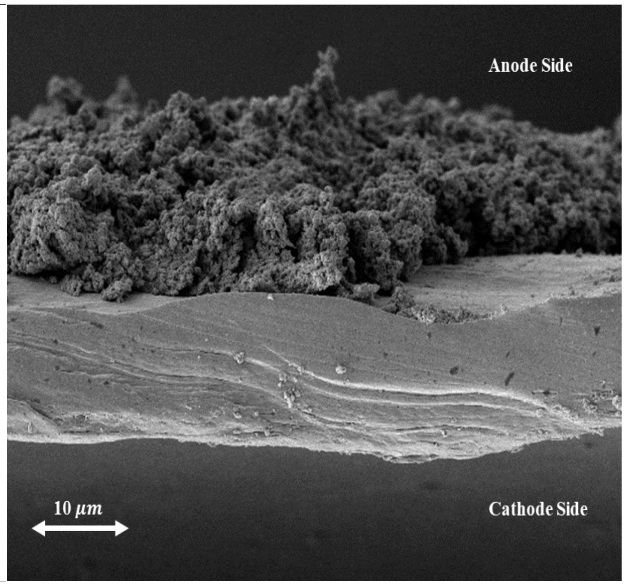

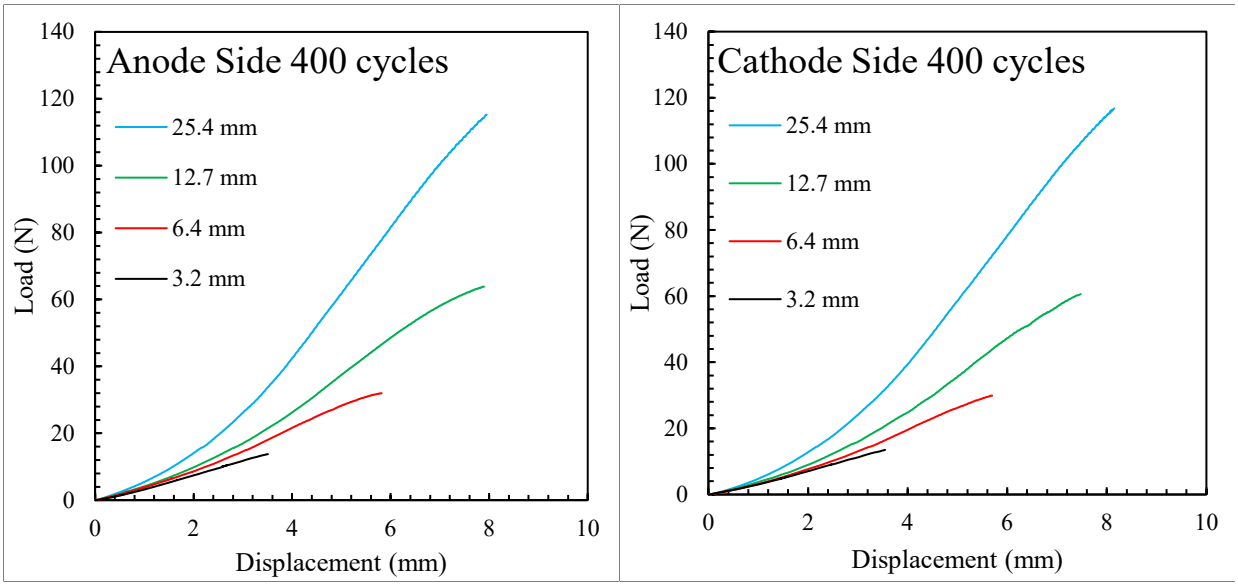
Anode Side 400 cycles
25.4 mm
12.7 mm
6.4 mm
3.2 mm
Load (N)
Displacement (mm)
Cathode Side 400 cycles
25.4 mm
12.7 mm
6.4 mm
3.2 mm
Load (N)
Displacement (mm)

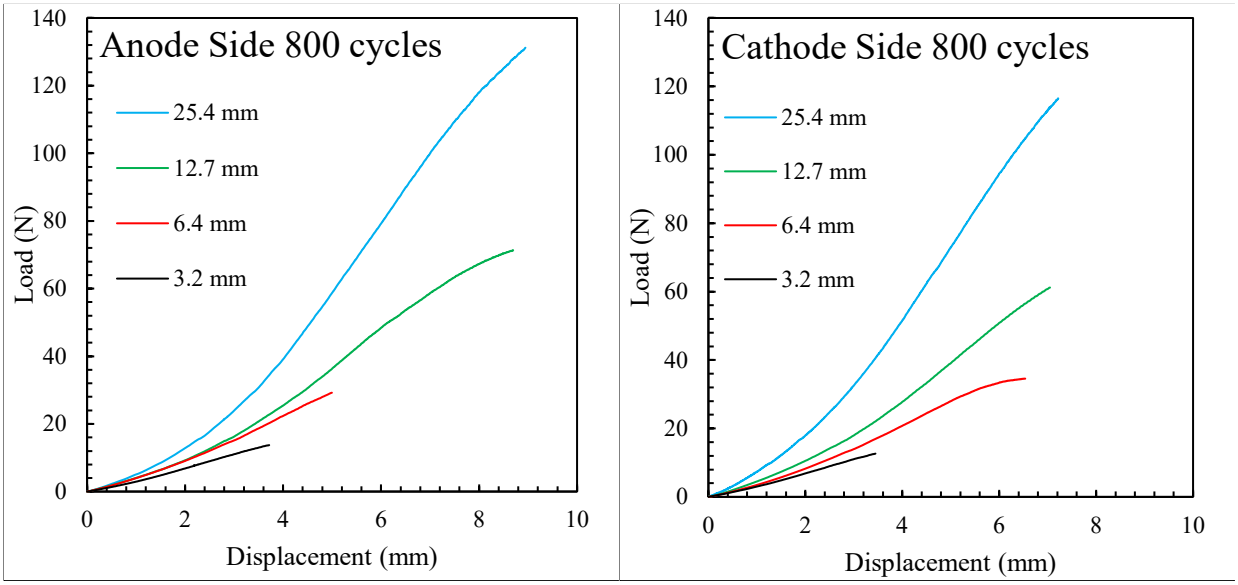
Anode Side 800 cycles
25.4 mm
12.7 mm
6.4 mm
3.2 mm
Load (N)
Displacement (mm)
Cathode Side 800 cycles
25.4 mm
12.7 mm
6.4 mm
3.2 mm
Load (N)
Displacement (mm)

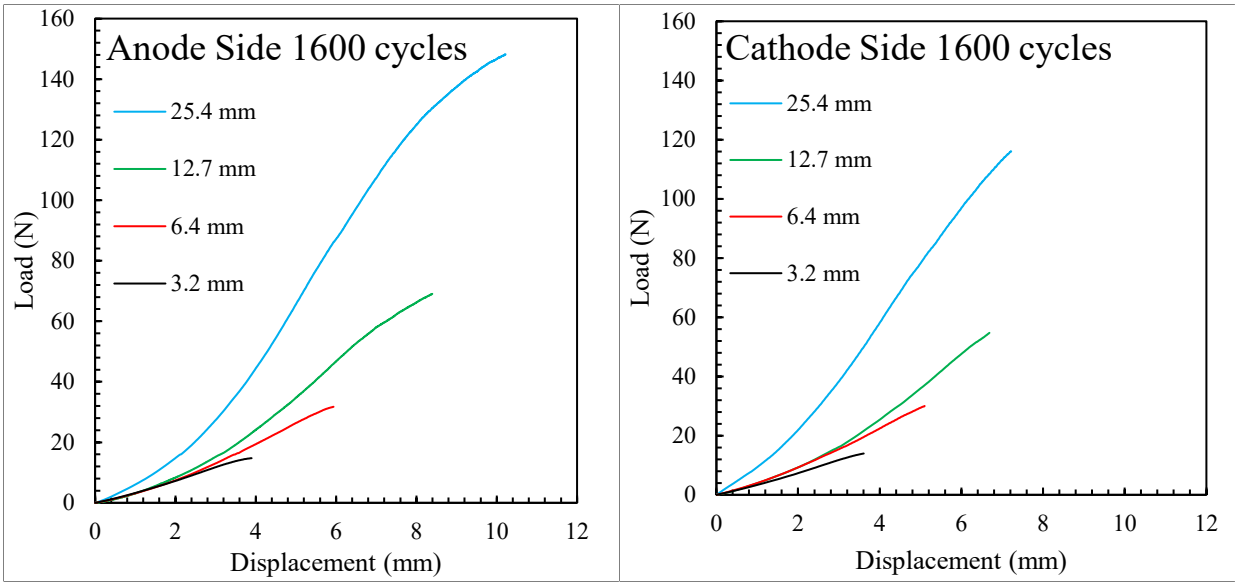

Figure 3.13: Load vs. displacement response under punch testing of pristine and 400, 800, and 1600 cycled separators. SEM micrograph of 1600 cycled separators showing the coated anode side.

The average maximum deformation at fracture under punch loading using different punch diameters and number of charging cycles is shown in Figure 3.14. When compared to the average fracture results of the tensile tests, the standard deviation is lower. The maximum deformation at fracture is approximately similar between the anode and cathode sides for the 3.2 mm and 6.4 mm punch diameters. However, at higher punch diameter, a clear difference in the maximum deformation at fracture between the anode and cathode side is observed. Those observations correlate with the aforementioned explanation. When the anode side is punched, the fracture is controlled by the separator layer which exhibits a higher ductility than the deposit layer. While when the cathode side is punched, the deposit layer controls the fracture. The brittle deposit layer is under tension resulting into cracks formation around which stress rises to accelerate the fracture in the separator layer. Additionally, for the anode side, we observe an increase in the maximum deformation at fracture between the 0 and 1600 cycled separator. While, for the cathode side, we

observe a decrease in the maximum deformation at fracture between the 0 and 1600 cycled separator. Similar results were reported by Zhang et al., (2017). This decrease can be associated to the separator fiber localized fracture reported by the SEM analysis.

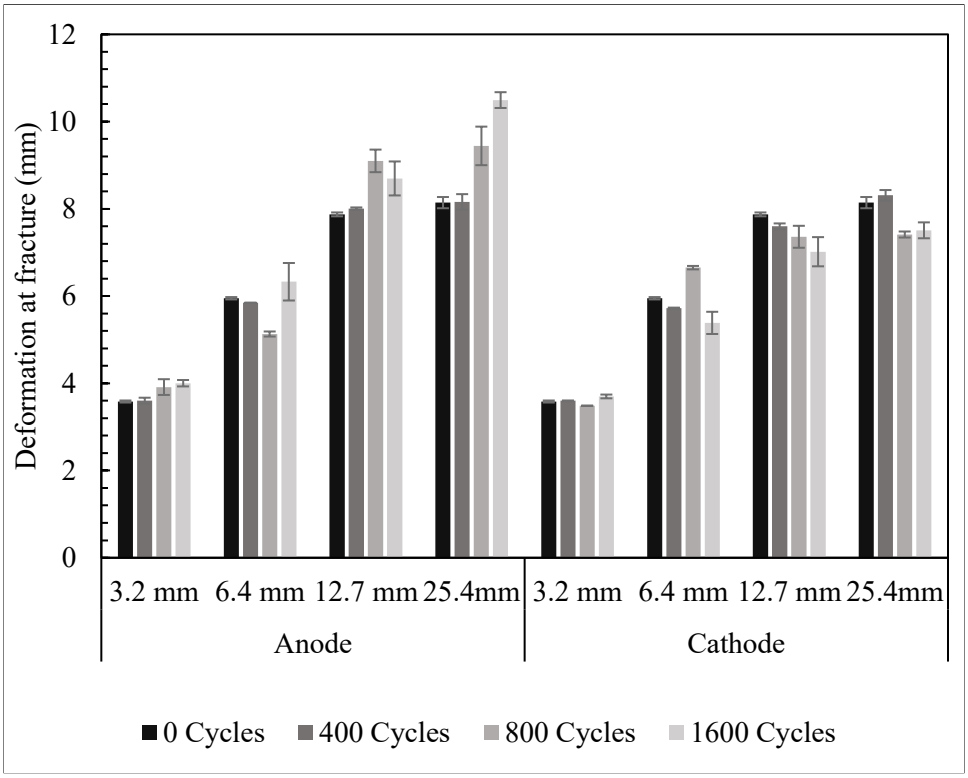

Figure 3.14: Deformation at fracture for different punch diameters and punch separator side.

3.4 Discussion and Damage Mechanisms

The separators' porosity, thickness, and pore structure are the main factors associated with the increase or decrease of ionic mobility which affects the capacity of the battery at high charging rate (Djian et al., 2007). During charge and discharge, the electrolytes decompose and reduce at the anode resulting in solid electrolyte interphase (SEI) layer formation (validated by our FTIR analysis). From Figure 3.4, the deposits density on the anode side increase with an increasing number of cycles. At 1600 cycles, the SEI deposits fully cover the separator anode side. The battery capacity drops significantly at around 100 cycles (Table 3.2) before the appearance of any

substantial SEI deposit layer; only few deposit spots are observed on the anode side of the 400 cycled separator. The SEI deposit layer on the anode side can potentially cause blockage of pores, which result in battery capacity decrease. Furthermore, our cycled battery pouches were sandwiched between two plates with a 1 N.m compressive load applied to the bolts. This compressive load, applied to the separator thickness, can be correlated to pores density decrease. Peabody & Arnold, (2011) reported that the porosity in the separator decreased with increasing external compressive stresses influenced by compressive creep and operation temperature. Cross-sectional SEM analysis of our cycled separators (Figure 3.8) showed pore closure. While the pore blockage by deposits and pore shrinkage due to compression are not the main reason for the drop in capacity, they are both potentially factors associated with the ionic transfer decreases causing an increase in the internal resistance and a decrease in the capacity retention. Additionally, dendrites start forming when lithium-ions start depositing on the anode surface in an irregular manner during charging, which deteriorates the battery performance, and can cause safety concerns (Lee et al., 2021; Rosso et al., 2001; Xu et al., 2014). The dendrite formation on the anode side leads to a low cycling efficiency.

Chemical characterization of the separator surface using FTIR and XPS analysis provides insight into the potential mechanisms of degradation; FTIR is mainly used for detecting organic components while XPS is used to detect the inorganic components. XPS analysis (Figure 3.9) showed that the cycled separator contained Cu, P, F, O, C with higher intensity of Cu, P and F on the anode side. The P, F, and O are potentially electrolyte salt and solvents decomposition products (X. Chen et al., 2012), and Cu results probably from the degradation of the current collector. The FTIR analysis (Figure 3.10) shows two absorption bands at 3588 and 3364 cm^{-1} associated with to O-H bond stretching in free bond and intermolecular bonds respectively. Moreover, several IR

absorption bands of lithium hexafluorophosphate ($LiPF_6$) are observed; like at 845, 559 and 1636 cm^{-1} (Aurbach et al., 1994; Kock et al., 2012). The FTIR analysis do not point to the presence of any functional group, which might be associated to a chemical reaction resulting from the separator environmental degradation (Chain scission or crosslinking). Consequently, based on the FTIR and XPS analysis results we can assume that the PE separator does not undergo chemical degradation. Compared to Polypropylene (PP) and trilayer PP/PE/PP separators, PE separators have the most stable electrochemical behavior (X. Chen et al., 2012).

For a thorough understanding of the battery operation conditions, Figure 3.15 schematically represents the battery internal components reaction to charging and discharging. During charging and discharging cycles, the battery separator is subjected to electrochemical, thermal, and mechanical loading simultaneously. The main requirements for the separator is to be inert, and mechanically robust to endure the deformations resulting from battery assembly, cyclic charging, and battery pack external forces (strapping battery cells in series and parallel) (Huang, 2011; Oh et al., 2016). During battery operations, the lithium insertion electrochemical process results in a large volumetric expansion and shrinkage of the electrode materials (Timmons and Dahn, 2007), causing large deformation in the separator. In addition, a temperature increase due to the chemical reaction causes thermal stresses to arise from the battery components with different coefficients of thermal expansions (Shi et al., 2011). Both processes initiate mechanical and thermal cyclic loading on the battery separator. Since the XPS and FTIR analysis did not reveal the presence of chemical degradation in the separator, we can assume that thermal and mechanical cycling provoke microstructural alterations associated with the ductility loss.

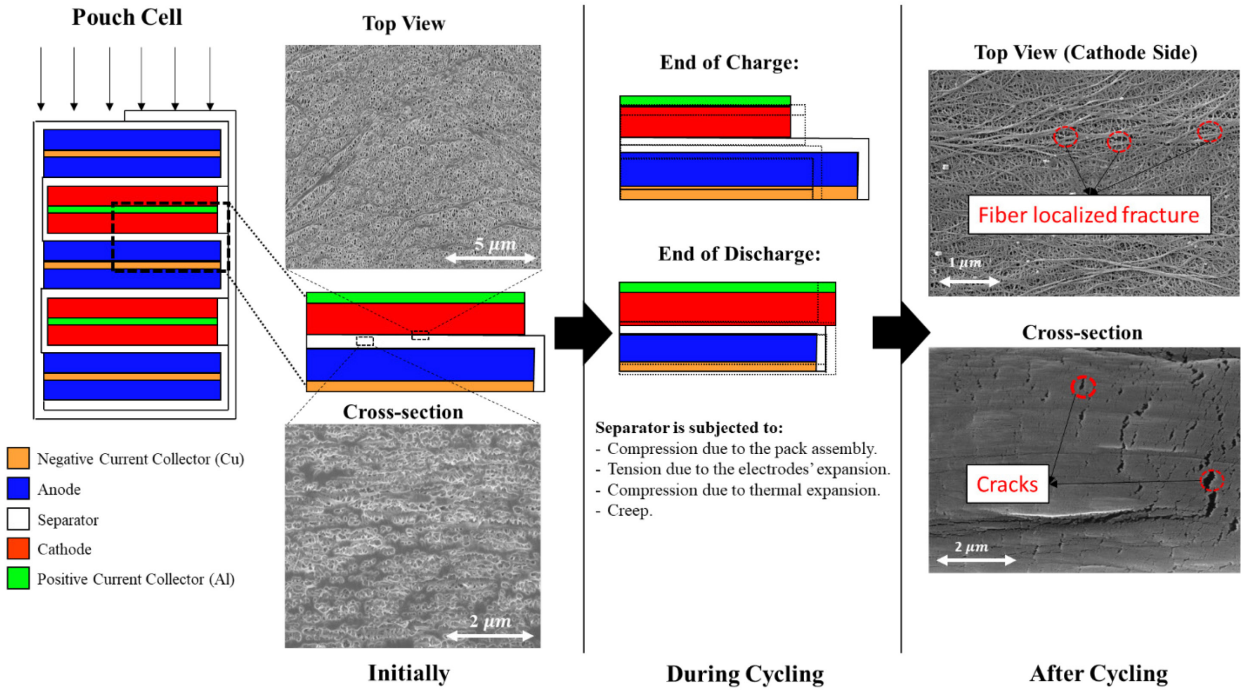

Figure 3.15: Pouch cell and separator deformation during cyclic charging.

Figure 3.15, shows that the electrode deformation due to the electrochemical reaction and the temperature causes significant deformation in the battery separator. During charge, the cathode shrinks, and the anode expands subjecting the separator to a tensile force along the machine direction. The battery pouches were subjected to a constant voltage (during continuous cyclic charging) with a current drop to 5% at the end of charge and discharge cycles and hold periods subjecting the separator to two types of creep deformation: tensile loading (due to anode expansion) and persistent compressive stress (due to compressive load applied on the pouch assembly setup). The high number of charging cycles cause damage to accumulate in the form of pore closure resulting from compression creep along the thickness, and fiber fracture and through thickness crack formation resulting from tensile creep along the machine direction. Indeed, localized fiber fracture can be observed on the surface of the separator (Figure 3.7), which can potentially cause enlargement of the pores and reduction in ductility. The localized fiber fracture

is believed to be favored by the cyclic tensile creep and the increase in temperature. Furthermore, the through thickness cracks observed in the 1600 cycled separators also contribute to the separator loss of ductility.

Our experimental results suggest that tensile creep is a major factor contributing to the mechanical degradation of the battery separator. To better understand the polyethylene separator sensitivity to creep, creep testing was conducted on the strip-shaped uniaxial tensile specimens using several engineering stresses. The creep test sensitivity was tested along the machine direction. Several engineering creep stresses (60, 70, 80, and 90 MPa) with a ramp loading of 0.1 MPa/s were applied. The creep stresses were selected based on preliminary multi-physics simulations of the battery pouch charge discharge conditions. All tests were left until a maximum displacement of 60 mm was reached. The creep displacement vs time curves are presented in Figure 3.16. It is observed that the battery separator are very sensitive to creep. Furthermore, all tests were interrupted in the primary stage of creep characterized by a rapid increase in the deformation. The high creep sensitivity and creep deformation correlate with the development of significant damage in the separator.

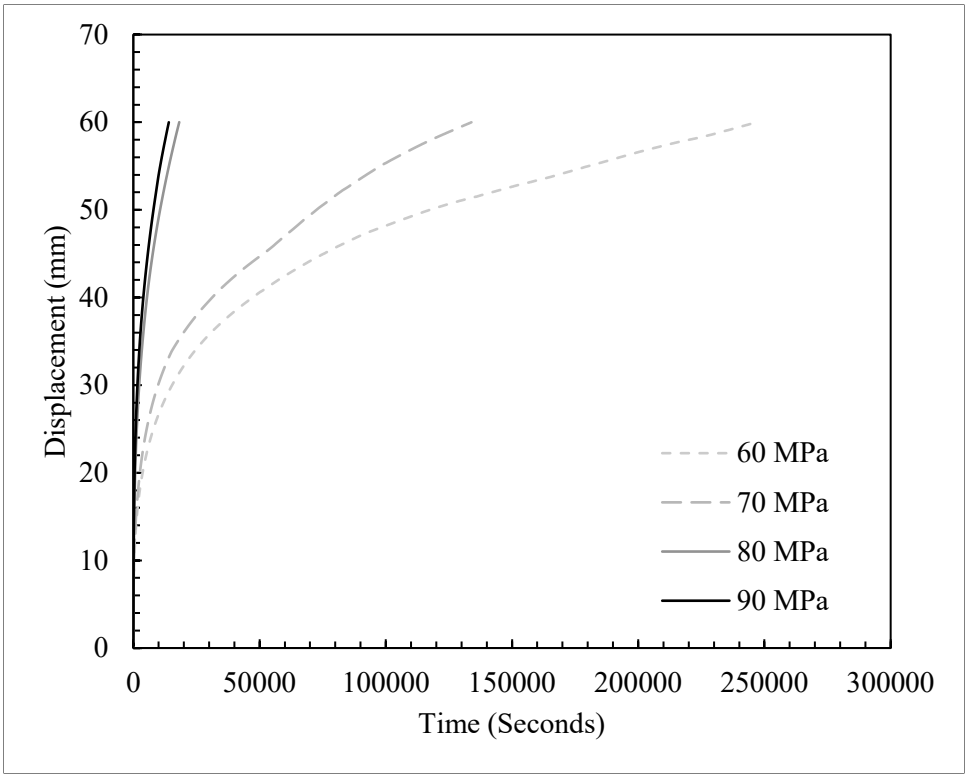

Figure 3.16: Creep test displacement as a function of time for 60, 70, 80, and 90 MPa.

3.5 Conclusion

Lithium-ion batteries emerged as preferred energy source for electrical vehicles driven by their excellent life cycle, lighter weight, affordability, high energy density and high power per mass battery unit. While lithium-ion batteries present numerous advantages, the capacity loss under fast charging conditions poses big challenges. The objective of this work is to guide future improvement of lithium-ion batteries manufacturing by understanding the effect of cyclic fast charging on the mechanical and physico-chemical properties of the separator. For that purpose, six battery pouch cells were subjected to cyclic fast charging conditions at 4C (fast) charge rate and 0.5C discharge rate up to 400, 800, and 1600 cycles under an ambient temperature of 20 degrees Celsius. Once the cyclic fast charging is completed, the battery pouch cells were fully discharged, carefully disassembled and its components are allowed to dry. While the cathode side of the

separators did not show any deposits for all cyclic charging conditions, the anode side showed an increase in the deposit density with increasing number of charging cycles. Indeed, the 1600 cycled separator presented the highest deposits density. The XPS and FTIR analysis of the separator surfaces did not reveal the presence of chemical degradation. XPS analysis showed that the cycled separator contained P, F, O that are potentially electrolyte salt and solvents decomposition products. FTIR showed several IR absorption bands of lithium hexafluorophosphate ($LiPF_6$). The SEM micrographs of the separator showed a layer of deposits from the anode side while small scattered deposits were seen on the cathode side. Under continuous cyclic charging the separator is subjected to two types of creep deformation: tensile loading along the machine direction and persistent compressive stress. The high number of charging cycles cause damage to accumulate in the form of pore closure resulting from compression creep along the thickness, and fiber fracture and through thickness crack formation resulting from tensile creep along the machine direction. Consequently, the mechanical properties of the cycled separators presented a decrease in the toughness and ductility with increased number of charging cycles. Additionally, under punch tests the cycled separators presented different behaviors between the cathode and anode side of the separator. Samples punched from the anode side showed a higher overall average fracture than the specimens punched from the cathode side.

In summary, under fast charging conditions the separator is subjected to harsh mechanical loading in a battery pack. The fast-charging conditions can affect the separators' mechanical integrity. The separator is subjected to a compressive force (along the thickness) from the battery pack assembly, accompanied by tensile force (along the machine direction) resulting from the electrodes' expansion. Consequently, the separator is subjected to creep caused by the hold period and the repeated charging cycles. The high number of charging cycles cause damage to accumulate

in the form of pore closure resulting from compression creep along the thickness, and fiber fracture and through thickness crack formation resulting from tensile creep along the machine direction. While most of battery degradation characterization approaches are postmortem and focus on the chemical degradation of the separator, further investigations should explore quantifying the porosity change, and thermal, compressive, and tensile stresses in the separator under fast charging conditions. Hence, our future work will be focused on modeling, validating, and predicting the temperature change and the stress distribution and evolution in the separator during battery fast cyclic charging.

Chapter 4 Multiphysics Modelling of a Lithium-Ion Battery Cell for Prediction of Stress Distribution in the Separator Under Fast Charge Condition

Automotive industries are quickly shifting to electrical vehicles to reduce their carbon footprint. The Lithium-ion battery is the state-of-art tool for energy storage in electrical vehicles. For wider spread of electrical vehicles, one of the main challenges is to develop safe and fast charging technologies to significantly reduce the batteries charging time while preventing any unsafe conditions such as short-circuits due to separator failure. To server this purpose, a novel battery cell model for prediction of stress distribution inside a battery pouch cell during fast charging is presented. First, a Multiphysics model is developed to predict the core temperature of the battery, the loads applied, and the displacement behavior in the battery pack array. The thermal and mechanical behavior of an NMC 622 pouch cell in a battery pack array is characterized and discussed under fast charging conditions. A robust parameter identification scheme is proposed to determine the model parameters based on experimental data. The first principal stress in the separator was shown to be around 70 MPa. Creep and fatigue tests were conducted on the separator to generate deformation damage. The results show that 70 MPa can cause significant damage in the separator after repeated fast charging.

4.1 Introduction

Due to the volatility of the world oil markets and the sustainability policies among companies and authorities limiting carbon footprint, the automotive industry has been swiftly switching towards electrical vehicles (EVs) as well as hybrid electric vehicles (HEVs) as a promising solution. Not only do EVs reduce the emission of greenhouse gases, pollutants, but it also provides a solution to mitigate societal cost by reducing the consumption of fuel resources. As EVs increase their market share at a fast pace compared to traditional internal combustion engines, an extremely high demand in high efficiency energy storage systems (ESSs) has been observed. Electrochemical energy storage systems provide a clean, convenient, and efficient way to store and deliver energy on demand in EVs.

Among various types of electrochemical ESSs, lithium-ion batteries (LIBs) are the current state-of-art chemistry used technology in EVs (Alaoui, 2013; Iclodean et al., 2017; Pesaran et al., 2009) due to their high energy/power density over broad temperature operation range, low self-discharge when unused, and reliable recharging capability (Ramadesigan et al., 2012). Compared to other cell chemistries, such as nickel-metal hydride (NiMH), LIBs can achieve nearly two times the specific energy and energy density (Bandhauer et al., 2011). LIBs are composed of four main components which are the anode, cathode, separator, and current collectors altogether submerged in liquid electrolyte (Lukic et al., 2008).

During battery operation, LIBs are subjected to electrochemical reactions, thermal energy, and mechanical stresses acting simultaneously which can severely impact their performance and lifespan if not managed correctly. Throughout the electrochemical process, many complex processes occur at the same time such as charge transport, chemical reactions at the electrode, and intercalation or deintercalation. Lithium ions (Li+) are transferred between the anode and cathode

by passing through the porous separator. The ions are transported via migration and diffusion driven by gradients in potential and concentration respectively (Song et al., 2020). Two main sources of heat are generated in a lithium-ion battery cell: entropy change and joule heating (Benger et al., 2009; Jeon & Baek, 2011). Entropy heat compensates for the residual energy when converting energy between enthalpy change and the Gibbs free energy (Electrical work) (Onda et al., 2006). Indeed, entropy heat is reversible and generally exothermic during discharge and endothermic during charge. In contrast, Joule heating is irreversible and exothermic regardless of the battery operation.

High heat generation can cause temperatures rise which can lead to a decrease in the LIB efficiency, and a decrease in their lifespan (Wang et al., 2014). In addition to the electrochemical reactions mentioned previously, side reactions such as lithium plating occur in the battery. These reactions are significantly affected when the temperature is outside the normal operating range and can severely affect the lifespan and efficiency of the battery. Moreover, excessive temperature may lead to performance degradation due to the decomposition or degradation of the material, release of oxygen and flammable gas, and cause internal short circuit and as a result thermal runaway (Q. Wang et al., 2019). Both the electrochemical process and heat generation induce mechanical loads in the battery components. The former process induces a volumetric change of the active material due to the intercalation processes of lithium-ions, while the latter process changes the volume of all the cell components due to thermal expansion.

In LIBs, a critical component is the separator which is a porous membrane positioned between the electrodes. The essential function of the separator is to prevent direct contact between the electrodes, while maintaining ionic flow via electrolyte (Arora & Zhang, 2004). Indeed, the separator impedes the physical contact of the positive (cathode) and negative (anode) electrodes

and acts as an insulator for electrons, while the pores in the separator contain electrolytes which allow the exchange of lithium-ions between the electrodes. Therefore, the separator is the most crucial safety component inside the lithium-ion battery preventing contact between the positive and negative electrodes and internal short circuits. Such crucial role translates to several requirements for the thermal and mechanical properties of the separators. First, the separator should be chemically stable under the reductive and oxidative conditions encountered during battery operations (Lee et al., 2014). The separator should not degrade or interfere with the electrochemical reaction. Degradation in the separator can weaken its mechanical integrity. Secondly, the separator should have low thermal shrinkage in the machine and transversal direction typically less than 5% after 60 minutes at 90 degrees Celsius (Baldwin et al., 2010). This general requirement prevents the exposure of electrode edges due to shrinkage of separator dimensions and allowing the edges to be in contact which can induce short circuit. Additionally, the separator should have a high-temperature melt integrity to avoid thermal runaway when the cell is exposed to high temperatures. A shutdown temperature of 130 degrees Celsius or lower is usually enough to control thermal runaway in LIBs. Finally, the separator should be mechanically robust to withstand the mechanical stresses encountered during the battery assembly, battery operation, and under abuse conditions. A high tensile stress and a high puncture strength are both required to avoid rupture and penetration of electrode material which can cause short circuits in the battery (Huang, 2011). Under fast charging conditions, damage in the separator can accumulate in the form of pore closure along the thickness, and fiber fracture and through thickness crack formation along the machine direction. Due to both damage mechanisms, the separator loses ductility which weakens its mechanical integrity (Makki et al., 2022). Given its integral role in the battery safety and functionality, an accurate characterization and modeling of the stress distribution

in the separator is needed to address safety concerns under fast charging conditions.Many efforts have been devoted to characterizing and modeling the heat transfer during charge and discharge cycles. Indeed, an accurate characterization of the mechanisms occurring inside the cell can provide a useful foundation for innovative and practical solutions leading to improvement in the lifespan of battery cells and providing guidance for the cell design. The authors Y. Chen & Evans, (1996) conducted a thermal analysis of lithium-ion batteries during charge/discharge cycles using a mathematical model. The model showed significant heat accumulation in the battery under continuous high-rate charge and discharge. This can lead to thermal runaway because the battery temperature may keep increasing. In other works, a physical coupled thermal-electrochemical model was developed to predict the heat generated in the components: matrix and solution (Srinivasan & Wang, 2003). The model incorporated three types of heat generation consisting of the reversible, irreversible, and ohmic heat. The model showed that reversible heat was significant at all charge rates. Moreover, the ohmic heat was negligible in the matrix irrespective of the charge rate. The irreversible and ohmic heat in the electrolyte increase when the charging rate increase. A thermo-electric battery model was developed to predict the voltage, current and heat generated in the electrodes (Olszanski et al., 2012). The model uses an empirical approach which links the current-voltage to the temperature in the cell. Additionally, lumped parameter thermal models have been also proposed for battery thermal management systems. Kim et al., (2014) developed a 1D radial thermal model for cylindrical battery cells. The thermal model uses a polynomial approximation of the temperature profile inside the battery, and a dual Kalman filter is used to identify the convection coefficient and battery core temperature. Other works include using phase change material or microchannel for thermal management (Jin et al., 2014; Ling et al., 2014).

While the overheating in lithium-ion batteries can cause significant degradation in the battery performance due to capacity fades and thermal runaways (Ramadass et al., 2002; Q. Wang et al., 2012; Yuksel & Michalek, 2012), another important aspect is the swelling and mechanical stresses generated in the battery components during charge and discharge cycling. Indeed, mechanical stresses are induced by swelling due to the volumetric expansion of the electrodes and thermal expansion of the battery components. Both mechanisms can cause squeezing of the soft separator (Gor et al., 2014), which can cause the shrinking of large pores reducing ion transfer and as a consequence internal resistance and capacity fade increase (Peabody & Arnold, 2011). Currently, there is no method to evaluate the stresses inside the battery. Researchers use Multiphysics finite element modeling to predict the stress and deformation in the battery components. Xiao et al., (2010) used a multi-scale model to predict the stresses in the polymeric separator. The model use a 1D macroscopic battery model coupled with a meso-scale representative volume element battery sub-model. Shi et al., (2011) developed a Multiphysics model for pouch cells to predict the stresses in the battery separator. The model used a 1D electrochemical model coupled with a 2D spherical particle model. The model calculates the lithium concentration at each electrode and the heat generated and projected them to the macroscale 2D model to find the stresses in the separator. The swelling and force generated during battery cycling has been the subject of research. Oh & Epureanu, (2016a) developed a thermal swelling model to predict the swelling in the battery due to temperature variation. The temperature in the battery was modeled as a parabola and a 1D heat conduction model was used to predict the temperature. In their other works, (Oh & Epureanu, 2016b) used a phenomenological force and swelling model to predict the dynamic swelling in the battery. Modeling the stresses generated in the battery at fast-charging conditions has not been fully addressed in the literature. To address

this gap, this work aims to propose a modeling framework using Multiphysics to predict the temperature, displacement, force on the battery cell, and the stresses in the battery components at different charge rates, and different packing conditions.

For that purpose, in this work a Multiphysics model has been developed consisting of three main components: (1) a 1D electrochemical model, (2) a lumped parameter model, and (3) a 2D solid mechanics model. A fast charge and discharge cycling is conducted on a lithium-ion battery cell with temperature, load, and displacement measurements. The 1D electrochemical is used to predict the heat generated in the battery cell. The heat generated is used as an input for a lumped parameter model which mimics the battery cell behavior in a battery pack array. The model parameters are optimized using a non-linear regression. Finally, the lithium-concentration and temperature are used in the solid mechanics model to predict the stresses inside the battery and specifically in the separator.

The chapter is organized as follows: In section 4.2, the Multiphysics model is discussed, and the constitutive equations are presented. In section 4.3, the lithium-ion battery materials are discussed. Additionally, the temperature, load, and displacement experiments are explained in detail. In section 4.4, the experimental results are presented and discussed. Additionally, the model parameters identification procedure is presented, and the model capability is assessed. In section 4.5, additional tests were conducted to assess the damage in the separator at the predicted stress. Finally, a summary of the work is provided.

4.2 Multiphysics Model

During charge and discharge cycles, the lithium-ion battery is subjected to electrochemical, thermal, and mechanical phenomenon acting simultaneously. Each phenomenon is described by a set of equation and is coupled with another physical entity using a physical parameter. The

framework of the multi-physics model is divided into three components. The first component uses a simple 1D model to predict the electrochemical reaction and heating source in the battery based on the charging rate provided. The model is composed of three parts: Anode, separator, and cathode. The second component is a Lumped parameter model to predict the load, displacement, and temperature in the battery when it is packed in a battery array pack. The model composed of three parts: a thermal model for heat transfer, a spring model, and a linking equation which links the thermal model to the spring model. The last component is a 2D solid mechanics model which calculates the stress distribution in the separator based on the temperature predicted in component 2 and the lithium concentration in the electrodes predicted in component 1. Figure 4.1 shows all three components with the input/output variables. In what follows, a detailed description of each of the models is provided.

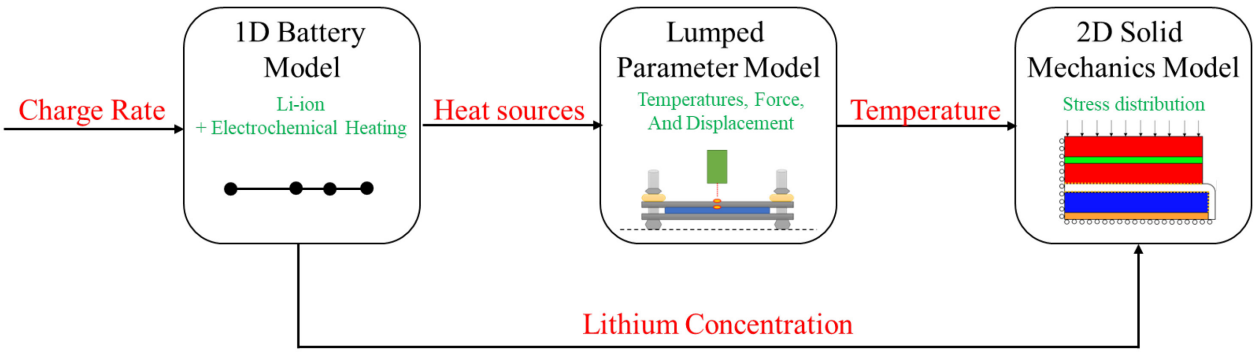

Figure 4.1: Flowchart of the Multiphysics Model.

4.2.1 Component 1: 1D Battery Model

The model uses a 1D component to predict the electrochemical reaction and heat sources in the battery. Li-ion batteries are composed of three components placed in electrolyte: Cathode, anode, and separator. During the cell assembly, the cell is usually discharged. During charging,

lithium-ions move from the cathode to the anode through the separator. Concurrently, electrons move from the cathode to the anode from an external circuit. In general, this process decreases the anode's potential and increases the cathode potential leading to an increase in the voltage of the cell. The model calculates the lithium concentration and heat generation in the anode and cathode after 1 full charging cycles.

When the battery is charged or discharged, the base for all other entities is the electrochemical reaction occurring at the electrodes. Mathematical models have been fully established for the electrochemical reaction, and the equations are provided (Doyle et al., 1993; Doyle & Newman, 1996).

The first dimension is the thickness of the model components. The mesh size is automatically generated by COMSOL based on the physics, using a finer mesh near the separator. The 1D model is shown in Figure 4.2.

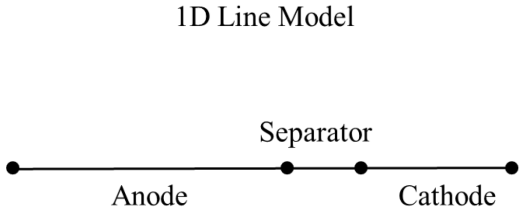

Figure 4.2: Component 1, 1D electrochemical model.

The volume fraction of the electrodes is defined by:

$$\varepsilon_l^i = 1 - \varepsilon_s^i - \varepsilon_{filler}^i \tag{4.1}$$

Where ε_s^i is the active material volume fraction, ε_l^i is the electrolyte volume fraction (porosity), and ε_{filler}^i is the binder and fillers volume fraction. The superscript i denotes the electrode under consideration (p for positive and n for negative).

4.2.1.1 Solid Phase

The following equations apply to the solid phase of the anode and cathode. The active material in the electrodes is assumed to be composed of spherical particles. Fick's second law describes the transport in the solid electrode particles and predicts the change of concentration field with time by the following equation in spherical coordinates:

$$\frac{\partial c_s^i}{\partial t} = \frac{D_s^i}{r^2}\frac{\partial}{\partial r}\left(r^2 \frac{\partial c_s^i}{\partial r}\right) \tag{4.2}$$

where r is the particle radius coordinate, c_s^i is the lithium concentration in the solid particle phase, and D_s^i is the diffusion coefficient of lithium-ion in solid electrode particles. The equation assumes a constant diffusion coefficient of lithium-ions in the solid phase. From symmetry, the first boundary condition yields $-D_s^i \frac{\partial c_s^i}{\partial r}\Big|_{r=0} = 0$, since there is no flux at the center of the particle. The second boundary condition relates the pore wall flux across the interface and the rate of diffusion of lithium-ions into the solid/liquid interface yielding $-D_s^i \frac{\partial c_s^i}{\partial r}\Big|_{r=r_p} = J_i$, where r_p is the particle radius and J_i is the pore wall flux of lithium ions.

The conservation of charge in the solid phase is governed by Ohm's law:

$$\frac{\partial}{\partial x}\left(\sigma_{eff}^i \frac{\partial \varphi_s}{\partial x}\right) = a_v F J_i \tag{4.3}$$

Where σ_{eff}^i is the effective conductivity determined by $\sigma_{eff}^i = {\varepsilon_s^i}^{1.5}\sigma_s^i$, φ_s is the potential in the solid phase, a_v is the particle specific surface area, and F is the Faraday's constant. The first boundary condition is provided at the interface between the current collector and the positive electrode where the charge flux is equal to the current density I_{app} applied to the cell $-\sigma_{eff}^i \frac{\partial \varphi_s}{\partial x}\Big|_{x=0} = I_{app}$. The second boundary condition is at the interface between the electrodes

and separators which corresponds to no charge flux: $-\sigma_{eff}^{i}\frac{\partial\varphi_s}{\partial x}\Big|_{x=L_N} = -\sigma_{eff}^{i}\frac{\partial\varphi_s}{\partial x}\Big|_{x=L_N+L_{sep}} = 0$,

where L_N and L_{sep} are the negative electrode and separator's thicknesses, respectively.

4.2.1.2 Liquid Phase

The following equations apply to the liquid phase in the electrodes and the separator. To account for lithium species transport and participation in reactions, concentrated solution theory is used (Doyle et al., 1993; Smith et al., 2007, 2008). The material balance for a salt in the liquid phase is given by:

$$\varepsilon_l^v\frac{\partial c_l^v}{\partial t} = \frac{\partial}{\partial x}\left(D_{eff,l}^{i}\frac{\partial c_l^v}{\partial x}\right) + (1-t_+)a_v J_i \tag{4.4}$$

where ε_l^v denotes the electrolyte volume fraction in the component v, c_l^v is the lithium concentration in the electrolyte, $D_{eff,l}^{i}$ is the effective diffusion coefficient in the electrolyte given by $D_{eff,l}^{i} = {\varepsilon_l^i}^{1.5}D_l^i$, and t_+ is the transport number. The superscript v denotes the component under consideration (p for positive, n for cathode, and sep for separator). For the separator, the pore wall flux is equal to zero. No mass flux at the two ends of the cell, hence $\frac{\partial c_l^v}{\partial x}\Big|_{x=0} = 0$ and $\frac{\partial c_l^v}{\partial x}\Big|_{x=L} = 0$.

The charge balance in the liquid phase is based on Ohm's law:

$$-\frac{\partial}{\partial x}\left(\kappa_{eff,i}\frac{\partial\varphi_l}{\partial x}\right) + \frac{2RT(1-t_+)}{F}\frac{\partial}{\partial x}\left(\kappa_{eff,i}\frac{\partial(\ln c_l^v)}{\partial x}\right) = a_v F J_i \tag{4.5}$$

Where $\kappa_{eff,i}$ is the effective conductivity, φ_l is the potential in the liquid phase, R is the ideal gas constant, and T is the temperature. At the two ends of the cell, there is no current flow in the liquid phase. The boundary condition corresponding to no current flow yields $\frac{\partial\varphi_l}{\partial x}\Big|_{x=0} = \frac{\partial\varphi_l}{\partial x}\Big|_{x=L} = 0$.

4.2.1.3 Charge Transfer at the Electrode/Electrolyte Interface

The pore wall flux at the electrode/electrolyte interface is determined by the Butler-Volmer equation which describes the relationship between electrical current on an electrode, the electrode potential and the local specie concentration at the interface between electrode and electrolyte. Specifically, the rate of transfer of lithium ions from the electrolyte to the active material is controlled by the local deviation of the surface potential with respect to its equilibrium value. The relation linking the charge balance and material balance (applicable to both electrodes) is given by:

$$J_i = a_v i_{ex} \left(\exp\left(\frac{\alpha_a F \eta_i}{RT}\right) - \exp\left(\frac{-\alpha_c F \eta_i}{RT}\right) \right) \tag{4.6}$$

Where i_{ex} is the exchange current density, η_i is the overpotential of the intercalation reaction, and α_a and α_c are the charge transfer coefficients for oxidation and reduction respectively, assumed to be equal to 0.5. Both the forward rate of the anodic process and the backward rate of the cathodic process are given in Equation 4.6.

The exchange current density is given by:

$$i_{ex} = F k_i \left(\frac{c_l^i}{c_{l,ref}}\right)^{\alpha_c} \left(c_{s,max}^i - c_{s,surf}^i\right)^{\alpha_c} \left(c_{s,surf}^i\right)^{\alpha_a} \tag{4.7}$$

Where k_i is the reaction rate constant, c_l^i is the concentration of lithium-ions in the electrolyte, $c_{s,surf}^i$ is the concentration of lithium-ions on the surface of the solid electrode, and $c_{s,max}^i - c_{s,surf}^i$ is the available space for lithium intercalation.

The overpotential is given by:

$$\eta_i = \phi_s - \phi_l - U_i \tag{4.8}$$

Where ϕ_s is the potential of the solid electrode, ϕ_l is the potential of the electrolyte, and U_i is the open circuit potential.

4.2.1.4 Thermal Phenomena

The heat transfer during the electrochemical reaction is governed by a transient heat conduction equation. For most battery systems, the convection term can generally be neglected and the equation simplifies to (Gu & Wang, 2000):

$$\rho C_p \frac{\partial T}{\partial t} = \nabla.(\mathrm{K}\nabla T) + Q_{gen} \tag{4.9}$$

Where T is the temperature, K is the thermal conductivity, and ρ and C_p are the density and specific heat, respectively. During battery operation, two heat sources are included in this model: (1) Entropy heat (Reaction heat, reversible), (2) Joule heat (Due to the internal resistance of the cell components such as electrodes and separator, irreversible).

The heat generated equation during the electrochemical reaction is given by the following equation:

$$Q_{gen} = \left(\phi_s - \phi_l - U_i + T\frac{\partial U_i}{\partial T}\right)J \tag{4.10}$$

where $(\phi_s - \phi_l - U_i)J$ represents the joule heat, and $T\frac{\partial U_i}{\partial T}J$ represents the entropy heat.

4.2.2 Component 2: Lumped Parameter Model

The individual components (electrodes, current collectors, and separator) inside the battery are very thin. Indeed, the thickness of each component is of the order of dozens of micrometers. Lumped parameter models have been previously used to represent equivalent material properties for all the layers such as thermal conductivity and specific heat coefficient (Lin et al., 2012, 2014; Oh & Epureanu, 2016). Additionally, it is safe to assume a uniform heat generation throughout the battery cell (Bernardi et al., 1985; S. C. Chen et al., 2005; Kim et al., 2013).

4.2.2.1 Thermal Model

A schematic diagram of the pouch cell sandwiched between two plates is shown in Figure 4.3. The lumped parameter model assumes a 1D thermal behavior of the pouch cell with a conduction boundary condition when in contact with the plates as illustrated in Figure 4.3. Left. Moreover, a convection boundary condition is considered on the top and the bottom of the plates. The liquid electrolytes generally show limited mobility since they are trapped in the porous structure of the electrodes and the separator. Hence, the contribution of convection inside the battery can be neglected.

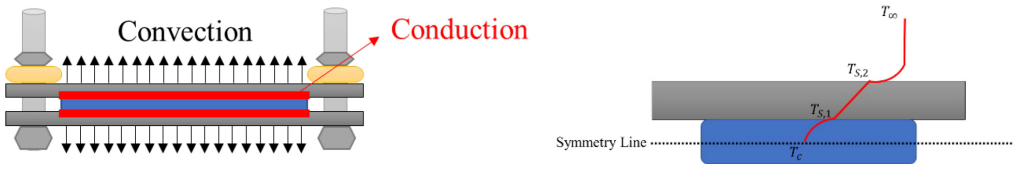

Figure 4.3: Schematic representation of the pouch cell inside the fixture.

The transient one-dimensional conductive heat transfer equation is as follows:

$$C_{cell}\,\frac{dT_C(t)}{dt} = Q_{gen}(t) - 2 * \frac{\mathrm{K}_{cell}\,A_{cell}}{\frac{L_{cell}}{2}}\left(T_C(t) - T_{S,1}(t)\right) \tag{4.11}$$

where C_{cell} is the cell heat capacity, $Q_{gen}(t)$ is the heat generated in the battery, T_C is the core temperature of the battery, $T_{S,1}(t)$ is the surface temperature of the battery, K, A, and L refer to the thermal conductivity, area, and length, respectively. At the top boundary of the plate, convection is considered. The convective heat transfer can be expressed as:

$$Q_{conv} = h_{air}\,A_{plate}(T_{S,2}(t) - T_\infty) \tag{4.12}$$

Moreover, the two-state approximation of the 1D thermal model can be defined from Figure 4.3:

$$\frac{\mathrm{K}_{cell}\,A_{cell}}{\frac{L_{cell}}{2}}\left(T_C(t) - T_{S,1}(t)\right) = \frac{\mathrm{K}_{plate}\,A_{plate}}{\frac{L_{plate}}{2}}\left(T_{S,1}(t) - \frac{T_{S,1}(t) + T_{S,2}(t)}{2}\right) \tag{4.13}$$

$$\frac{\mathrm{K}_{cell}\, A_{cell}}{\frac{L_{cell}}{2}}\left(T_C(t) - T_{S,1}(t)\right) = h_{air}\, A_{plate}\left(T_{S,2}(t) - T_\infty\right) \tag{4.14}$$

where $T_{S,2}(t)$ is the surface temperature of the plate, $T_{\infty,ambient}$ is the ambient temperature, and h_{air} is the air convection coefficient.

4.2.2.2 Spring Model

A spring model was used to depict the battery cell behavior in the fixture. Figure 4.4 illustrates the behavior of the cell at constrained conditions. Two equivalent stiffness elements are modeled: the equivalent stiffness s_{Total} representing the cell and the plate, and the equivalent stiffness s_{Rod} representing the rod. These equivalent stiffness values refer to the relationship between the force applied on the fixture and the displacement of the fixture along the vertical axis. A linear model was used to predict the dependence of the force on the displacement (Branch A):

$$F_{Branch\ A} = s_{Total}\left(\delta_{Total}^{c,\%}\right) \tag{4.15}$$

where s_{Total} is the linear equivalent stiffnesses, and $\delta_{Total}^{c,\%}$ represents the constrained displacement of the battery and plates. The superscript c represents the constrained displacement conditions. There are four rods connected in parallel at the four edges of the plate. The total force in Branch B can be described by:

$$F_{Branch\ B} = 4 * s_{Rod}\left(\Delta_{bolt} + \delta_b^{f,\%} - \delta_{Total}^{c,\%}\right) \tag{4.16}$$

where Δ_{bolt} is the displacement in the rod due to the tightening of the bolt and $\delta_b^{f,\%}$ is the free unconstrained displacement of the battery. The total measured displacement in this case would be:

$$\delta^{EXP,\%} = \delta_b^{f,\%} - \delta_{Total}^{c,\%} + \delta_0^c \tag{4.17}$$

where δ_0^c is the initial displacement.

At the equilibrium state, the plate and the battery cell are compressed, while the rods are stretched from their original size. Indeed, two force acts on the spring model, a compressive force acts on the plates and the battery cell and a tensile force acts on the rods. At mechanical equilibrium, the resultant force is zero. Hence, both forces are equal. Using the balance of forces gives:

$$F_{Branch\ A} = F_{Branch\ B} \tag{4.18}$$

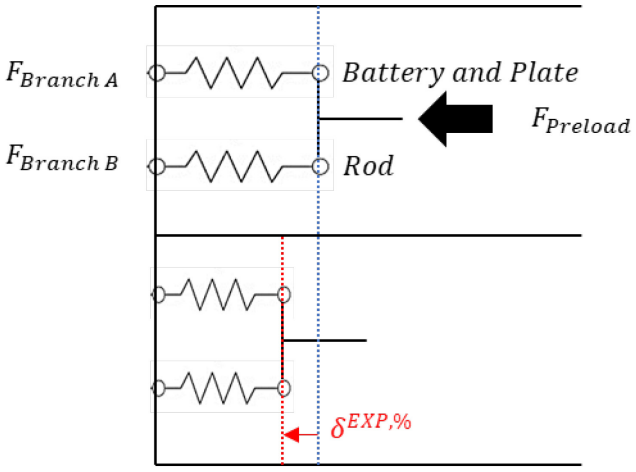

Figure 4.4: Spring Model.

4.2.2.3 Multi-Physics Coupling

The proposed lumped parameter model considers the total swelling ΔL_{Total} in the battery cell is mainly due to: (1) swelling due to the thermal expansion $\Delta L_{Thermal}$, (2) Swelling due to Li-ion intercalation process $\Delta L_{Intercalation}$.

The model assumes lumped parameters, and uniform heat generation (Joule and entropy heat) across the cell. Hence, the temperature distribution in the battery follows a parabolic shape (See Figure 4.3. Right). First, the thermal swelling normal to the battery cell can be expressed as:

$$\Delta L_{Thermal} = \alpha \int_0^{L_{Cell}} (T(x) - T_S)dx \tag{4.19}$$

Where ΔL_T is the thermal swelling (due to the cell heating/cooling), L_{Cell} is the original thickness of the cell, α is the lumped coefficient of thermal expansion, and T is the temperature. The subscript S denotes the surface initial state. By integrating the Equation 4.17 and assuming that the temperature distribution across the cell can be modelled using a parabola we get:

$$\Delta L_{Thermal}(t) = \alpha * L_{Cell} * \left(\frac{2}{3}\left(T_C(t) - T_S(t)\right) + \left(T_S(t) - T_{Ref}\right)\right) \tag{4.20}$$

where t is the time. Two main terms are shown in the equation: The first term $\frac{2}{3}\left(T_C(t) - T_S(t)\right)$ represents the thermal swelling based on the temperature in the cell, while the second term $\left(T_S(t) - T_{Ref}\right)$ represents the swelling due to the difference in temperature between the surface of the cell and the reference temperature.

Swelling due to the Li-ion intercalation process occurs during charging and discharging in the battery cell. During charging, the anode expands and the cathode shrinks. The equation is given by:

$$\Delta L_{Intercalation} = \xi . SOC \tag{4.21}$$

Where ξ is the SOC coefficient, and SOC is the state-of-charge of the cell.

The thermal (Section 4.3.2.1) and the spring model (Section 4.3.2.2) are linked using free swelling in the battery cell given as:

$$\delta_b^{f,\%} = \Delta L_{Thermal} + \Delta L_{Intercalation} = \alpha_{Battery} L_{Battery} \left(\frac{2}{3}\left(T_c - T_{s,1}\right) + \left(T_{s,1} - T_{Ref}\right)\right) + \xi . SOC \tag{4.22}$$

Where $\delta_{Diffusion}^{\%}$ the displacement of the battery due to lithiation, and the second term is the displacement of the battery due to thermal expansion.

4.2.2.4 Parameterization

The responses and predictors are shown in Table 4.1. Four parameters are estimated from the lumped parameter model: (1) Heat capacity of the cell C_{Cell}, (2) heat transfer coefficient of air h_{air}, (3) thermal expansion coefficient of the cell, (4) Soc coefficient for the Li-ion intercalation. The responses parameters were estimated in MATLAB using the experimental temperatures $T_{s,1}^{actual}$ and $T_{s,2}^{actual}$, the force F^{actual}, and displacement $\delta_{Total}^{EXP,\%,actual}$ from the charge and discharge experiment by minimizing:

$$\min \sum_{i} \left(T_{s,1}^{actual} - T_{s,1}^{predicted}\right)^2 + \left(T_{s,2}^{actual} - T_{s,2}^{predicted}\right)^2 + \left(F^{actual} - F^{predicted}\right)^2 + \left(\delta_{Total}^{EXP,\%,actual} - \delta_{Total}^{EXP,\%,predicted}\right)^2 \quad (4.23)$$

Table 4.1: Responses and predictors for the optimization problem.

Responses	**Symbol**
Battery Surface Temperature	$T_{s,1}$
Plate Surface Temperature	$T_{s,2}$
Total Force	F
Constrained Displacement of the Fixture	$\delta^{EXP,\%}$
Predictors	**Symbol**
Heat Generated from the battery	Q_{gen}
Diffusion Swelling	$\delta_{Diffusion}^{\%}$
Time	Time
Ambient Temperature	T_{Amb}

4.2.3 Component 3: Solid Mechanics Model

For component 3, structural mechanics is used to predict the stresses in the model. The 2D schematic representation of the mechanical model is shown in Figure 4.5. The part modeled is highlighted using a dotted box on the left figure. The negative current collector, anode electrode, separator, cathode electrode and positive current collector are shown in different colors. Two sets of boundary conditions take place in the model: (1) Internal and (2) external. During the battery

production process, the electrodes and the current collectors are bonded together using a paste. Then, the separator is tightly wrapped around the electrodes. Hence, a union was created between the cathode electrodes and the positive current collector, and the anode electrode and the negative current collector. The union assumes that the electrodes and the corresponding current collector as continuous media. Moreover, two internal boundaries were assigned in the model that might result in a relative slip. A contact boundary condition was assigned between the cathode electrode and the separator, and between the anode electrode and the separator. Two external boundary conditions were also assigned. A symmetric boundary condition was placed on the left and bottom side of the model. The right-side boundaries were free boundaries. Lastly, a distributed normal load was applied at the top boundary due to the tightening of the bolts.

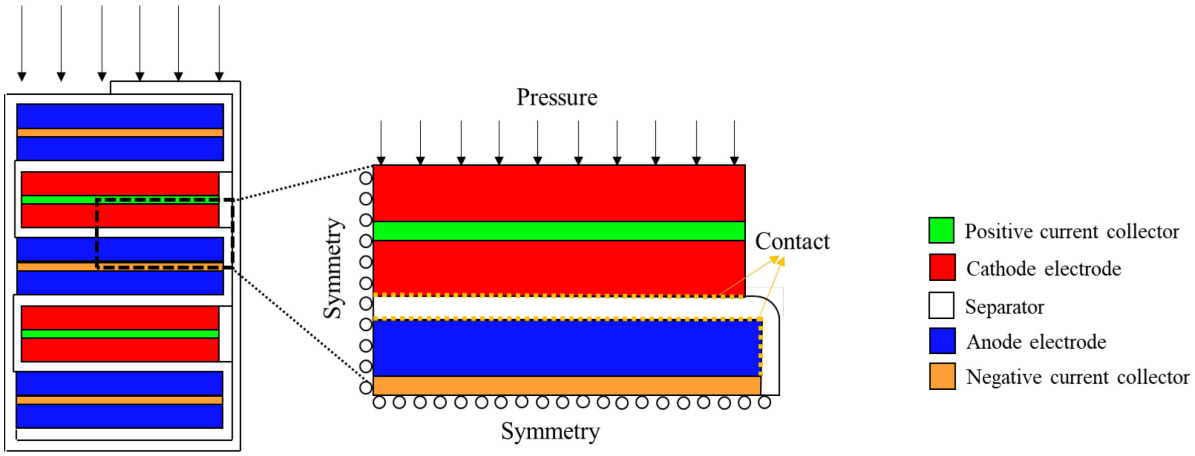

Figure 4.5: 2D Mechanical Model Schematic representation.

Remark 1. The 2D mechanical model was built with an extra cathode on the top. If a full cell was modeled without the extra cathode, the cathode would form an asymmetric beam which tends to deflect upwards splitting from the separator under the Li-ion intercalation induced stress.

To solve this problem, one needs to add an additional cathode into the 2D mechanical model to counteract the bending.

The constitutive equations use mechanical strains ε_{ij}^{me}, thermal strain ε_{ij}^{T} (Shi et al., 2011) and intercalation induced strain ε_{ij}^{D} (Xiao et al., 2010; Zhang et al., 2007) to predict the stress in the battery components. The full equation can be written as:

$$\begin{aligned} \varepsilon_{ij} &= \varepsilon_{ij}^{me} + \varepsilon_{ij}^{T} + \varepsilon_{ij}^{D} \\ &= \frac{1}{E^{v}}\Big((1+\nu^{v})\sigma_{ij} + \nu\sigma_{kk}\delta_{ij}\Big) + \alpha_{ij}\Delta T\delta_{ij} + \frac{1}{3}\Delta c\Omega\delta_{ij} \end{aligned} \tag{4.24}$$

where E^{v} is the Young's modulus, ν^{v} is the Poisson's ratio, σ_{ij} is the stress tensor, and δ_{ij} is the Kronecker delta, α_{ij}^{v} is the thermal expansion coefficient, ΔT is the change in temperature from a reference value, Δc is the change in the diffusion species concentration from a reference (stress-free) value, and Ω^{i} is the partial molar volume (Zhang et al., 2007, 2008). The partial molar volume can be calculated using (Zhang et al., 2007):

$$\Omega^{i} = \frac{3\varepsilon}{\Delta y\, C_{s,Max}} \tag{4.25}$$

Remark 2. Equation 4.24 only considers the elastic deformation and does not consider plastic deformation. This is a safe assumption in this case since we are only simulating one full charge in the 1D battery model. However, if simulating a significant number of charge and discharge cycles, accumulated fatigue or creep needs to be considered in the mechanical equations.

4.3 Experimental Methods

This section provided detailed information about the battery cell used and its components material. Moreover, a description of the experiments for the parameter identification and validation is provided. A first experiment was conducted to measure the total load, displacement, and temperatures when the battery is packed. The experiment was used to fit the 1D electrochemical

model and the lumped parameter model parameters. A second experiment was conducted to find the equivalent stiffness of the battery and plate in the fixture. A third experiment was conducted to find the Young's Modulus of the rod used in the fixture.

4.3.1 Material

A pouch type (110 mm × 74 mm × ≈4 mm height × width × depth) 3.5 Ah Li-ion battery cell was used in this study. The pouch cells used a double-sided mesophase graphite (SMG) anode with a copper current collector, and double-sided $LiNi_{0.6}Co_{0.2}Mn_{0.2}O_2$ (NMC 622) cathode with an aluminum current collector. 1 M $LiPF_6$ in ethylene carbonate (EC): ethyl methyl carbonate (EMC) (3:7 by volume) were used as electrolyte, and a wet processed polyethylene (PE) single layer separator was used between the electrodes.

The PE separator was 12 μm in thickness fabricated through co-extrusion blowing process. The separator porosity was 43% with a crystallinity range between 60% and 80%. The tensile strength in the machine direction (MD) was 235 MPa while in the transversal direction (TD) 225 MPa. The PE separator properties are shown in Table 4.2.

Table 4.2: PE separator properties.

Thickness (μm)	Crystallinity (%)	Porosity (%)	Heat Shrinkage MD (% @105C,8hr)	Heat Shrinkage TD (% @105C,8hr)	Tensile Strength MD (MPa)	Tensile Strength TD (MPa)
12	60-80	43	4.0	4.5	235	225

4.3.2 Charge and Discharge Cycling (4C)

A first experiment was carried out to capture the load, displacement, and temperature variation during charge and discharge of the battery. Initially, the batteries were charged at a constant current- constant voltage (CC-CV) to 3.6 volts at 0.5 C, with a 5% current cutoff (0.0875

A) and allowed to rest for 1 hours for thermal equilibrium. A fixture was used to hold the battery shown in Figure 4.6. The fixture was composed of two steel plates (125 mm length × 99 mm width × 12.7 mm thickness) with non-conductive tape on the edges, connected using four threaded rods (9.5 mm diameter), lock-nuts were used on the bottom side of the rods, and hex nuts were used at the top. The battery was placed in the middle of the bottom plate, sandwiched between both plates. One thermocouple was attached to the middle surface of the battery to measure the battery's surface temperature. Another thermocouple was installed on the middle surface of the top plate to measure the temperature variation due to the heat exchanged with the battery. A third thermocouple was placed next to the fixture to measure the ambient temperature. On the top side, four compression load cells manufactured by Omega (Model: LC9150-500-1K) were placed between the plate and the hex nut. The load cells were connected to a junction box to sum up the signal. A high precision displacement sensor by Keyence (LK-G10) was placed 10 mm above the fixture and was used to measure the fixture expansion on the top plate. The whole setup was placed inside a thermal chamber where the temperature was set to 20 degrees Celsius. Finally, a 1 N.m torque was applied on the top hex nuts.

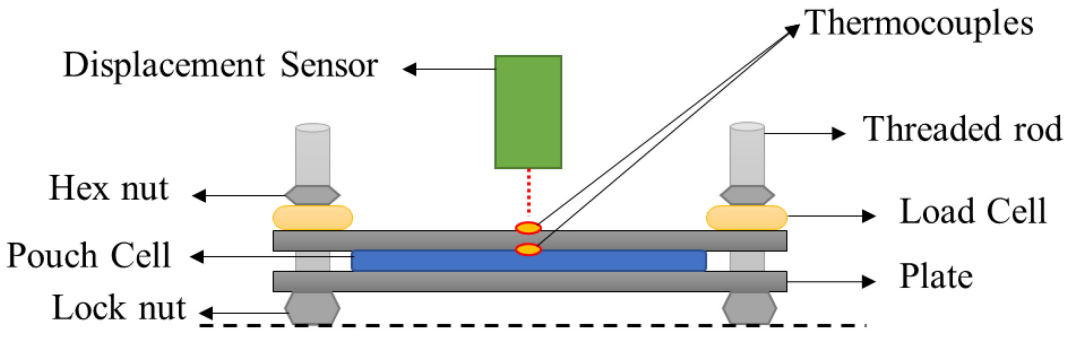

Figure 4.6: Fixture used for the charge and discharge.

A constant current constant voltage (CC-CV) charge or discharge was used in this study. The CC-CV consists of two main parts: (1) A constant current step is applied to the battery until it reaches the specified voltage known as the cutoff voltage, (2) A constant voltage step when the battery reaches the cutoff voltage until the current reaches a specified threshold value. The battery was first discharged to 3.0 volts with a current cutoff of 0.0875 A (5%) and allowed to rest for 1 hour. This was followed by a full charge to 4.2 volts and then a discharge to 3.0 volts. The charging process consisted of two steps: charging of the battery at a constant current (14 A) equivalent to 4C, until reaching a voltage of 4.2 volts, and then holding the cell voltage at 4.2 volts until the current drops to 5% (0.7 A) of its initial value. For the discharge process, it also consisted of two steps: the battery was discharged at a constant current (1.75 A) until reaching 3 volts, then holding the cell voltage at 3.0 volts until the current drops to 5% (0.0875 A) of its initial value. The total force, displacement, three temperatures (Battery surface, plate surface, and ambient temperature), voltage and current were all measured during the experiment.

4.3.3 Equivalent Stiffness Experiment

In a second experiment, the force and displacement at several torques were measured to find the equivalent spring constant of the battery and the plate. The fixture shown previously in Figure 4.6 was used for the experiment. The battery was initially charged to 3.6 volts and placed between the plates. No thermocouples were used in this experiment. Four compression load cells manufactured by Omega (Model: LC9150-500-1K) were placed between the plate and the hex nut. The torque was increased by an increment of 0.2 N.m between 0 and 1 N.m, and by an increment of 0.1 N.m between 1 and 1.2 N.m. The total force and the displacement were recorded at each increment.

4.3.4 Rod Stiffness Experiment

In a third experiment, the force and turn angle were recorded to find the stiffness coefficient of the rod. A rod was placed vertically with a lock-nut at the bottom. An Omega load cell was placed between the lock-nut and a hex nut. A torque was applied with an initial increment of 0.5 N.m, with a following torque 0.8 N.m, 1.2 N.m, and 1.6 N.m. The turn angle and force were recorded at each increment.

4.3.5 Effective Material Properties

The battery cell is filled with liquid electrolyte which rests in the porous structure of the electrodes and the separator. To account for this influence, the porosity needs to be considered in the materials properties for the electrodes and the separator. Indeed, the components' porosity needs to be taken into consideration by introducing effective material properties. In this study, an effective thermal expansion coefficient and Young's modulus were used.

The expansion of the components and the electrolytes cannot be neglected when modeling thermal expansion. The effective thermal expansion of the electrodes and the separator was estimated by the rule of mixture similar to composite systems as:

$$\alpha_{eff} = \sum_{i} \alpha_i V_i \tag{4.26}$$

Where α_i and V_i are the thermal expansion coefficient and volume fraction of the ith phase, respectively. Similarly, the effective Young's modulus of a composite consisting of particles dispersed in a matrix falls between an upper and lower bound (Rethwisch, 2010). The expressions are defined as:

$$E_{eff,upper} = E_m V_m + E_p V_p \tag{4.27}$$

$$E_{eff,lower} = \frac{E_m E_p}{E_p V_m + E_m V_p} \tag{4.28}$$

where E_m and E_p are the Young's modulus of the matrix and particles, respectively, and V_m and V_p are the volume fraction of the matrix and particles, respectively.

4.3.6 Models Parameters

The structural, electrochemical, thermal, and mechanical parameters used in COMSOL are listed in Table 4.3. The use of '*' next to a value indicates an effective parameter.

Table 4.3: COMSOL Model parameters for component 1 and component 3.

Model Parameters	**Units**	**Cu**	**Anode**	**Separator**	**Cathode**	**Al**	**Electrolyte**
Dimensional Parameters							
Thickness	μm	10	71	12	48.5	20	
Length	mm	71	71		69	69	
Electrochemical Parameters							
Density	kg/m^3		2230	900	4750		1210
Active Volume Fraction			0.5686		0.6698		
Porosity			0.37454	0.43	0.26322		
Stochiometric maximum concentration	mol/m^3		49000		31507		
Diffusion coefficient	$m^2 s^{-1}$		1.4523×10^{-13}		5×10^{-13}		
Particle Radius	μm		4		5		
Partial molar volume	m^3/mol		4.4196×10^{-5}		2.8418×10^{-5}		
Thermal Parameters							
Thermal expansion coefficient	$1/K$	17×10^{-6}	6.03×10^{-6}*	82.5×10^{-6}*	9.62×10^{-6}*	23×10^{-6}	
Mechanical Parameters							
Young's Modulus	GPa	110	6.82*	0.645*	6.69*	70	
Poisson's ratio		0.35	0.3	0.45	0.3	0.33	0.25

This section covers the model parameters used in the LPM. The thickness and area for the aluminum plate were 12.7 mm and 0.023 m^2, respectively. The thickness and area of the cell were 3.906 mm and 0.008 m^2. The thermal conductivity of the cell depends on the direction of the heat flow (S. C. Chen et al., 2005; Drake et al., 2014). Indeed, the heat transfer is anisotropic in the cell due to the presence of current collector which present very high thermal diffusivity. The through-plane thermal conductivity can be expressed as (Drake et al., 2014):

$$\frac{\sum t_v}{\mathrm{K}_{eq}} = \sum \frac{t_v}{\mathrm{K}_v} \tag{4.29}$$

Where K_v is the thermal conductivity of the material layer, and t_v is the thickness of the material layer. This is only applicable when the battery components are thermally stacked in series in the cell. The equivalent thermal conductivity of the cell was found to be 0.633 $\frac{W}{mK}$. The thermal conductivity and thermal expansion coefficient of the plate were provided by the manufacturer as 167 $\frac{W}{mK}$, and 25.2×10^{-6} $\frac{1}{K}$, respectively.

4.4 Results & Discussion

4.4.1 Charge and Discharge Cycling Data

The charging and discharging load/temperature measurements are presented in this section. The battery was initially charged to 3.6 volts with a constant current density equivalent to a charge rate of 0.5C, then the voltage was held at 3.6 volts with a current drop to 5% of its initial value. Figure 4.7. Top shows the voltage and current at the start of discharge from 3.6 volts. The data consists of three parts which all use a constant current – constant voltage charge or discharge. The first part of the curve shows a CC-CV 0.5C discharge from 3.6 to 3 volts (0-2178 seconds). The

second part is a CC-CV 4C charge from 3 to 4.2 volts (2178-3407 seconds), and the third part is a CC-CV 0.5C discharge from 4.2 to 3 volts (3407-9470 seconds).

Figure 4.7 (Bottom Left) shows the load and displacement vs time overlayed on the voltage curves to allow for easier interpretation. Starting with the displacement figure (See Figure 4.7. Bottom Left), the discharge between 3.6 volts and 3 volts decreases the displacement measured at the top of the fixture. The displacement sensor was set reset to zero after tightening the bolts. The rapid decrease during discharge is followed by a faint decrease during the voltage hold. During fast-charging at 4C, the sharp increase in the voltage instigates a sharp increase in the displacement. During charging the lithium-ions travel from the cathode to the anode, which causes a shrinkage in the cathode electrode and an expansion of the anode electrode. The voltage-hold after fast charging results in a small increase in the displacement followed by a decrease. This is due to the initial increase in the temperature during charge followed by a decrease during the hold period. The maximum displacement reached during fast charging was 45.8 μm. During discharge the displacement decreases sharply between 4.2 volts and 3.7 volts, followed by a faint decrease between 3.7 and 3.6 and another sharp decrease between 3.6 and 3 volts. The load follows exactly the same trend described for the displacement curve. After tightening the bolts with a 1 N.m torque, the initial load applied on the battery was 1314 Newton. The load decreases during the discharge from 1314 to 983 Newton, then increases significantly during charge to a maximum of 2333 Newton followed by a small decrease to 2213 during the charge hold period. During the discharge to 3 volts, the load decrease to 1070 Newton.

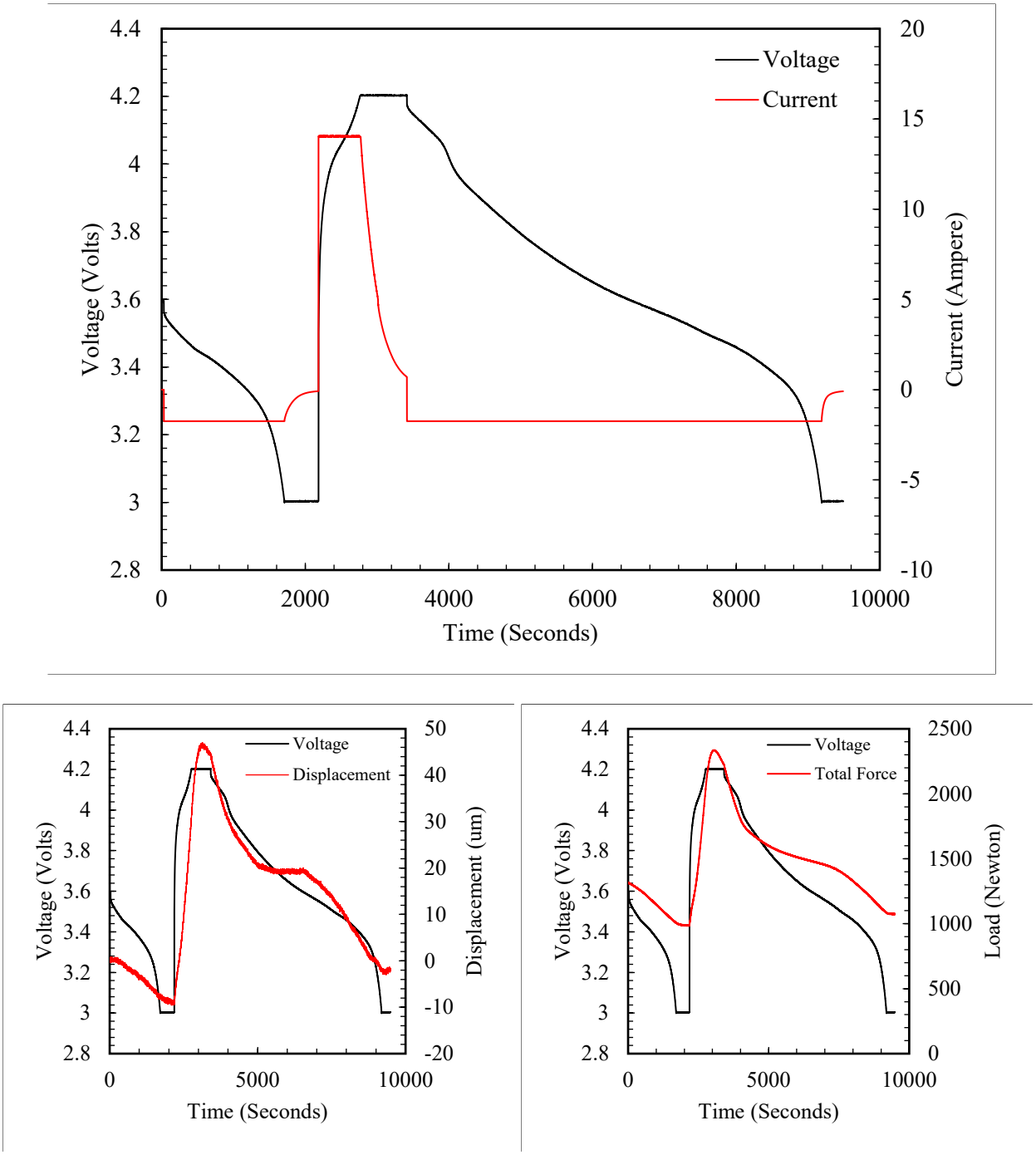

Figure 4.7: (Top) Voltage and current versus time, (Bottom Left) Voltage & Displacement versus Time, (Bottom Right) Voltage & Load versus Time.

Figure 4.8 presents the battery surface and plate temperatures measured during the fast-charging period. The battery surface and plate temperatures were around 20 degrees throughout the

experiment. However, during the fast charging at 4C, we notice an increase in the battery and plate temperature. The battery and plate surface temperature reaches a maximum 21 and 20.8 degrees Celsius, respectively. During the hold period, the temperature starts to decrease.

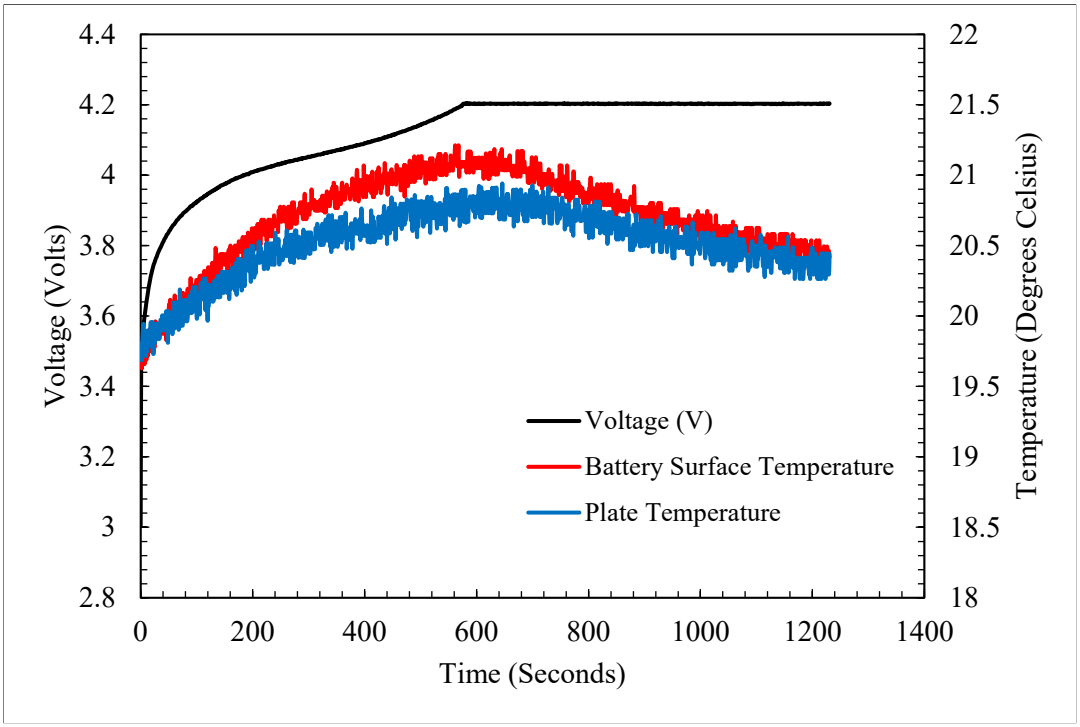

Figure 4.8: Battery surface temperature and plate temperature versus time.

4.4.2 LPM Model Fitting and Results

Several parameters are needed to solve the lumped parameter model. The first parameter is the equivalent spring coefficient of the plate and the battery. The force measurement experiment provides the load applied and the displacement at specific torques applied. The equivalent stiffness was fitted on the force and displacement experimental data shown in Figure 4.9. Left. The spring constant for the battery was found to be $\boldsymbol{s_{Total}} = 9.0892 \times 10^{6}\ N.m^{-1}$. Additionally, the rod spring constant was found fitted on the force and displacement experimental data shown in Figure 4.9. Right. The turn angle was used to calculate the displacement in the rod using the pitch.

However, the spring constant found was for the distance between the two nuts. The Young's modulus can then be found using:

$$S_{Rod} = \frac{EA}{L} \tag{4.30}$$

Using the Young's Modulus, we can then calculate the rod spring constant for the actual distance in the fixture. S_{Rod} was found to be 12×10^6 N. m^{-1}.

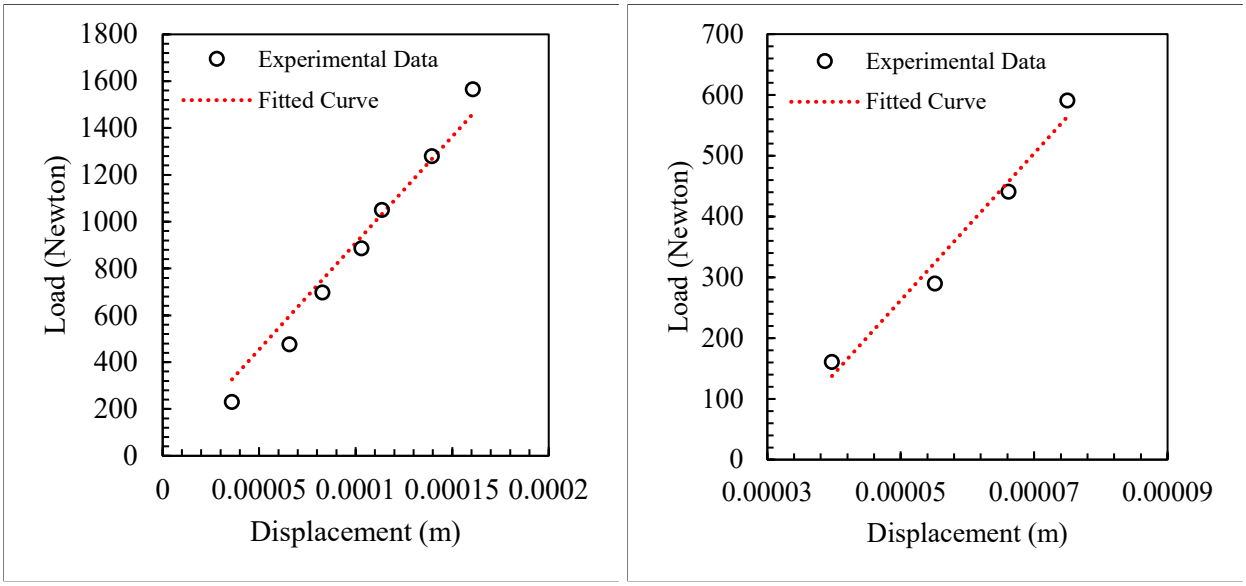

Figure 4.9: Force versus Displacement for the (Left) equivalent battery and plate spring constant and (Right) rod spring constant.

The entropy and joule heat were extracted from the 1D electrochemical model and used as an input in the lumped parameter model. Equation 4.15 and 4.16 were used to find the initial value of Δ_{bolt} at the initial force. A non-linear regression was performed using a least-square approximation (lsqcurvefit in MATLAB) to identify the thermal and SOC coefficient model parameters. The estimated parameters are shown in Table 4.4. The estimated parameters are in the same order of magnitude with the values found in the literature. The heat capacity was found to be 403 J/K. The

thermal expansion coefficient of the cell was 0.003 $1/K$, which falls in the range found in (Oh & Epureanu, 2016).

Table 4.4: Optimized parameters.

Parameters	Optimization Solution
C_{Cell}	403.69
h_{air}	112.30
α_{Cell}	0.003
ξ	0.0001

The results of the parameters are shown in Figure 4.10. The battery surface temperature, the plate surface temperature, and the fixture displacement are all predicted accurately. The lumped parameter overestimates the force at the end of charging.

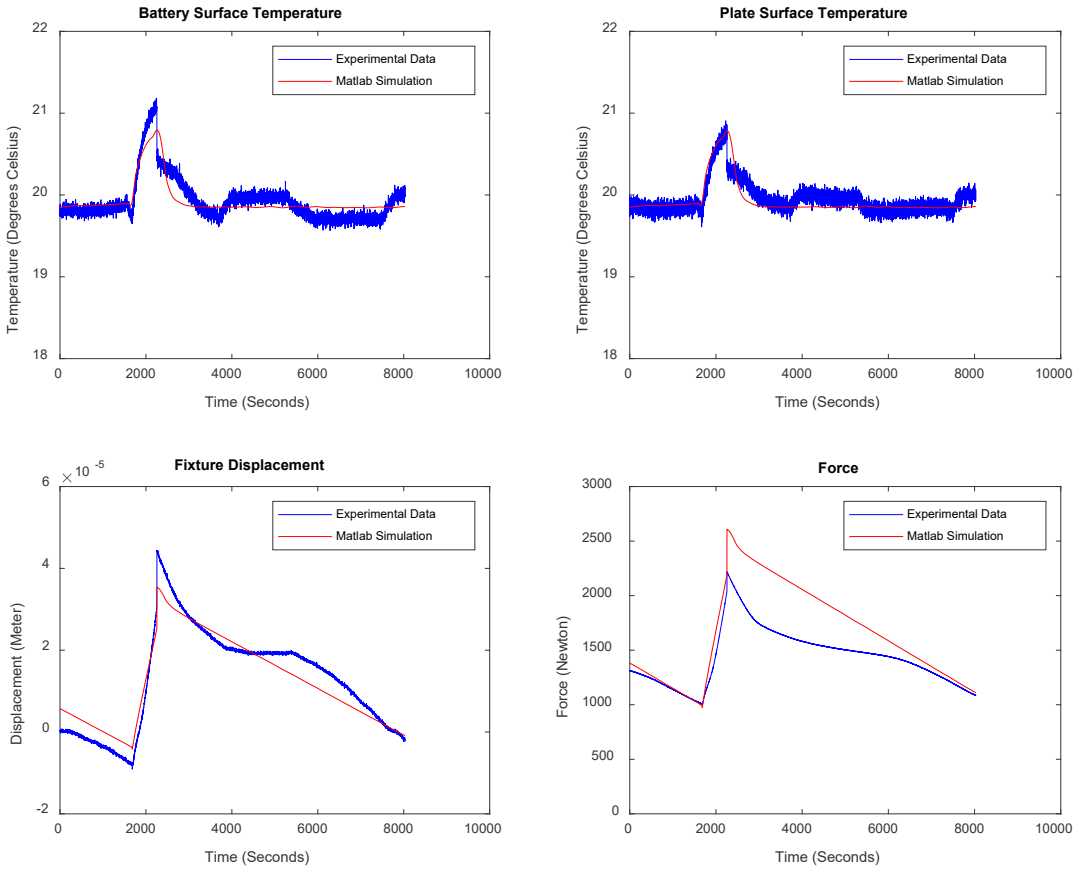

Figure 4.10: Fitted Curves vs Experimental Data.

To check for the accuracy of the LPM and evaluate the model's predictions, the root mean square error (RMSE) was used as a fit performance metric for accuracy. RMSE is expressed as:

$$RMSE = \sqrt{\frac{\sum_{i=1}^{n}\left(y_i^{actual} - y_i^{predicted}\right)^2}{N}} \tag{4.31}$$

where y_i^{actual} is the experimental value, $y_i^{predicted}$ is the value predicted in the model, and N is the total number of data points. Additionally, the RMSE range and average are also shown to check for the model's accuracy. The results are shown in Table 4.5. Based on the results, the maximum error was found for the Force which was 573 for the force. The RMSE values for the temperatures

and displacement show the strength of the model in predicting the data accurately. However, the RMSE value for the force is on the high side due to the poor fit during the discharge period.

Table 4.5: Maximum error and RMSE between the experimental and predicted curves.

Parameters	**Maximum Error**	**RMSE**	**RMSE/ Range**	**RMSE/ Average**
$T_{s,1}$	0.52	0.1326	0.1262	0.0066
$T_{s,2}$	0.63	0.1190	0.1142	0.0060
$\delta^{EXP,\%}$	$6.06e-6$	$3.6379e-6$	0.0969	0.2962
F	573	297	0.1921	0.1800

4.4.3 Stress Prediction in the Separator

The temperature and lithium concentration were used as a direct input from component 1 and component 2. The top boundary load used corresponds to the experimental total load measured. The stresses in the middle of the separator were computed. Figure 4.11 presents the first principal stress contours in the middle of the separator. All other components were greyed out. The maximum first principal stress was found to be 70 MPa after a full charge at 4C. The principal stress was aligned in the machine direction with the machine direction. The high stress is mainly due to the expansion of the anode electrode which induces a tensile load on the separator since the separator is wrapped around it. Moreover, the top boundary load causes a compression in the separator.

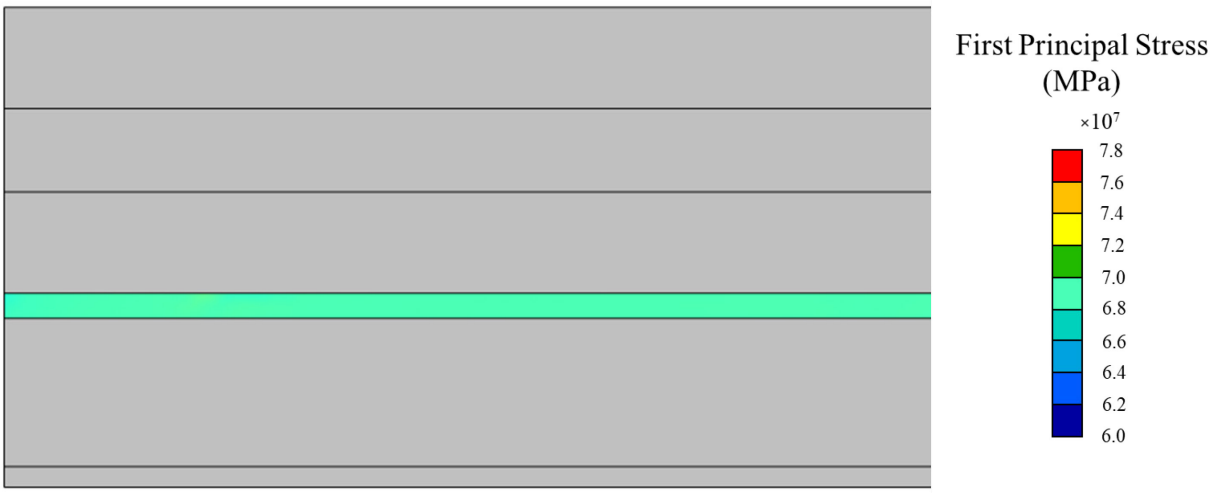

Figure 4.11: COMSOL Model components displacement.

4.5 Damage Validation

Creep and fatigue tests were conducted on the pristine separators to check the effect of the hold period during constant voltage, and the effect of charge and discharge cycling on the polyethylene separator. Strip-shaped uniaxial tensile specimens were prepared according to ASTM D882. The samples were cut from a pristine separator roll as strip-shaped using a razor. The samples main axis was aligned in the machine direction with a 100 mm length and 10 mm width. The gage length was chosen to be 50 mm. The creep and fatigue experiments were conducted using an ElectroPuls E1000. Foamy jaws were used to hold the specimen from each side.

The creep testing was conducted to several engineering stresses specified. First a ramp loading of 0.1 MPa/s was used to reach the specified stress. The initial specified stress used was 70 MPa which was the first principal stress calculated from COMSOL solid mechanics component. The stress was in COMSOL found after a CC-CV charge from 3 volts to 4.2 volts. Four other stresses were also used: 50, 60, 80, and 90 MPa, with 50 and 60 falling below the reference stress, and 80 and 90 falling above the reference stress. All tests were left until reach a maximum

displacement of 60 mm, with 50 MPa the only exception. The test was stopped after 6 days. The creep test results are presented in Figure 4.12. The samples reached 60 mm under an applied loading of 90 and 80 MPa after 4 and 5.5 hours respectively. Both tests stayed in the primary stage of creep with a rapid increase in the deformation. The time increases significantly to 37 hours when the load becomes 70 MPa. Moreover, the time increases to 68 hours at 80 MPa. At 90 MPa the experiment was stopped after 6 days reaching 48.45 mm displacement. The creep tests at 50, 60, and 70 MPa reached the secondary creep stage where the creep was practically constant. The creep results show that a loading stress of 70, 80 or 90 MPa can cause significant damage in the separator. Even at a lower load such as 50 MPa, the polymeric separator deforms by 20 mm under just 4 hours. The results suggest that tensile creep is a major factor contributing to the mechanical degradation of the battery separator. Moreover, the separator is subjected to a compressive load due to the torque applied at the bolt in our case mimicking the module assembly. The fast-charging condition subjects the separator to high stress conditions causing a tensile stress in the machine and a compressive stress along the thickness direction affecting the mechanical integrity of the separator.

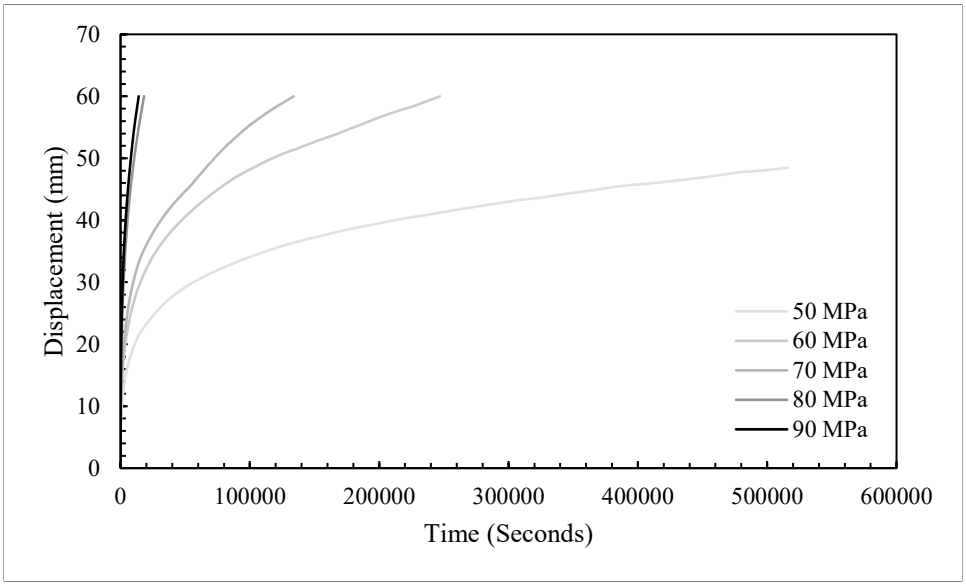

Figure 4.12: Displacement as a function of time for the creep tests.

Fatigue testing was also conducted on the pristine separator. The testing mimicked the CC-CV charging and discharging of the battery for 68 cycles. Each cycle consisted of: (1) an increasing linear ramp representing the charge duration, (2) a stress hold representing the voltage hold period, and (3) a linear decreasing ramp representing the discharge duration. The initial ramp was applied between 0 to 70 MPa for a total time of 13 minutes to simulate the fast-charging condition. The first principal stresses calculated from COMSOL was also used in this experiment. Then, the stress was held at 70 MPa for 10 minutes to simulate the constant voltage with the current drop. Finally, a linear decreasing ramp was applied between 70 and 0 MPa for a total time of 90 minutes. The test ran continuously until reaching 68 cycles. The fatigue tests are presented in Figure 4.13. The displacement as a function of time is shown on the left while the maximum position in each cycle is shown on the right. The displacement vs time shows a strong linear increase in the displacement during the charging period, followed by a faint increase in the displacement during the hold period at 70 MPa. This is followed by a decrease in the displacement during unloading. From the

maximum position in each cycle (See Figure 4.13. Right), the displacement increases significantly during the first 10 cycles, followed by a linear increase for the rest of the cycles. The fatigue test is an extreme simulation of the separator deforming under charge and discharge cycles. The separator deforms significantly during the preliminary cycles, the deforms slowly after that. The results suggest that an initial load of 70 MPa can cause a significant damage in the separator. Additionally, continuous battery charge and discharge cycling causes the damage to accumulate due to the increase in the deformation in the separator.

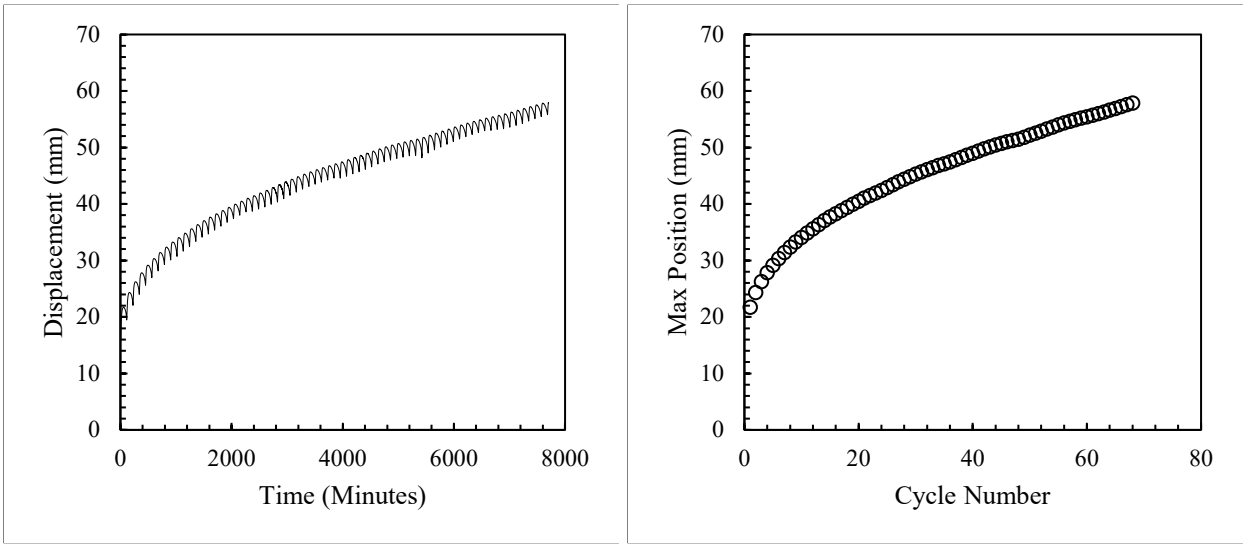

Figure 4.13: Fatigue tests simulating the charge and discharge cycles.

4.6 Summary

In the past decade, lithium-ion batteries have become the most used technology choice for EVs. As more car manufacturers switch to EVs, the time required to recharge batteries is one of the main challenges that needs to be addressed. Fast-charging protocols have been developed to reduce charging time however, the strong currents can cause capacity and power decrease. Moreover, continuous fast charging can cause heat accumulation in the battery causing thermal degradation and raising safety concerns. In EVs, lithium-ion batteries are combined in series or

parallel to create modules, and then many modules are connected to create a pack. The basic building block is thus a cell whether it's a rectangular pouch cell or a wound configuration such as cylindrical cells. This paper presents a Multiphysics framework to capture the thermal and mechanical stresses arising in the battery cell under fast charging conditions. The model considers two main inputs: the charge rate and the boundary load. The Multi-physics model predicts the heat generation in the battery, the total load applied on the battery cell, the battery displacement, and the cell temperature. Additionally, the model predicts the stresses inside the battery, specifically the separator. A non-linear regression was performed using a least-square approximation to identify the LPM parameters. The model results showed that the temperature did not increase significantly nevertheless, the first principal stress in the separator was around 70 MPa aligned with the machine direction. Furthermore, creep and fatigue were conducted at 70 MPa to check for the separator deformation damage. The results showed that a 70 MPa in the machine direction can cause significant damage in the separator. The high creep sensitivity and creep deformation correlate with the development of significant damage in the separator. Further investigation should explore modifications of the solid mechanics model to account for the effect of creep and fatigue during the battery charge and discharge cycling. The constitutive equations use the mechanical, thermal, and intercalation strains to predict the stresses in the separator. The separator is subjected to creep caused due to the voltage hold period and to fatigue due to the repeated charging cycles. Both of these mechanisms should be included in the solid mechanics constitutive equation.

Chapter 5 Conclusion and Future Work

5.1 Summary of Research Achievements

To address the gap in knowledge regarding the separator degradation during charge and discharge cycles, the objectives of this dissertation are summarized as follows:

(1) *Understand the mechanisms behind the chemical and mechanical degradation of separators under charging and discharging cycles, specifically fast charging conditions.*

To meet this objective, an experimental plan was implemented to charge and discharge lithium-ion batteries at different number of cycles. We attempted fast charging at 4C and discharging at 0.5C for 400, 800, and 1600 cycles. Afterwards, the batteries were disassembled, and the separator was removed. We conducted FTIR and XPS on the pristine separator and the 1600 cycled separators to check for any chemical degradation that might have occurred from the electrochemical reaction. The XPS and FTIR analysis of the separator surfaces did not reveal the presence of chemical degradation. XPS analysis showed that the cycled separator contained P, F, O that are potentially electrolyte salt and solvents decomposition products. FTIR showed several IR absorption bands of lithium hexafluorophosphate ($LiPF_6$). Additionally, we conducted SEM on the pristine separator, the 800, and 1600 cycled separator to check for mechanical degradation. The SEM micrographs of the separator showed a layer of deposits from the anode side while small, scattered deposits were seen on the cathode side. SEM also showed that the high number of charging cycles cause damage to accumulate in the form of pore closure resulting from compression creep along the thickness, and fiber fracture and through thickness crack formation

resulting from tensile creep along the machine direction. The fast-charging conditions can affect the separators' mechanical integrity. The separator is subjected to a compressive force (along the thickness) from the battery pack assembly, accompanied by tensile force (along the machine direction) resulting from the electrodes' expansion. Consequently, the separator is subjected to creep caused by the hold period and the repeated charging cycles.

(2) Identify the effect of cell operations including the number of cycles on the separator degradation.

The first objective helped in identifying the main mechanisms of degradation which is creep-fatigue. To address the second objective, we conducted tensile loading, biaxial loading tests, and creep and fatigue tests. The mechanical properties of the cycled separators presented a decrease in the toughness and ductility with increased number of charging cycles. Additionally, under punch tests the cycled separators presented different behaviors between the cathode and anode side of the separator. Samples punched from the anode side showed a higher overall average fracture than the specimens punched from the cathode side. Moreover, the separator showed high creep sensitivity and creep deformation correlating with the development of significant damage in the separator.

(3) *Provide designers with predictive tools that allow them to improve the battery life efficiency and safety.*

To meet objective 3, the mechanical and anisotropic behavior of a single-layer polyethylene battery separator was investigated under uniaxial tension and punch tests. A finite element model was proposed that combines the anisotropic continuum damage theory and the non-Gaussian network to account for the viscohyperelastic behavior. The capability of the proposed model to predict the anisotropic mechanical behavior up to fracture for two different types of

battery separators was assessed using the experiments generated on the polyethylene single layer battery separator (Wet-processed), and the experiments reported in the literature on PP/PE/PP trilayer (Dry-processed). The model was able to predict the mechanical behavior and failure of the separators under different loading conditions. In other works, a Multiphysics framework was developed to capture the thermal and mechanical stresses arising in the battery cell under fast charging conditions. The model showed a good agreement with the experimental results. Additionally, the stress distribution inside the battery pouch cell was predicted. Creep and fatigue tests were conducted on the pristine separator to generate deformation damage. The results show that the predicted stress from the Multiphysics model can cause significant damage in the separator after continuous fast charge and discharge cycling.

5.2 Intellectual Merit and Broader Impacts

The proposed work will expand the knowledge about the degradation mechanisms during charge and discharge cycles. Findings from chapter 3 helped in identifying the main mechanisms of degradation during fast charge and discharge cycles. Additionally, by understanding the degradation mechanisms occurring in the separator, we can develop models that integrate those mechanisms to enhance the design of batteries. Hence, this work will help in increasing the public scientific knowledge regarding this topic.

Intellectual Merit: The lithium-ion battery is the main energy storage device used in electronics (laptops, smartphones), biomedical, and automotive (Electrical Vehicles) fields. Researchers are trying to optimize the cost, safety, performance, and life of lithium-ion batteries. Accurately characterizing the degradation mechanisms occurring under different charge-discharge cycles will help in finding solutions in estimating the remaining useful battery life and provide engineers with tools to allow them to improve the battery safety and prolong its life cycle. The

findings from this research will help manufacturers understand the effect of number of cycles and charging rate on the separator degradation and provide designers with a model to allow them to improve the battery life span and safety.

Broader Impact: Improving the battery life span and safety will have a direct impact on the development of lithium-ion batteries. The life span of lithium-ion batterie in electrical vehicles is around 10-20 years. Moreover, the safety of lithium-ion batteries is a main concern as there is risk of combustion. Therefore, accurately modeling the mechanical stresses inside the battery cell is essential and can decrease the safety concerns over lithium-ion batteries.

5.3 Future Work

Although this dissertation helped in bridging the gap between the degradation mechanisms in the separator under charge and discharge cycles and providing tools to model the stresses in the separator, there are several improvements that should be considered. First, chapter 2 provides a constitutive model to predict the damage in the separator. Validating the capability of the proposed model to predict the effects of aging in the separators under charge and discharge cycles is one of the key improvements. Separators showed a decrease in toughness and ductility with increased number of cycles. The continuum damage mechanics model implements two damage parameters that can be modified at different number of cycles. This can allow for the modeling of fracture at different number of cycles. In chapter 4, a Multiphysics model was developed to predict the stresses in the separator under different charging rates, and pack assembly loads. The constitutive equations in the solid mechanics model can be modified and improved to account for the effect of creep and fatigue during the battery charge and discharge cycling.

Appendices

Appendix A

Jacobian Matrix Derivation

This section provides details on the derivation of the Jacobian matrix introduced in Equation 2.29. First, the constitutive equation for the stress rate (Equation 2.7), backstress rate (Equation 2.13), and damage rate (Equation 2.17) were derived with respect to the stress, backstress, and damage vectors (Equation 2.22). For instance, the stress rate was derived with respect to the stress, damage, and backstress vectors as follows:

$$\frac{\partial \dot{\sigma}_{ij}}{\partial \sigma_{kl}}, \frac{\partial \dot{\sigma}_{ij}}{\partial \varphi_{kl}}, \frac{\partial \dot{\sigma}_{ij}}{\partial b_{kl}} \tag{A.1}$$

Similar approach was used to determine the derivation of the backstress rate and the damage rate as follows:

$$\frac{\partial \dot{b}_{ij}}{\partial \sigma_{kl}}, \frac{\partial \dot{b}_{ij}}{\partial \varphi_{kl}}, \frac{\partial \dot{b}_{ij}}{\partial b_{kl}} \tag{A.2}$$

$$\frac{\partial \dot{\varphi}_{ij}}{\partial \sigma_{kl}}, \frac{\partial \dot{\varphi}_{ij}}{\partial \varphi_{kl}}, \frac{\partial \dot{\varphi}_{ij}}{\partial b_{kl}} \tag{A.3}$$

These partial derivations are needed for deriving the residual vectors (Equation 2.24 to 2.26). The Jacobian matrix is determined by deriving the stress, backstress and damage residuals with respect to the stress, backstress, and damage vectors. The full Jacobian matrix shown in Equation 2.29 becomes:

$$\left[\frac{\partial[\boldsymbol{R}]}{\partial[\boldsymbol{X}]}\right]_{18\times 18}=\begin{bmatrix}\frac{\partial R_{\sigma_{11}}}{\partial \sigma_{11}} & \cdots & \frac{\partial R_{\sigma_{11}}}{\partial \sigma_{13}} & \frac{\partial R_{\sigma_{11}}}{\partial \varphi_{11}} & \cdots & \frac{\partial R_{\sigma_{11}}}{\partial \varphi_{13}} & \frac{\partial R_{\sigma_{11}}}{\partial b_{11}} & \cdots & \frac{\partial R_{\sigma_{11}}}{\partial b_{13}} \\ \vdots & \ddots & \vdots & \vdots & \ddots & \vdots & \vdots & \ddots & \vdots \\ \frac{\partial R_{\sigma_{13}}}{\partial \sigma_{11}} & \cdots & \frac{\partial R_{\sigma_{13}}}{\partial \sigma_{13}} & \frac{\partial R_{\sigma_{13}}}{\partial \varphi_{11}} & \cdots & \frac{\partial R_{\sigma_{13}}}{\partial \varphi_{13}} & \frac{\partial R_{\sigma_{13}}}{\partial b_{11}} & \cdots & \frac{\partial R_{\sigma_{13}}}{\partial b_{13}} \\ \frac{\partial R_{\varphi_{11}}}{\partial \sigma_{11}} & \cdots & \frac{\partial R_{\varphi_{11}}}{\partial \sigma_{13}} & \frac{\partial R_{\varphi_{11}}}{\partial \varphi_{11}} & \cdots & \frac{\partial R_{\varphi_{11}}}{\partial \varphi_{13}} & \frac{\partial R_{\varphi_{11}}}{\partial b_{11}} & \cdots & \frac{\partial R_{\varphi_{11}}}{\partial b_{13}} \\ \vdots & \ddots & \vdots & \vdots & \ddots & \vdots & \vdots & \ddots & \vdots \\ \frac{\partial R_{\varphi_{13}}}{\partial \sigma_{11}} & \cdots & \frac{\partial R_{\varphi_{13}}}{\partial \sigma_{13}} & \frac{\partial R_{\varphi_{13}}}{\partial \varphi_{11}} & \cdots & \frac{\partial R_{\varphi_{13}}}{\partial \varphi_{13}} & \frac{\partial R_{\varphi_{13}}}{\partial b_{11}} & \cdots & \frac{\partial R_{\varphi_{13}}}{\partial b_{13}} \\ \frac{\partial R_{b_{11}}}{\partial \sigma_{11}} & \cdots & \frac{\partial R_{b_{11}}}{\partial \sigma_{13}} & \frac{\partial R_{b_{11}}}{\partial \varphi_{11}} & \cdots & \frac{\partial R_{b_{11}}}{\partial \varphi_{13}} & \frac{\partial R_{b_{11}}}{\partial b_{11}} & \cdots & \frac{\partial R_{b_{11}}}{\partial b_{13}} \\ \vdots & \ddots & \vdots & \vdots & \ddots & \vdots & \vdots & \ddots & \vdots \\ \frac{\partial R_{b_{13}}}{\partial \sigma_{11}} & \cdots & \frac{\partial R_{b_{13}}}{\partial \sigma_{13}} & \frac{\partial R_{b_{13}}}{\partial \varphi_{11}} & \cdots & \frac{\partial R_{b_{13}}}{\partial \varphi_{13}} & \frac{\partial R_{b_{13}}}{\partial b_{11}} & \cdots & \frac{\partial R_{b_{13}}}{\partial b_{13}} \end{bmatrix} \tag{A.4}$$

The residual stress, backstress, and damage derivatives are given as follows:

$$\frac{\partial R_{\sigma_{ij}}}{\partial \sigma_{kl}}=\begin{cases}\frac{1}{\Delta t}-\frac{\partial \dot{\sigma}_{ij}}{\partial \sigma_{kl}} & if\ i=k\ and\ j=l \\ -\frac{\partial \dot{\sigma}_{ij}}{\partial \sigma_{kl}} & otherwise\end{cases} \qquad \frac{\partial R_{\varphi_{ij}}}{\partial \sigma_{kl}}=-\frac{\partial \dot{\varphi}_{ij}}{\partial \sigma_{kl}} \qquad \frac{\partial R_{b_{ij}}}{\partial \sigma_{kl}}=-\frac{\partial \dot{b}_{ij}}{\partial \sigma_{kl}}$$

$$\frac{\partial R_{\sigma_{ij}}}{\partial \varphi_{kl}}=-\frac{\partial \dot{\sigma}_{ij}}{\partial \varphi_{kl}} \qquad \frac{\partial R_{\varphi_{ij}}}{\partial \varphi_{kl}}=\begin{cases}\frac{1}{\Delta t}-\frac{\partial \dot{\varphi}_{ij}}{\partial \varphi_{kl}} & if\ i=k\ and\ j=l \\ -\frac{\partial \dot{\varphi}_{ij}}{\partial \varphi_{kl}} & otherwise\end{cases} \qquad \frac{\partial R_{b_{ij}}}{\partial \varphi_{kl}}=-\frac{\partial \dot{b}_{ij}}{\partial \varphi_{kl}} \tag{A.5}$$

$$\frac{\partial R_{\sigma_{ij}}}{\partial b_{kl}}=-\frac{\partial \dot{\sigma}_{ij}}{\partial b_{kl}} \qquad \frac{\partial R_{\varphi_{ij}}}{\partial b_{kl}}=-\frac{\partial \dot{\varphi}_{ij}}{\partial b_{kl}} \qquad \frac{\partial R_{b_{ij}}}{\partial b_{kl}}=\begin{cases}\frac{1}{\Delta t}-\frac{\partial \dot{b}_{ij}}{\partial b_{kl}} & if\ i=k\ and\ j=l \\ -\frac{\partial \dot{b}_{ij}}{\partial b_{kl}} & otherwise\end{cases}$$

Appendix B

Implicit Integration Algorithm

This section provides a step-by-step explanation of the implicit integration algorithm implemented in the user-defined material (Figure 2.5). The algorithm uses Newton-Raphson's iterative procedure to correct the state variables guesses (stress, backstress, and damage) at each time increment.

Implicit Integration Algorithm code

Inputs: $\boldsymbol{\sigma}$, $\boldsymbol{b}$, $\boldsymbol{\varphi}$, and $\boldsymbol{F}$.

Returns: $\boldsymbol{\sigma}$, $\mathbb{Q}$.

Step 1. For time increment Δt.

Step 2. Set a convergence tolerance $\delta = 10^{-3}$ for the stress, backstress, and damage residual vectors.

Step 3. For Newton-Raphson iteration k.

Step 4. Initialize guesses for the state variables:

If $k = 1$ *and* $t = 0$

Initial guesses are assigned by the user:

$$\left[X_{ij}\right]^{t+1} = X_{0_{ij}} \tag{B.1}$$

Else if $k = 1$ *and* $t > 0$

Update guesses using previous time step:

$$\left[X_{ij}\right]^{t+1} = \left[X_{ij}\right]^{t} \tag{B.2}$$

Else

Update guesses using Newton-Raphson procedure.

Step 5. Compute the stress rate $\dot{\sigma}_{ij}$ (Equation 2.7), backstress rate $\dot{b}_{ij}$ (Equation 2.13), and damage rate $\dot{\varphi}_{ij}$ (Equation 2.17).

Step 6. Compute the residual vectors of the stress $R_{\sigma_{ij}}$, damage $R_{\varphi_{ij}}$, and backstress $R_{b_{ij}}$ (Equation 2.24-2.26).

Step 7. Check for convergence:

If $|R_{\sigma_{ij}}|$, $|R_{b_{ij}}|$, *and* $|R_{\varphi_{ij}}| > \delta$

a. Compute the rate derivatives (Equation A.1-A.3).

b. Compute the residual vectors derivatives (Equation A.5).

c. Compute the Jacobian matrix (Equation A.4)

d. Update the state variables using the Newton-Raphson procedure (Equation 2.28).

e. Go to step 4.

Else if $|R_{\sigma_{ij}}|$, $|R_{b_{ij}}|$, *and* $|R_{\varphi_{ij}}| < \delta$

Go to step 8.

Step 8. Compute consistent tangent matrix ($\mathbb{Q}$)

Appendix C

Fixture Dimensions

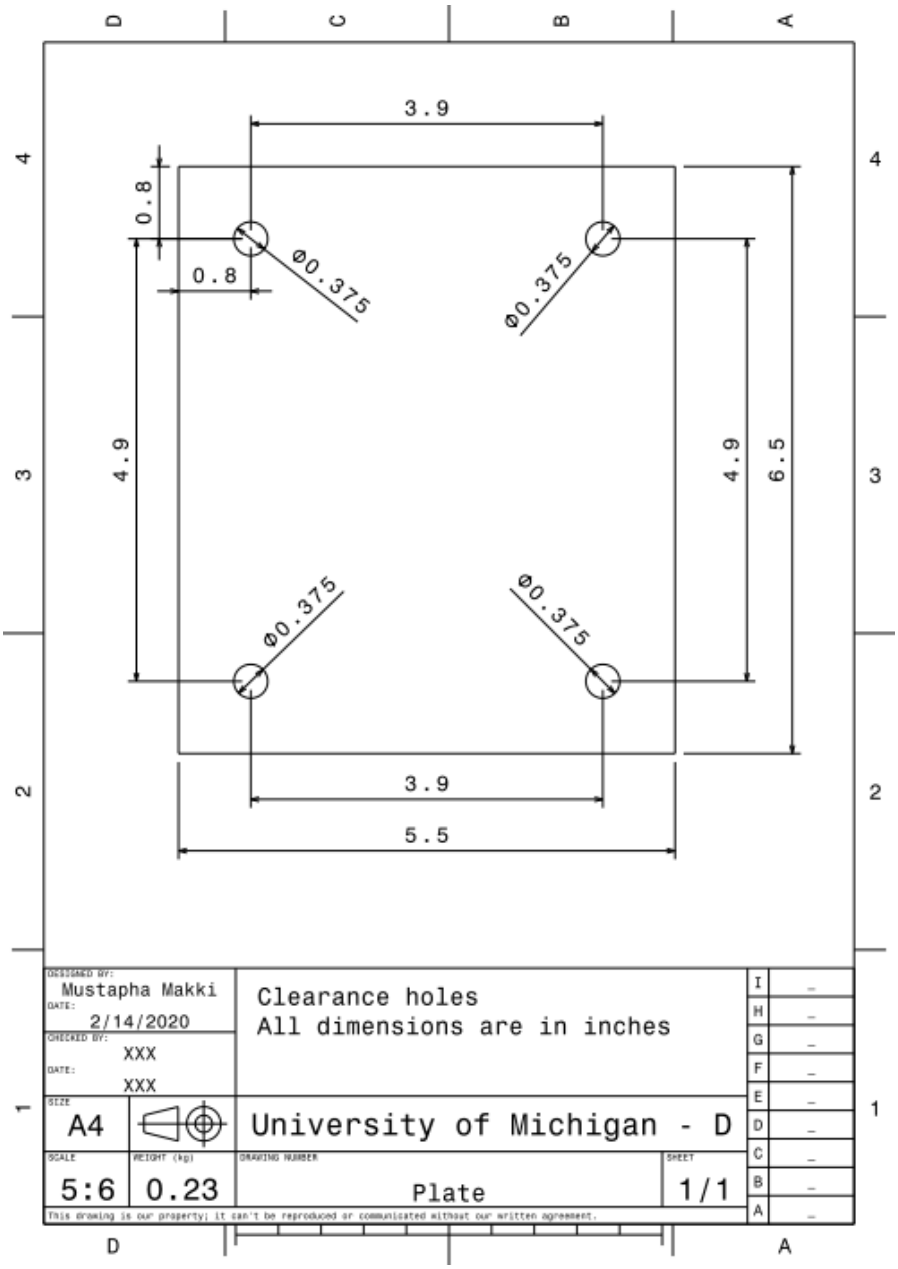

Figure C.1 Drawing sheet for the steel plate.

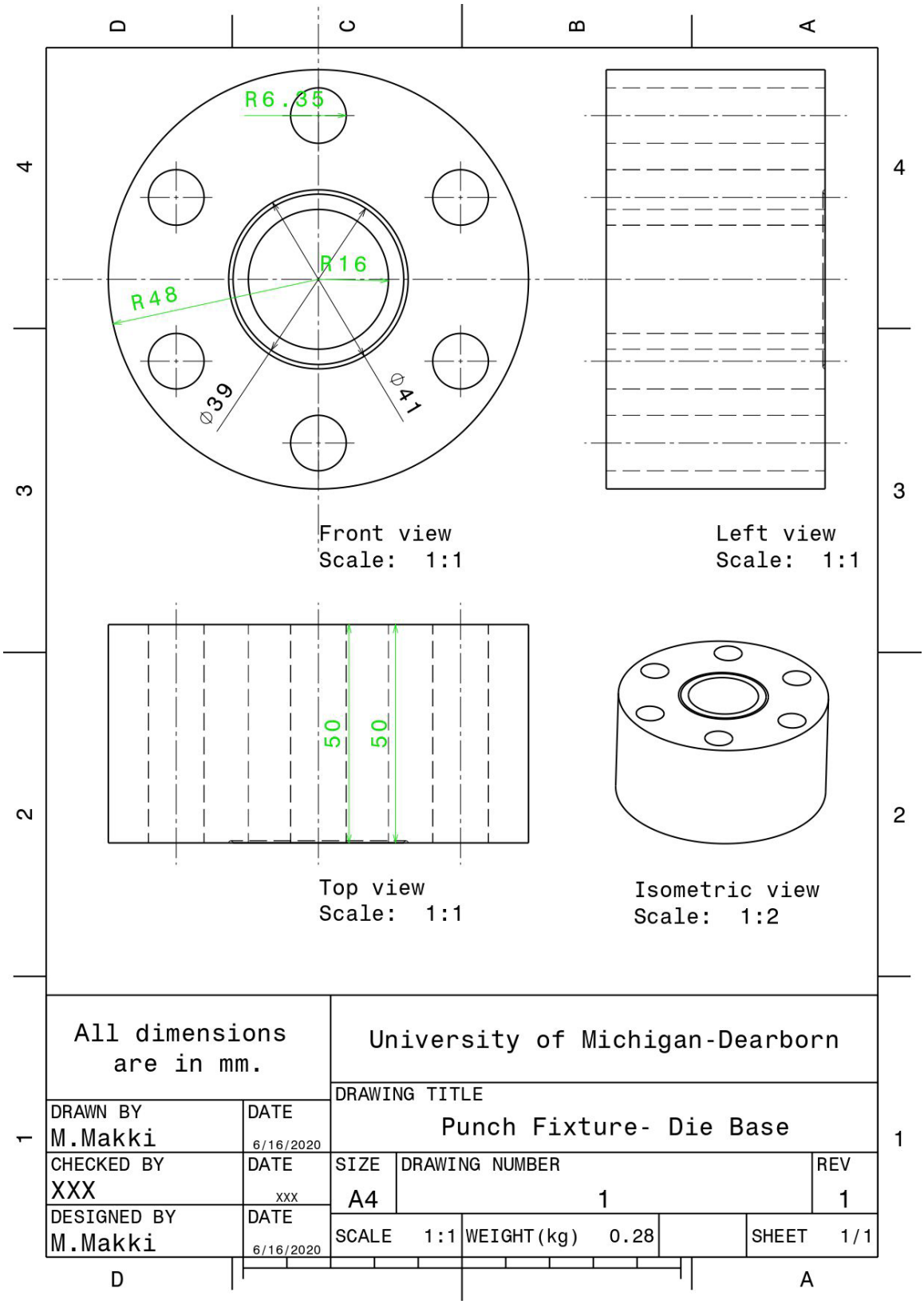

Figure C.2: Drawing sheet for the die.

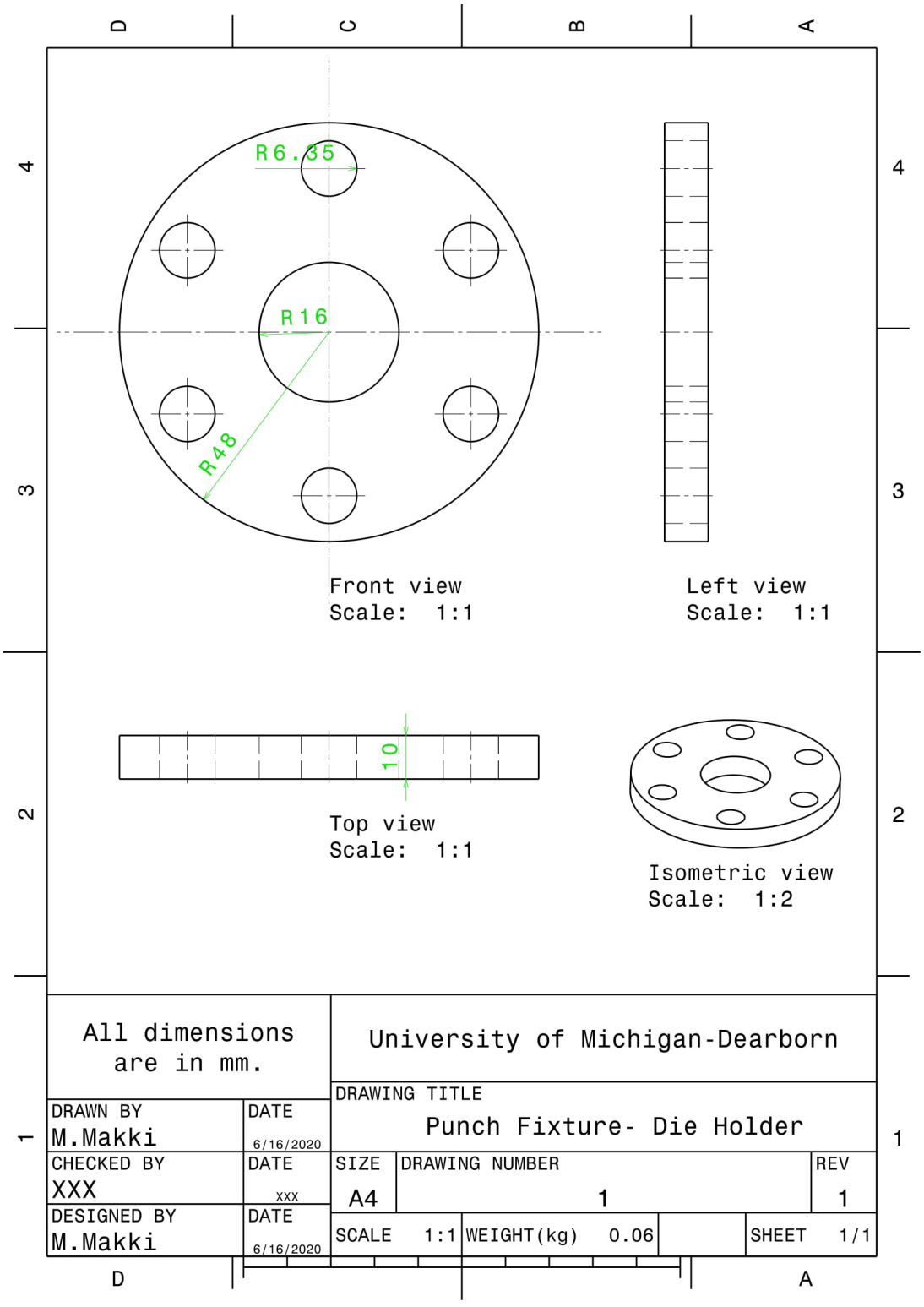

Figure C.3: Drawing sheet for the clamping plate.

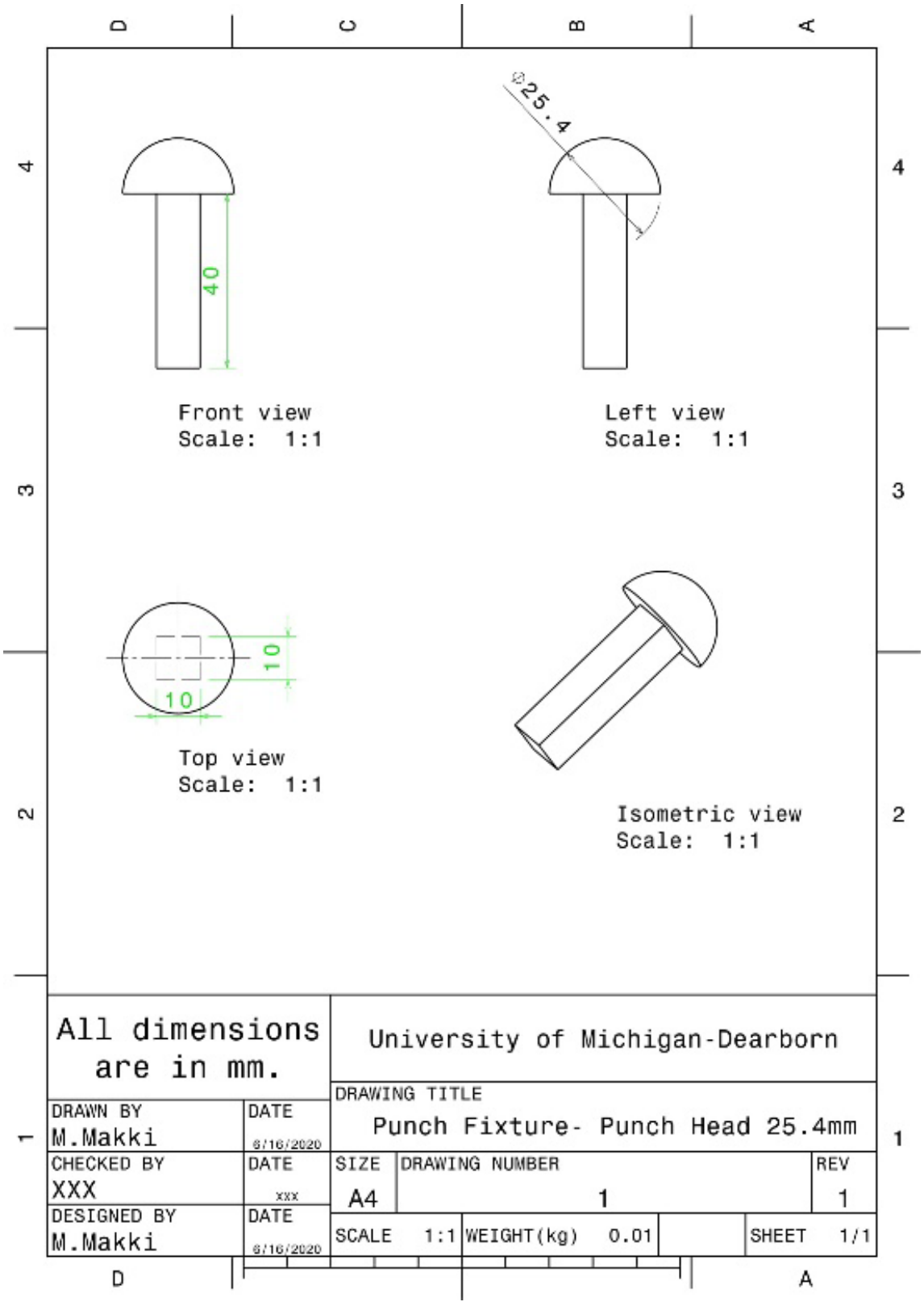

Figure C.4: Drawing sheet for punch head of 25.4 mm diameter.

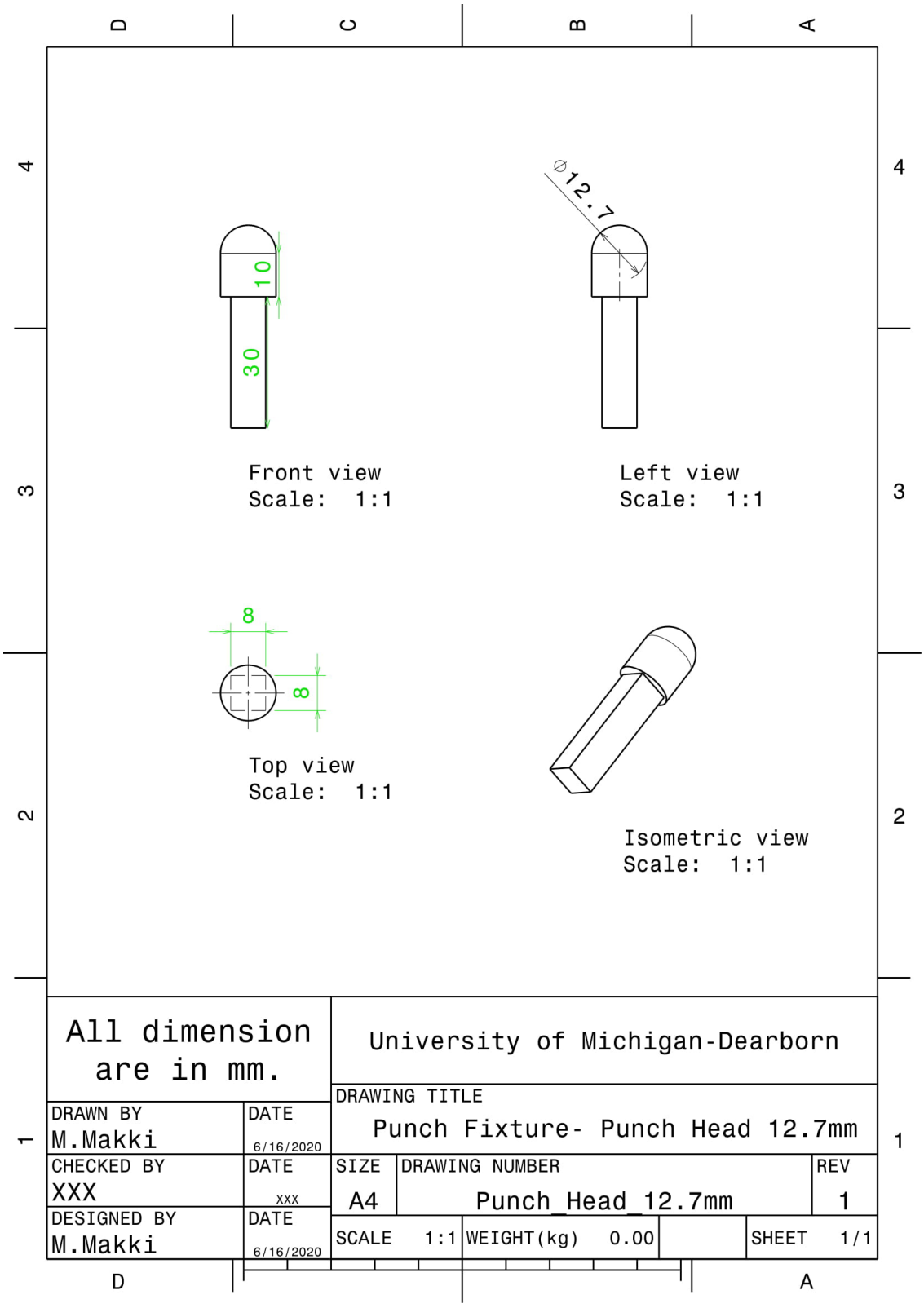

Figure C.5: Drawing sheet for punch head of 12.7 mm diameter.

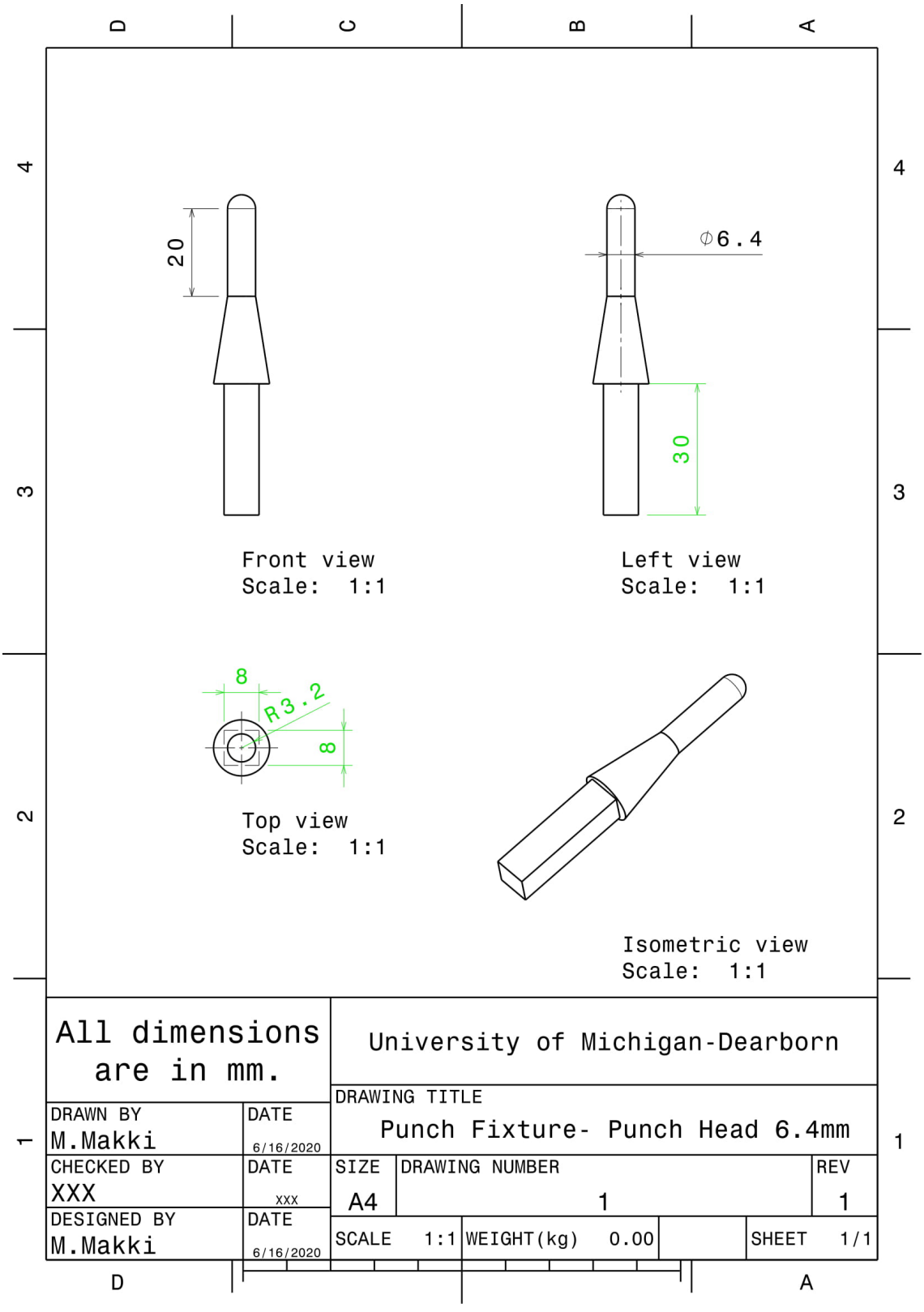

Figure C.6: Drawing sheet for punch head of 6.4 mm diameter.

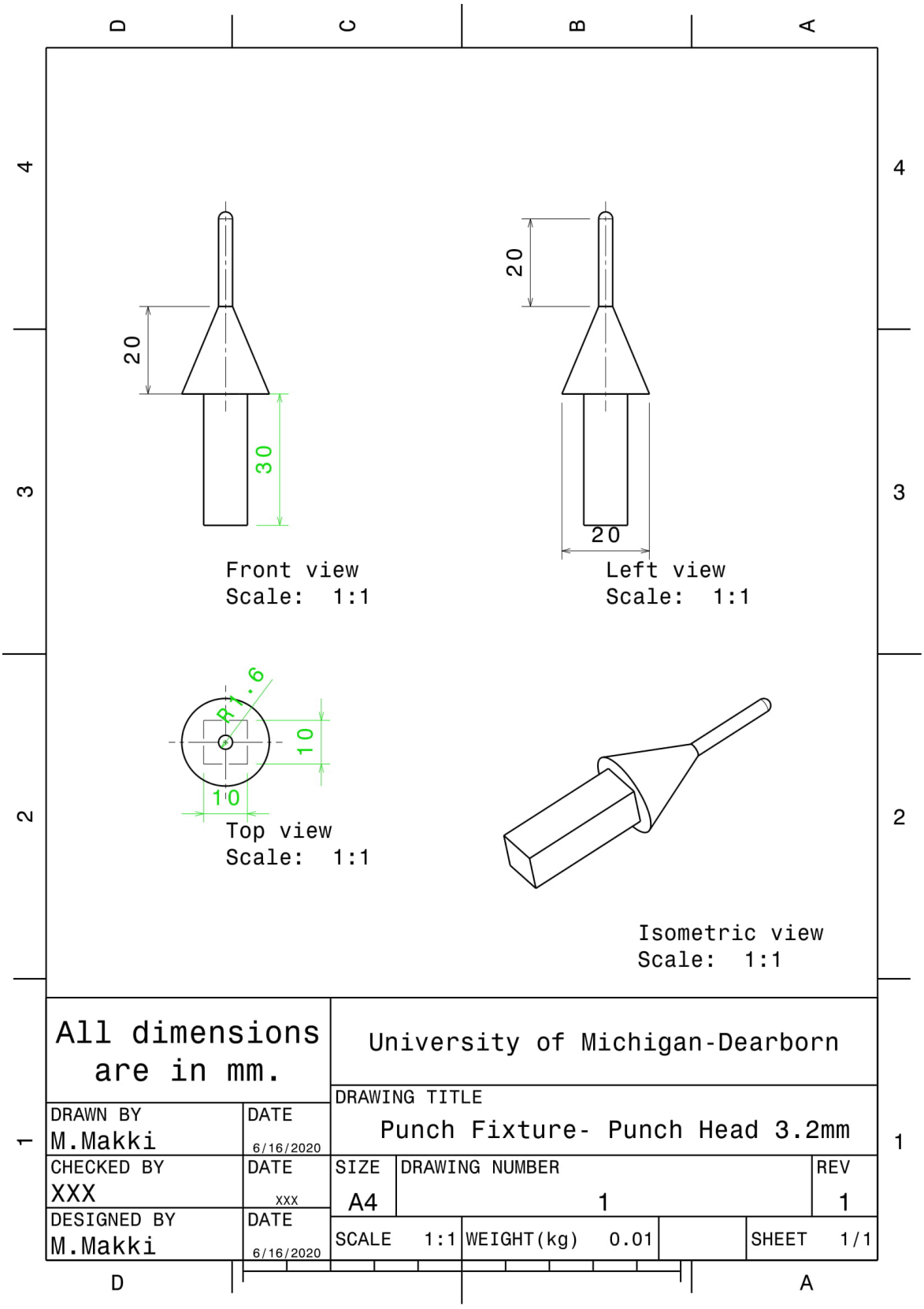

Figure C.7: Drawing sheet for punch head of 3.2 mm diameter.

Bibliography

Abdul-Hameed, H., Messager, T., Ayoub, G., Zaïri, F., Naït-Abdelaziz, M., Qu, Z., Zaïri, F., 2014. A two-phase hyperelastic-viscoplastic constitutive model for semi-crystalline polymers: Application to polyethylene materials with a variable range of crystal fractions. J. Mech. Behav. Biomed. Mater. 37. https://doi.org/10.1016/j.jmbbm.2014.04.016

Abdul-Hameed, H, Messager, T., Zaïri, F., Naït-Abdelaziz, M., 2014. Large-strain viscoelastic–viscoplastic constitutive modeling of semi-crystalline polymers and model identification by deterministic/evolutionary approach. Comput. Mater. Sci. 90, 241–252. https://doi.org/http://dx.doi.org/10.1016/j.commatsci.2014.03.043

Agubra, V., Fergus, J., 2013. Lithium ion battery anode aging mechanisms. Materials (Basel). 6, 1310–1325. https://doi.org/10.3390/ma6041310

Ahzi, S., Makradi, A., Gregory, R. V, Edie, D.D., 2003. Modeling of deformation behavior and strain-induced crystallization in poly(ethylene terephthalate) above the glass transition temperature. Mech. Mater. 35, 1139–1148. https://doi.org/http://dx.doi.org/10.1016/S0167-6636(03)00004-8

Alaoui, C., 2013. Solid-State Thermal Management for. IEEE Trans. Veh. Technol. 62, 98–107.

Amjadi, M., Fatemi, A., 2020. Multiaxial fatigue behavior of thermoplastics including mean stress and notch effects: Experiments and modeling. Int. J. Fatigue 136, 105571. https://doi.org/10.1016/j.ijfatigue.2020.105571

Anand, L., Gurtin, M.E., 2003. A theory of amorphous solids undergoing large deformations, with application to polymeric glasses. Int. J. Solids Struct. 40, 1465–1487. https://doi.org/10.1016/S0020-7683(02)00651-0

Argon, A.S., 1973. A theory for the low-temperature plastic deformation of glassy polymers. Philos. Mag. A J. Theor. Exp. Appl. Phys. 28, 839–865. https://doi.org/10.1080/14786437308220987

Armero, F., Oller, S., 2000. General framework for continuum damage models. II. Integration algorithms, with applications to the numerical simulation of porous metals. Int. J. Solids Struct. 37, 7437–7464. https://doi.org/10.1016/S0020-7683(00)00206-7

Arora, P., Zhang, Z., 2004. Battery separators. Chem. Rev. 104, 4419–4462. https://doi.org/10.1021/cr020738u

Arora, P., Zhang, Z.J., Lakes, S., Carolina, N., 2004. Battery Separators.

Arruda, E.M., Boyce, M.C., 1993. A three-dimensional constitutive model for the large stretch behavior of rubber elastic materials. J. Mech. Phys. Solids 41, 389–412. https://doi.org/http://dx.doi.org/10.1016/0022-5096(93)90013-6

Arruda, E.M., Boyce, M.C., Jayachandran, R., 1995. Effects of strain rate, temperature and thermomechanical coupling on the finite strain deformation of glassy polymers. Mech. Mater. 19, 193–212. https://doi.org/10.1016/0167-6636(94)00034-E

Asaro, R.J., Needleman, A., 1985. Overview no. 42 Texture development and strain hardening in rate dependent polycrystals. Acta Metall. 33, 923–953. https://doi.org/http://dx.doi.org/10.1016/0001-6160(85)90188-9

Aurbach, Doron, Ein-Ely, Y., Zaban, A., 1994. The Surface Chemistry of Lithium Electrodes in Alkyl Carbonate Solutions. J. Electrochem. Soc. 141, L1–L3. https://doi.org/10.1149/1.2054718

Aurbach, D., Weissman, I., Zaban, A., Chusid, O., 1994. Correlation between surface chemistry, morphology, cycling efficiency and interfacial properties of Li electrodes in solutions containing different Li salts. Electrochim. Acta 39, 51–71. https://doi.org/10.1016/0013-4686(94)85010-0

Ayoub, G., Naït-Abdelaziz, M., Zaïri, F., 2014a. Multiaxial fatigue life predictors for rubbers: Application of recent developments to a carbon-filled SBR. Int. J. Fatigue 66, 168–176. https://doi.org/https://doi.org/10.1016/j.ijfatigue.2014.03.026

Ayoub, G., Naït-Abdelaziz, M., Zaïri, F., Gloaguen, J.M., 2010a. Multiaxial fatigue life prediction of rubber-like materials using the continuum damage mechanics approach, in: Procedia Engineering. https://doi.org/10.1016/j.proeng.2010.03.107

Ayoub, G., Naït-Abdelaziz, M., Zaïri, F., Gloaguen, J.M., Charrier, P., 2011a. A continuum damage model for the high-cycle fatigue life prediction of styrene-butadiene rubber under multiaxial loading. Int. J. Solids Struct. 48. https://doi.org/10.1016/j.ijsolstr.2011.04.003

Ayoub, G., Rodriguez, A.K., Mansoor, B., Colin, X., 2020. Modeling the visco-hyperelastic–viscoplastic behavior of photodegraded semi-crystalline low-density polyethylene films. Int. J. Solids Struct. 204–205, 187–198. https://doi.org/https://doi.org/10.1016/j.ijsolstr.2020.08.025

Ayoub, G, Zaïri, F., Fréderix, C., Gloaguen, J.M., Naït-Abdelaziz, M., Seguela, R., Lefebvre, J.M., 2011. Effects of crystal content on the mechanical behaviour of polyethylene under finite strains: Experiments and constitutive modelling. Int. J. Plast. 27, 492–511. https://doi.org/https://doi.org/10.1016/j.ijplas.2010.07.005

Ayoub, G., Zaïri, F., Fréderix, C., Gloaguen, J.M., Naït-Abdelaziz, M., Seguela, R., Lefebvre, J.M., 2011b. Effects of crystal content on the mechanical behaviour of polyethylene under finite strains: Experiments and constitutive modelling. Int. J. Plast. 27, 492–511.

https://doi.org/10.1016/j.ijplas.2010.07.005

Ayoub, G., Zaïri, F., Fréderix, C., Gloaguen, J.M., Naït-Abdelaziz, M., Seguela, R., Lefebvre, J.M., 2010b. Modelling finite deformation stress-strain response during loadingunloading of polyethylene over a wide range of crystallinities, in: Procedia Engineering. https://doi.org/10.1016/j.proeng.2010.03.106

Ayoub, G., Zaïri, F., Naït-Abdelaziz, M., Gloaguen, J.M., 2010c. Modelling large deformation behaviour under loading-unloading of semicrystalline polymers: Application to a high density polyethylene. Int. J. Plast. 26, 329–347. https://doi.org/10.1016/j.ijplas.2009.07.005

Ayoub, G., Zaïri, F., Naït-Abdelaziz, M., Gloaguen, J.M., Kridli, G., 2014b. A visco-hyperelastic damage model for cyclic stress-softening, hysteresis and permanent set in rubber using the network alteration theory. Int. J. Plast. 54, 19–33. https://doi.org/https://doi.org/10.1016/j.ijplas.2013.08.001

Bahrololoumi, A., Morovati, V., Poshtan, E.A., Dargazany, R., 2020. A multi-physics constitutive model to predict hydrolytic aging in quasi-static behaviour of thin cross-linked polymers. Int. J. Plast. 130, 102676. https://doi.org/https://doi.org/10.1016/j.ijplas.2020.102676

Balieu, R., Lauro, F., Bennani, B., Delille, R., Matsumoto, T., Mottola, E., 2013. A fully coupled elastoviscoplastic damage model at finite strains for mineral filled semi-crystalline polymer. Int. J. Plast. 51, 241–270. https://doi.org/http://dx.doi.org/10.1016/j.ijplas.2013.05.002

Bandhauer, T.M., Soc, J.E., Bandhauer, T.M., Garimella, S., Fuller, T.F., 2011. A Critical Review of Thermal Issues in Lithium-Ion Batteries. https://doi.org/10.1149/1.3515880

Bardenhagen, S.G., Stout, M.G., Gray, G.T., 1997. Three-dimensional, finite deformation, viscoplastic constitutive models for polymeric materials. Mech. Mater. 25, 235–253. https://doi.org/http://dx.doi.org/10.1016/S0167-6636(97)00007-0

Barré, A., Deguilhem, B., Grolleau, S., Gérard, M., Suard, F., Riu, D., 2013. A review on lithium-ion battery ageing mechanisms and estimations for automotive applications. J. Power Sources 241, 680–689. https://doi.org/10.1016/j.jpowsour.2013.05.040

Bartczak, Z., Galeski, A., 2010. Plasticity of Semicrystalline Polymers. Macromol. Symp. VO - 294, no. 1.

Ben Hadj Hamouda, H., Laiarinandrasana, L., Piques, R., 2007. Viscoplastic behaviour of a medium density polyethylene (MDPE): Constitutive equations based on double nonlinear deformation model. Int. J. Plast. 23, 1307–1327. https://doi.org/http://dx.doi.org/10.1016/j.ijplas.2006.11.007

Benger, R., Wenzl, H., Beck, H.-P., Jiang, M., Ohms, D., Schaedlich, G., 2009. Electrochemical and thermal modeling of lithium-ion cells for use in HEV or EV application. World Electr. Veh. J. https://doi.org/10.3390/wevj3020342

Bergström, J.S., Boyce, M.C., 1998. Constitutive modeling of the large strain time-dependent

behavior of elastomers. J. Mech. Phys. Solids 46, 931–954. https://doi.org/http://dx.doi.org/10.1016/S0022-5096(97)00075-6

Bernardi, D., Pawlikowski, E., Newman, J., 1985. A General Energy Balance for Battery Systems. J. Electrochem. Soc. 132, 5. https://doi.org/10.1149/1.2113792

Billon, N., 2012. New constitutive modeling for time-dependent mechanical behavior of polymers close to glass transition: Fundamentals and experimental validation. J. Appl. Polym. Sci. 125, 4390–4401. https://doi.org/https://doi.org/10.1002/app.36598

Bodner, S.R., Partom, Y., 1975. Constitutive Equations for Elastic-Viscoplastic Strain-Hardening Materials. J. Appl. Mech. 42, 385–389. https://doi.org/10.1115/1.3423586

Boyce, M.C., Parks, D.M., Argon, A.S., 1988. Large inelastic deformation of glassy polymers. part I: rate dependent constitutive model. Mech. Mater. 7, 15–33. https://doi.org/10.1016/0167-6636(88)90003-8

Brooks, N.W.J., Duckett, R.A., Ward, I.M., 1998. Temperature and strain-rate dependence of yield stress of polyethylene. J. Polym. Sci. Part B Polym. Phys. 36, 2177–2189. https://doi.org/10.1002/(SICI)1099-0488(19980915)36:12<2177::AID-POLB15>3.0.CO;2-X

Callister, W., Rethwisch, D., 1996. Materials Science and Engineering. John Wiley & Sons, Inc.

Cantournet, S., Desmorat, R., Besson, J., 2009. Mullins effect and cyclic stress softening of filled elastomers by internal sliding and friction thermodynamics model. Int. J. Solids Struct. 46, 2255–2264. https://doi.org/10.1016/J.IJSOLSTR.2008.12.025

Cayzac, H.A., Saï, K., Laiarinandrasana, L., 2013. Damage based constitutive relationships in semi-crystalline polymer by using multi-mechanisms model. Int. J. Plast. 51, 47–64. https://doi.org/10.1016/j.ijplas.2013.06.008

Chaboche, J., 1997. APPLICATION TO THE VISCOPLASTICITY AND. Int. J. Solids Struct. 34, 2239–2254. https://doi.org/10.1016/S0020-7683(96)00162-X

Chaboche, J.L., 1981. Continuous damage mechanics - A tool to describe phenomena before crack initiation. Nucl. Eng. Des. 64, 233–247. https://doi.org/10.1016/0029-5493(81)90007-8

Chen, J., Sun, T., Qi, Y., Li, X., 2014a. A Coupled Penetration-Tension Method for Evaluating the Reliability of Battery Separators. ECS Electrochem. Lett. 3.

Chen, J., Yan, Y., Sun, T., Qi, Y., Li, X., 2014b. Deformation and fracture behaviors of microporous polymer separators for lithium ion batteries. RSC Adv. 4, 14904–14914. https://doi.org/10.1039/c4ra00983e

Chen, S.C., Wan, C.C., Wang, Y.Y., 2005. Thermal analysis of lithium-ion batteries 140, 111–124. https://doi.org/10.1016/j.jpowsour.2004.05.064

Chen, X., Xu, W., Xiao, J., Engelhard, M.H., Ding, F., Mei, D., Hu, D., Zhang, Jian, Zhang, Ji-guang, 2012. Effects of cell positive cans and separators on the performance of high-voltage Li-ion batteries 213, 160–168. https://doi.org/10.1016/j.jpowsour.2012.04.009

Chen, Y., Evans, J.W., 1996. Thermal Analysis of Lithium-Ion Batteries 143, 2708–2712.

Chen, Y., Evans, J.W., 1994. Three-Dimensional Thermal Modeling of Lithium-Polymer Batteries under Galvanostatic Discharge and Dynamic Power Profile 141.

Chow, C.L., Wang, J., 1988. Ductile fracture characterization with an anisotropic continuum damage theory. Eng. Fract. Mech. 30, 547–563. https://doi.org/10.1016/0013-7944(88)90150-6

Chow, C.L., Wang, J., 1987. An anisotropic theory of continuum damage mechanics for ductile fracture. Eng. Fract. Mech. 27, 547–558. https://doi.org/10.1016/0013-7944(87)90108-1

Chow, C.L., Yang, X.J., 2002. A generalized mixed kinematic-isotropic hardening plastic model coupled with anisotropic damage for sheet metal forming. ASME Int. Mech. Eng. Congr. Expo. Proc. 13, 37–44. https://doi.org/10.1115/IMECE2002-33019

Chow, C.L., Yang, X.J., Chu, E., 2001. Effect of principal damage plane rotation on anisotropic damage plastic model. Int. J. Damage Mech. 10, 43–55. https://doi.org/10.1106/6ENW-PLMH-M20N-5TP6

Chow, C.L., Yu, L.G., Demeri, M.Y., 1997. A Unified Damage Approach for Predicting Forming Limit Diagrams. J. Eng. Mater. Technol. 119, 346–353. https://doi.org/10.1115/1.2812269

Chowdhury, K.A., Benzerga, A.A., Talreja, R., 2008. A computational framework for analyzing the dynamic response of glassy polymers. Comput. Methods Appl. Mech. Eng. 197, 4485–4502. https://doi.org/10.1016/J.CMA.2008.07.008

Colak, O.U., 2005. Modeling deformation behavior of polymers with viscoplasticity theory based on overstress. Int. J. Plast. 21, 145–160. https://doi.org/http://dx.doi.org/10.1016/j.ijplas.2004.04.004

Cordebois, J.P., Sidoroff, F., 1982a. Damage Induced Elastic Anisotropy BT - Mechanical Behavior of Anisotropic Solids / Comportment Méchanique des Solides Anisotropes, in: Boehler, J.-P. (Ed.), . Springer Netherlands, Dordrecht, pp. 761–774.

Cordebois, J.P., Sidoroff, F., 1982b. Endommagement anisotrope en élasticité et plasticité. J. Mécanique Appliquée 45–60.

Costa, C.M., Silva, M.M., Lanceros-Méndez, S., 2013. Battery separators based on vinylidene fluoride (VDF) polymers and copolymers for lithium ion battery applications. RSC Adv. 3, 11404–11417. https://doi.org/10.1039/c3ra40732b

Djian, D., Alloin, F., Martinet, S., Lignier, H., Sanchez, J.Y., 2007. Lithium-ion batteries with high charge rate capacity: Influence of the porous separator. J. Power Sources 172, 416–421.

https://doi.org/10.1016/j.jpowsour.2007.07.018

Doyle, M., Fuller, T.F., Newman, J., 1993. Modeling of Galvanostatic Charge and Discharge of the Lithium / Polymer / Insertion Cell 140, 1526–1533.

Doyle, M., Newman, J., 1996. Comparison of Modeling Predictions with Experimental Data from Plastic Lithium Ion Cells Comparison of Modeling Predictions with Experimental Data from Plastic Lithium Ion Cells.

Drake, S.J., Wetz, D.A., Ostanek, J.K., Miller, S.P., Heinzel, J.M., Jain, A., 2014. Measurement of anisotropic thermophysical properties of cylindrical Li-ion cells. J. Power Sources 252, 298–304. https://doi.org/10.1016/j.jpowsour.2013.11.107

Drozdov, A.D., 2009. Mullins' effect in semicrystalline polymers. Int. J. Solids Struct. 46, 3336–3345. https://doi.org/http://dx.doi.org/10.1016/j.ijsolstr.2009.05.001

Drozdov, A.D., Gupta, R.K., 2003. Constitutive equations in finite viscoplasticity of semicrystalline polymers. Int. J. Solids Struct. 40, 6217–6243. https://doi.org/http://dx.doi.org/10.1016/S0020-7683(03)00414-1

Dunn, B., Kamath, H., Tarascon, J., 2011. for the Grid : A Battery of Choices 334, 928–936.

Dusunceli, N., Colak, O.U., 2008. Modelling effects of degree of crystallinity on mechanical behavior of semicrystalline polymers. Int. J. Plast. 24, 1224–1242. https://doi.org/http://dx.doi.org/10.1016/j.ijplas.2007.09.003

Dusunceli, N., Colak, O.U., 2006. High density polyethylene (HDPE): Experiments and modeling. Mech. Time-Dependent Mater. 10, 331–345. https://doi.org/10.1007/s11043-007-9026-5

El-Qoubaa, Z., Othman, R., 2016. Strain rate sensitivity of polyetheretherketone's compressive yield stress at low and high temperatures. Mech. Mater. 95, 15–27. https://doi.org/10.1016/j.mechmat.2015.12.008

Felder, S., Holthusen, H., Hesseler, S., Pohlkemper, F., Gries, T., Simon, J.W., Reese, S., 2020. Incorporating crystallinity distributions into a thermo-mechanically coupled constitutive model for semi-crystalline polymers. Int. J. Plast. 135, 102751. https://doi.org/10.1016/j.ijplas.2020.102751

Foley, P., Celanese, H., 1993. Development of polyethylene tetrafluoroethylene microporous film for advanced batteries 4, 259–266.

Francis, C.F.J., Kyratzis, I.L., Best, A.S., 2020. Lithium-Ion Battery Separators for Ionic-Liquid Electrolytes : A Review 1904205, 1–22. https://doi.org/10.1002/adma.201904205

Galeski, A., Bartczak, Z., Kazmierczak, T., Slouf, M., 2010. Morphology of undeformed and deformed polyethylene lamellar crystals. Polymer (Guildf). 51, 5780–5787. https://doi.org/10.1016/j.polymer.2010.10.004

Gerssen-Gondelach, S.J., Faaij, A.P.C., 2012. Performance of batteries for electric vehicles on short and longer term. J. Power Sources 212, 111–129. https://doi.org/10.1016/j.jpowsour.2012.03.085

Ghorbel, E., 2008. A viscoplastic constitutive model for polymeric materials. Int. J. Plast. 24, 2032–2058. https://doi.org/http://dx.doi.org/10.1016/j.ijplas.2008.01.003

Gor, G.Y., Cannarella, J., Prévost, J.H., Arnold, C.B., 2014. A Model for the Behavior of Battery Separators in Compression at Different Strain/Charge Rates. J. Electrochem. Soc. 161, F3065–F3071. https://doi.org/10.1149/2.0111411jes

Goutam, S., Nikolian, A., Jaguemont, J., Smekens, J., Omar, N., Van Dan Bossche, P., Van Mierlo, J., 2017. Three-dimensional electro-thermal model of li-ion pouch cell: Analysis and comparison of cell design factors and model assumptions. Appl. Therm. Eng. 126, 796–808. https://doi.org/10.1016/j.applthermaleng.2017.07.206

Govaert, L.E., Timmermans, P.H.M., Brekelmans, W.A.M., 2000. The influence of intrinsic strain softening on strain localization in polycarbonate: Modeling and experimental validation. J. Eng. Mater. Technol. Trans. ASME 122, 177–185. https://doi.org/10.1115/1.482784

Gu, W.B., Wang, C.Y., 2000. Thermal - Electrochemical Modeling of Battery Systems Thermal-Electrochemical Modeling of Battery Systems.

Guo, Q., Zaïri, F., 2020. A physically-based thermo-mechanical model for stretch-induced crystallizable rubbers: Crystallization thermodynamics and chain-network crystallization anisotropy. Int. J. Plast. 131, 102724. https://doi.org/10.1016/j.ijplas.2020.102724

Hammi, Y., Bammann, D.J., Horstemeyer, M.F., 2004. Modeling of Anisotropic Damage for Ductile Materials in Metal Forming Processes. Int. J. Damage Mech. 13, 123–146. https://doi.org/10.1177/1056789504039255

Haward R. N., T.G., 1968. The use of a mathematical model to describe isothermal stress-strain curves in glassy thermoplastics. Proc. R. Soc. London. Ser. A. Math. Phys. Sci. 302, 453–472. https://doi.org/10.1098/rspa.1968.0029

Hill, R., 1948. A theory of the yielding and plastic flow of anisotropic metals. Proc. R. Soc. London. Ser. A. Math. Phys. Sci. 193, 281–297.

Holopainen, S., Barriere, T., Cheng, G., Kouhia, R., 2017. Continuum approach for modeling fatigue in amorphous glassy polymers. Applications to the investigation of damage-ratcheting interaction in polycarbonate. Int. J. Plast. 91, 109–133. https://doi.org/10.1016/j.ijplas.2016.12.001

Huang, X., 2011. Separator technologies for lithium-ion batteries. J. Solid State Electrochem. 15, 649–662. https://doi.org/10.1007/s10008-010-1264-9

Iclodean, C., Varga, B., Burnete, N., Cimerdean, D., Jurchiş, B., 2017. Comparison of Different Battery Types for Electric Vehicles. IOP Conf. Ser. Mater. Sci. Eng. 252.

https://doi.org/10.1088/1757-899X/252/1/012058

Ihm, D., Noh, J., Kim, J., 2002. Effect of polymer blending and drawing conditions on properties of polyethylene separator prepared for Li-ion secondary battery 109, 388–393.

Jeon, D.H., Baek, S.M., 2011. Thermal modeling of cylindrical lithium ion battery during discharge cycle. Energy Convers. Manag. 52, 2973–2981. https://doi.org/10.1016/j.enconman.2011.04.013

Jin, L.W., Lee, P.S., Kong, X.X., Fan, Y., Chou, S.K., 2014. Ultra-thin minichannel LCP for EV battery thermal management. Appl. Energy 113, 1786–1794. https://doi.org/10.1016/j.apenergy.2013.07.013

Jin, S.Y., Manuel, J., Zhao, X., Park, W.H., Ahn, J.H., 2017. Surface-modified polyethylene separator via oxygen plasma treatment for lithium ion battery. J. Ind. Eng. Chem. 45, 15–21. https://doi.org/10.1016/j.jiec.2016.08.021

Johnson, M.B., Wilkes, G.L., 2002a. Microporous membranes of polyoxymethylene from a melt-extrusion process: (II) Effects of thermal annealing and stretching on porosity. J. Appl. Polym. Sci. 84, 1762–1780. https://doi.org/https://doi.org/10.1002/app.10587

Johnson, M.B., Wilkes, G.L., 2002b. Microporous membranes of isotactic poly(4-methyl-1-pentene) from a melt-extrusion process. I. Effects of resin variables and extrusion conditions. J. Appl. Polym. Sci. 83, 2095–2113. https://doi.org/https://doi.org/10.1002/app.10164

Johnson, M.B., Wilkes, G.L., 2001. Microporous membranes of polyoxymethylene from a melt-extrusion process: (I) effects of resin variables and extrusion conditions. J. Appl. Polym. Sci. 81, 2944–2963. https://doi.org/https://doi.org/10.1002/app.1745

Jordan, B., Gorji, M.B., Mohr, D., 2020. Neural network model describing the temperature- And rate-dependent stress-strain response of polypropylene. Int. J. Plast. 135, 102811. https://doi.org/10.1016/j.ijplas.2020.102811

Kachanov, L.M., 1958. Time of the rupture process under creep conditions, Izy Akad. Nank SSR Otd Tech Nauk 8, 26–31.

Kalnaus, S., Kumar, A., Wang, Y., Li, J., Simunovic, S., Turner, J.A., Gorney, P., 2018a. Strain distribution and failure mode of polymer separators for Li-ion batteries under biaxial loading. J. Power Sources 378, 139–145. https://doi.org/10.1016/j.jpowsour.2017.12.029

Kalnaus, S., Wang, Y., Li, J., Kumar, A., Turner, J.A., 2018b. Temperature and strain rate dependent behavior of polymer separator for Li-ion batteries. Extrem. Mech. Lett. 20, 73–80. https://doi.org/10.1016/j.eml.2018.01.006

Kassar, S., Ayoub, G., Kridli, G., 2019. Anisotropic time dependent and continuum damage coupled plasticity model: An application for Mg AZ31B. Int. J. Solids Struct. 178–179, 199–211. https://doi.org/10.1016/j.ijsolstr.2019.07.006

Khan, A., Zhang, H., 2001. Finite deformation of a polymer: experiments and modeling. Int. J. Plast. 17, 1167–1188. https://doi.org/http://dx.doi.org/10.1016/S0749-6419(00)00073-5

Khan, A.S., Huang, S., 1995. Continuum theory of plasticity. John Wiley & Sons.

Kim, K.J., Park, M.S., Yim, T., Yu, J.S., Kim, Y.J., 2014. Electron-beam-irradiated polyethylene membrane with improved electrochemical and thermal properties for lithium-ion batteries. J. Appl. Electrochem. 44, 345–352. https://doi.org/10.1007/s10800-014-0661-7

Kim, Y., Mohan, S., Member, S., Siegel, J.B., Stefanopoulou, A.G., Ding, Y., 2014. The Estimation of Temperature Distribution in Cylindrical Battery Cells Under Unknown Cooling Conditions 22, 2277–2286.

Kim, Y., Siegel, J.B., Stefanopoulou, A.G., 2013. A Computationally Efficient Thermal Model of Cylindrical Battery Cells for the Estimation of Radially Distributed Temperatures.

Kock, L.D., Lekgoathi, M.D.S., Crouse, P.L., Vilakazi, B.M., 2012. Solid state vibrational spectroscopy of anhydrous lithium hexafluorophosphate (LiPF 6). J. Mol. Struct. 1026, 145–149. https://doi.org/10.1016/j.molstruc.2012.05.053

Krairi, A., Doghri, I., 2014. A thermodynamically-based constitutive model for thermoplastic polymers coupling viscoelasticity, viscoplasticity and ductile damage. Int. J. Plast. 60, 163–181. https://doi.org/http://dx.doi.org/10.1016/j.ijplas.2014.04.010

Krairi, A., Doghri, I., Robert, G., 2016. Multiscale high cycle fatigue models for neat and short fiber reinforced thermoplastic polymers. Int. J. Fatigue 92, 179–192. https://doi.org/10.1016/j.ijfatigue.2016.06.029

Krairi, A., Doghri, I., Schalnat, J., Robert, G., Van Paepegem, W., 2019. Thermo-mechanical coupling of a viscoelastic-viscoplastic model for thermoplastic polymers: Thermodynamical derivation and experimental assessment. Int. J. Plast. 115, 154–177. https://doi.org/10.1016/j.ijplas.2018.11.016

Krajcinovic, D., 1985. Continuous damage mechanics revisited: Basic concepts and definitions. J. Appl. Mech. Trans. ASME 52, 829–834. https://doi.org/10.1115/1.3169154

Krempl, E., Khan, F., 2003. Rate (time)-dependent deformation behavior: an overview of some properties of metals and solid polymers. Int. J. Plast. 19, 1069–1095. https://doi.org/http://dx.doi.org/10.1016/S0749-6419(03)00002-0

Kweon, S., Benzerga, A.A., 2013. Finite element implementation of a macromolecular viscoplastic polymer model. Int. J. Numer. Methods Eng. 94, 895–919. https://doi.org/10.1002/nme.4474

Lee, B.J., Argon, A.S., Parks, D.M., Ahzi, S., Bartczak, Z., 1993. Simulation of large strain plastic deformation and texture evolution in high density polyethylene. Polymer (Guildf). 34, 3555–3575. https://doi.org/10.1016/0032-3861(93)90039-D

Lee, B J, Parks, D., Ahzi, S., 1993. Micromechanical modeling of large plastic deformation and

texture evolution in semi-crystalline polymers. J. Mech. Phys. Solids 41, 1651–1687.

Lee, E.H., 1969. Elastic-Plastic Deformation at Finite Strains. J. Appl. Mech. 36, 1–6. https://doi.org/10.1115/1.3564580

Lee, H., Sitapure, N., Hwang, S., Kwon, J.S. Il, 2021. Multiscale modeling of dendrite formation in lithium-ion batteries. Comput. Chem. Eng. 153, 107415. https://doi.org/10.1016/j.compchemeng.2021.107415

Lee, H., Yanilmaz, M., Toprakci, O., Fu, K., Zhang, X., 2014. A review of recent developments in membrane separators for rechargeable lithium-ion batteries. Energy Environ. Sci. 7, 3857–3886. https://doi.org/10.1039/c4ee01432d

Lee, J.H., Ryu, D.M., Lee, C.S., 2020. Constitutive-damage modeling and computational implementation for simulation of elasto-viscoplastic-damage behavior of polymeric foams over a wide range of strain rates and temperatures. Int. J. Plast. 130, 102712. https://doi.org/10.1016/j.ijplas.2020.102712

Lee, Y., Park, J., Jeon, H., Yeon, D., Kim, B.H., Cho, K.Y., Ryou, M.H., Lee, Y.M., 2016. In-depth correlation of separator pore structure and electrochemical performance in lithium-ion batteries. J. Power Sources 325, 732–738. https://doi.org/10.1016/j.jpowsour.2016.06.094

Lemaitre, J., 1994. Damage 90 : a post processor for crack initiation 7825.

Lemaitre, J., 1992. No Title.

Lemaitre, J., 1985. A Continuous Damage Mechanics Model for Ductile Fracture 107, 83–89.

Lin, C., Tang, A., Mu, H., Wang, W., Wang, C., 2015. Aging mechanisms of electrode materials in lithium-ion batteries for electric vehicles. J. Chem. 2015. https://doi.org/10.1155/2015/104673

Lin, X., Perez, H.E., Mohan, S., Siegel, J.B., Stefanopoulou, A.G., Ding, Y., Castanier, M.P., 2014. A lumped-parameter electro-thermal model for cylindrical batteries. J. Power Sources 257, 1–11. https://doi.org/10.1016/j.jpowsour.2014.01.097

Lin, X., Perez, H.E., Siegel, J.B., Stefanopoulou, A.G., Li, Y., Anderson, R.D., Ding, Y., Castanier, M.P., 2012. On-line Parameterization of Lumped Thermal Dynamics in Cylindrical Lithium Ion Batteries for Core Temperature Estimation and Health Monitoring X, 1–11.

Linden, D., Reddy, T.B., 2002. Handbook of batteries third ed.

Ling, Z., Chen, J., Fang, X., Zhang, Z., Xu, T., Gao, X., Wang, S., 2014. Experimental and numerical investigation of the application of phase change materials in a simulative power batteries thermal management system. Appl. Energy 121, 104–113. https://doi.org/10.1016/j.apenergy.2014.01.075

Lu, L., Han, X., Li, J., Hua, J., Ouyang, M., 2013. A review on the key issues for lithium-ion battery management in electric vehicles. J. Power Sources 226, 272–288. https://doi.org/10.1016/j.jpowsour.2012.10.060

Lukic, S.M., Cao, J., Bansal, R.C., Rodriguez, F., Emadi, A., 2008. Energy storage systems for automotive applications. IEEE Trans. Ind. Electron. 55, 2258–2267. https://doi.org/10.1109/TIE.2008.918390

Makki, M., Ayoub, G., Abdul-Hameed, H., Zaïri, F., Mansoor, B., Naït-Abdelaziz, M., Ouederni, M., 2017a. Mullins effect in polyethylene and its dependency on crystal content: A network alteration model. J. Mech. Behav. Biomed. Mater. 75. https://doi.org/10.1016/j.jmbbm.2017.04.022

Makki, M., Ayoub, G., Abdul-Hameed, H., Zaïri, F., Mansoor, B., Naït-Abdelaziz, M., Ouederni, M., 2017b. Mullins effect in polyethylene and its dependency on crystal content: A network alteration model. J. Mech. Behav. Biomed. Mater. 75, 442–454. https://doi.org/10.1016/j.jmbbm.2017.04.022

Makradi, A., Ahzi, S., Gregory, R. V, Edie, D.D., 2005. A two-phase self-consistent model for the deformation and phase transformation behavior of polymers above the glass transition temperature: application to PET. Int. J. Plast. 21, 741–758. https://doi.org/http://dx.doi.org/10.1016/j.ijplas.2004.04.012

Martinez-Cisneros, C., Antonelli, C., Levenfeld, B., Varez, A., Sanchez, J.Y., 2016. Evaluation of polyolefin-based macroporous separators for high temperature Li-ion batteries. Electrochim. Acta 216, 68–78. https://doi.org/10.1016/j.electacta.2016.08.105

Miao, Y., Yokochi, A., 2019. Current Li-Ion Battery Technologies in Electric. https://doi.org/10.3390/en12061074

Nguyen, V.D., Lani, F., Pardoen, T., Morelle, X.P., Noels, L., 2016. A large strain hyperelastic viscoelastic-viscoplastic-damage constitutive model based on a multi-mechanism non-local damage continuum for amorphous glassy polymers. Int. J. Solids Struct. 96, 192–216. https://doi.org/10.1016/j.ijsolstr.2016.06.008

Oh, K.Y., Epureanu, B.I., 2016. A novel thermal swelling model for a rechargeable lithium-ion battery cell. J. Power Sources 303, 86–96. https://doi.org/10.1016/j.jpowsour.2015.10.085

Oh, K.Y., Epureanu, B.I., Siegel, J.B., Stefanopoulou, A.G., 2016. Phenomenological force and swelling models for rechargeable lithium-ion battery cells. J. Power Sources 310, 118–129. https://doi.org/10.1016/j.jpowsour.2016.01.103

Olszanski, T., Zanardelli, S., Peck, S., Pierce, M., 2012. Validation of a Thermal-Electric Li-Ion Battery Model. SAE Int. J. Passeng. Cars - Electron. Electr. Syst. 5, 154–163. https://doi.org/https://0-doi-org.wizard.umd.umich.edu/10.4271/2012-01-0332

Onda, K., Ohshima, T., Nakayama, M., Fukuda, K., Araki, T., 2006. Thermal behavior of small lithium-ion battery during rapid charge and discharge cycles 158, 535–542.

https://doi.org/10.1016/j.jpowsour.2005.08.049

Pampillo, C.A., Davis, L.A., 1972. Temperature dependence of the yield and flow stresses of linear high-molecular-weight polyethylene. J. Appl. Phys. 43, 4277–4285. https://doi.org/doi:http://dx.doi.org/10.1063/1.1660917

Pan, Z., Zhu, J., Xu, H., Sedlatschek, T., Zhang, X., Li, W., Gao, T., Xia, Y., Wierzbicki, T., 2020. Microstructural deformation patterns of a highly orthotropic polypropylene separator of lithium-ion batteries: Mechanism, model, and theory. Extrem. Mech. Lett. 37, 100705. https://doi.org/10.1016/j.eml.2020.100705

Parks, D.M., Ahzi, S., 1990. Polycrystalline plastic deformation and texture evolution for crystals lacking five independent slip systems. J. Mech. Phys. Solids 38, 701–724. https://doi.org/10.1016/0022-5096(90)90029-4

Peabody, C., Arnold, C.B., 2011. The role of mechanically induced separator creep in lithium-ion battery capacity fade. J. Power Sources 196, 8147–8153. https://doi.org/10.1016/j.jpowsour.2011.05.023

Peacock, A.J., 2000. Handbook of polyethylene : structures, properties, and applications. Andrew J. Peacock., Plastics engineering: 57. New York : Marcel Dekker, [2000].

Pesaran, A.A., Kim, G.H., Keyser, M., 2009. Integration issues of cells into battery packs for plug-in and hybrid electric vehicles. 24th Int. Batter. Hybrid Fuel Cell Electr. Veh. Symp. Exhib. 2009, EVS 24 3, 1924–1930.

Plaimer, M., Breitfuß, C., Sinz, W., Heindl, S.F., Ellersdorfer, C., Steffan, H., Wilkening, M., Hennige, V., Tatschl, R., Geier, A., Schramm, C., Freunberger, S.A., 2016. Evaluating the trade-off between mechanical and electrochemical performance of separators for lithium-ion batteries: Methodology and application. J. Power Sources 306, 702–710. https://doi.org/10.1016/j.jpowsour.2015.12.047

Pyrz, F., Zairi, M., 2007. Identification of viscoplastic parameters of phenomenological constitutive equations for polymers by deterministic and evolutionary approach. Model. Simul. Mater. Sci. Eng. 15, 85.

Rabotnov, Y., 1969. Creep problems in structural members.

Rae, P.J., Brown, E.N., Orler, E.B., 2007. The mechanical properties of poly(ether-ether-ketone) (PEEK) with emphasis on the large compressive strain response. Polymer (Guildf). 48, 598–615. https://doi.org/10.1016/j.polymer.2006.11.032

Ramadass, P., Haran, B., White, R., Popov, B.N., 2002. Capacity fade of Sony 18650 cells cycled at elevated temperatures Part I . Cycling performance 112, 606–613.

Ramadesigan, V., Northrop, P.W.C., De, S., Santhanagopalan, S., Braatz, R.D., Subramanian, V.R., 2012. Modeling and Simulation of Lithium-Ion Batteries from a Systems Engineering Perspective. J. Electrochem. Soc. 159, R31–R45. https://doi.org/10.1149/2.018203jes

Regrain, C., Laiarinandrasana, L., Toillon, S., Saï, K., 2009. Multi-mechanism models for semi-crystalline polymer: Constitutive relations and finite element implementation. Int. J. Plast. 25, 1253–1279. https://doi.org/http://dx.doi.org/10.1016/j.ijplas.2008.09.010

Rethwisch, W.D., 2010. Callister, Materials Science and Engineering.

Richeton, J., Ahzi, S., Vecchio, K.S., Jiang, F.C., Adharapurapu, R.R., 2006. Influence of temperature and strain rate on the mechanical behavior of three amorphous polymers: Characterization and modeling of the compressive yield stress. Int. J. Solids Struct. 43, 2318–2335. https://doi.org/10.1016/j.ijsolstr.2005.06.040

Richeton, J, Ahzi, S., Vecchio, K.S., Jiang, F.C., Adharapurapu, R.R., 2006. Influence of temperature and strain rate on the mechanical behavior of three amorphous polymers: Characterization and modeling of the compressive yield stress. Int. J. Solids Struct. 43, 2318–2335. https://doi.org/http://dx.doi.org/10.1016/j.ijsolstr.2005.06.040

Rosso, M., Gobron, T., Brissot, C., Chazalviel, J.N., Lascaud, S., 2001. Onset of dendritic growth in lithium/polymer cells. J. Power Sources 97–98, 804–806. https://doi.org/10.1016/S0378-7753(01)00734-0

Şerban, D.A., Weber, G., Marşavina, L., Silberschmidt, V. V., Hufenbach, W., 2013. Tensile properties of semi-crystalline thermoplastic polymers: Effects of temperature and strain rates. Polym. Test. 32, 413–425. https://doi.org/10.1016/j.polymertesting.2012.12.002

Sheidaei, A., Xiao, X., Huang, X., Hitt, J., 2011. Mechanical behavior of a battery separator in electrolyte solutions. J. Power Sources 196, 8728–8734. https://doi.org/10.1016/j.jpowsour.2011.06.026

Shi, D., Xiao, X., Huang, X., Kia, H., 2011. Modeling stresses in the separator of a pouch lithium-ion cell. J. Power Sources 196, 8129–8139. https://doi.org/10.1016/j.jpowsour.2011.05.026

Shojaei, A., Li, G., 2013. Viscoplasticity analysis of semicrystalline polymers: A multiscale approach within micromechanics framework. Int. J. Plast. 42, 31–49. https://doi.org/http://dx.doi.org/10.1016/j.ijplas.2012.09.014

Shojaei, A.K., Volgers, P., 2017. Fatigue damage assessment of unfilled polymers including self-heating effects. Int. J. Fatigue 100, 367–376. https://doi.org/10.1016/j.ijfatigue.2017.03.017

Shojaei, A.K., Wedgewood, A.R., 2017. An anisotropic cyclic plasticity, creep and fatigue predictive tool for unfilled polymers. Mech. Mater. 106, 20–34. https://doi.org/10.1016/j.mechmat.2017.01.003

Sidoroff, F., 1981. Description of Anisotropic Damage Application to Elasticity BT - Physical Non-Linearities in Structural Analysis, in: Hult, J., Lemaitre, J. (Eds.), . Springer Berlin Heidelberg, Berlin, Heidelberg, pp. 237–244.

Smith, K.A., Rahn, C.D., Wang, C., 2008. Model Order Reduction of 1D 130, 1–8. https://doi.org/10.1115/1.2807068

Smith, K.A., Rahn, C.D., Wang, C., 2007. Control oriented 1D electrochemical model of lithium ion battery 48, 2565–2578. https://doi.org/10.1016/j.enconman.2007.03.015

Song, M., Hu, Y., Choe, S., 2020. Analysis of the Heat Generation Rate of Lithium-Ion Battery Using an Electrochemical Thermal Model Analysis of the Heat Generation Rate of Lithium-Ion Battery Using an Electrochemical Thermal Model. https://doi.org/10.1149/1945-7111/aba96b

Srinivasan, V., Wang, C.Y., 2003. Analysis of Electrochemical and Thermal Behavior of Li-Ion Cells 98–106. https://doi.org/10.1149/1.1526512

Stringfellow, R.G., Parks, D.M., Olson, G.B., 1992. A constitutive model for transformation plasticity accompanying strain-induced martensitic transformations in metastable austenitic steels. Acta Metall. Mater. 40, 1703–1716.

Timmons, A., Dahn, J.R., 2007. Isotropic Volume Expansion of Particles of Amorphous Metallic Alloys in Composite Negative Electrodes for Li-Ion Batteries. J. Electrochem. Soc. 154, A444. https://doi.org/10.1149/1.2711075

van Dommelen, J.A.W., Parks, D.M., Boyce, M.C., Brekelmans, W.A.M., Baaijens, F.P.T., 2003. Micromechanical modeling of the elasto-viscoplastic behavior of semi-crystalline polymers. J. Mech. Phys. Solids 51, 519–541. https://doi.org/http://dx.doi.org/10.1016/S0022-5096(02)00063-7

Vetter, J., Novák, P., Wagner, M.R., Veit, C., Möller, K.C., Besenhard, J.O., Winter, M., Wohlfahrt-Mehrens, M., Vogler, C., Hammouche, A., 2005. Ageing mechanisms in lithium-ion batteries. J. Power Sources 147, 269–281. https://doi.org/10.1016/j.jpowsour.2005.01.006

Voyiadjis, G.Z., Kattan, P.I., 2006. Chapter 6 - Damage and plasticity in metals, in: Voyiadjis, G.Z., Kattan, P.I.B.T.-A. in D.M. (Second E. (Eds.), . Elsevier Science Ltd, Oxford, pp. 109–158. https://doi.org/https://doi.org/10.1016/B978-008044688-2/50007-2

Voyiadjis, G.Z., Kattan, P.I., 1999. Damage and Plasticity in Metals. Adv. Damage Mech. Met. Met. Matrix Compos. 109–157. https://doi.org/10.1016/B978-0-08-043601-2.50011-8

Voyiadjis, G.Z., Kattan, P.I., 1992. A plasticity-damage theory for large deformation of solids-I. Theoretical formulation. Int. J. Eng. Sci. 30, 1089–1108. https://doi.org/10.1016/0020-7225(92)90059-P

Voyiadjis, G.Z., Shojaei, A., Li, G., 2012. A generalized coupled viscoplastic-viscodamage-viscohealing theory for glassy polymers. Int. J. Plast. 28, 21–45. https://doi.org/10.1016/j.ijplas.2011.05.012

Wang, J., Purewal, J., Liu, P., Hicks-garner, J., Soukazian, S., Sherman, E., Sorenson, A., Vu, L., Tataria, H., Verbrugge, M.W., 2014. Degradation of lithium ion batteries employing graphite negatives and nickel e cobalt e manganese oxide þ spinel manganese oxide positives : Part 1 , aging mechanisms and life estimation. J. Power Sources 269, 937–948.

https://doi.org/10.1016/j.jpowsour.2014.07.030

Wang, Q., Mao, B., Stoliarov, S.I., Sun, J., 2019. A review of lithium ion battery failure mechanisms and fire prevention strategies. Prog. Energy Combust. Sci. 73, 95–131. https://doi.org/10.1016/j.pecs.2019.03.002

Wang, Q., Ping, P., Zhao, X., Chu, G., Sun, J., Chen, C., 2012. Thermal runaway caused fire and explosion of lithium ion battery. J. Power Sources 208, 210–224. https://doi.org/10.1016/j.jpowsour.2012.02.038

Weber, C.J., Geiger, S., Falusi, S., 2015. Material review of Li ion battery separators Material Review of Li Ion Battery Separators 66. https://doi.org/10.1063/1.4878480

Wu, P.D., van der Giessen, E., 1996. Computational Aspects of Localized Deformations in Amorphous Glassy Polymers. Eur. J. Mech. A/Solids 15, 799–823.

Wu, P.D., van der Giessen, E., 1993. On large-strain inelastic torsion of glassy polymers. Int. J. Mech. Sci. 35, 935–951. https://doi.org/https://doi.org/10.1016/0020-7403(93)90031-O

Wu, P.D., Van Der Giessen, E., 1993. On improved network models for rubber elasticity and their applications to orientation hardening in glassy polymers. J. Mech. Phys. Solids 41, 427–456. https://doi.org/10.1016/0022-5096(93)90043-F

Xiao, X., Wu, W., Huang, X., 2010. A multi-scale approach for the stress analysis of polymeric separators in a lithium-ion battery. J. Power Sources 195, 7649–7660. https://doi.org/10.1016/j.jpowsour.2010.06.020

Xing, L., 2018. Stability of Polymeric Separators in Lithium Metal Battery under Low Voltage. https://doi.org/10.1039/C7TA11259A

Xu, H., Zhu, M., Marcicki, J., Yang, X.G., 2017. Mechanical modeling of battery separator based on microstructure image analysis and stochastic characterization. J. Power Sources 345, 137–145. https://doi.org/10.1016/j.jpowsour.2017.02.002

Xu, J., Wang, L., Guan, J., Yin, S., 2016. Coupled effect of strain rate and solvent on dynamic mechanical behaviors of separators in lithium ion batteries. Mater. Des. 95, 319–328. https://doi.org/10.1016/j.matdes.2016.01.082

Xu, M., Zhang, Z., Wang, X., Jia, L., Yang, L., 2015. A pseudo three-dimensional electrochemical-thermal model of a prismatic LiFePO4 battery during discharge process. Energy 80, 303–317. https://doi.org/10.1016/j.energy.2014.11.073

Xu, W., Wang, J., Ding, F., Chen, X., Nasybulin, E., Zhang, Y., Zhang, J.G., 2014. Lithium metal anodes for rechargeable batteries. Energy Environ. Sci. 7, 513–537. https://doi.org/10.1039/c3ee40795k

Yang, P., Tarascon, J., 2012. Towards systems materials engineering. Nat. Mater. 11. https://doi.org/10.1038/nmat3367

Ye, Y., Shi, Y., Cai, N., Lee, J., He, X., 2012. Electro-thermal modeling and experimental validation for lithium ion battery. J. Power Sources 199, 227–238. https://doi.org/10.1016/j.jpowsour.2011.10.027

Yuksel, T., Michalek, J., 2012. Development of a Simulation Model to Analyze the Effect of Thermal Management on Battery Life. https://doi.org/10.4271/2012-01-0671

Zaïri, F., Naït-Abdelaziz, M., Gloaguen, J.M., Lefebvre, J.M., 2008. Modelling of the elasto-viscoplastic damage behaviour of glassy polymers. Int. J. Plast. 24, 945–965. https://doi.org/http://dx.doi.org/10.1016/j.ijplas.2007.08.001

Zaïri, F., Naït-Abdelaziz, M., Woznica, K., Gloaguen, J.-M., 2005a. Constitutive equations for the viscoplastic-damage behaviour of a rubber-modified polymer. Eur. J. Mech. - A/Solids 24, 169–182. https://doi.org/http://dx.doi.org/10.1016/j.euromechsol.2004.11.003

Zaïri, F., Woznica, K., Naït-Abdelaziz, M., 2005b. Phenomenological nonlinear modelling of glassy polymers. Comptes Rendus Mécanique 333, 359–364. https://doi.org/http://dx.doi.org/10.1016/j.crme.2005.02.003

Zhang, C., Moore, I.D., 1997. Nonlinear mechanical response of high density polyethylene. Part II: Uniaxial constitutive modeling. Polym. Eng. Sci. 37, 414–420. https://doi.org/https://doi.org/10.1002/pen.11684

Zhang, S.S., 2007. A review on the separators of liquid electrolyte Li-ion batteries. J. Power Sources 164, 351–364. https://doi.org/10.1016/j.jpowsour.2006.10.065

Zhang, X., Sahraei, E., Wang, K., 2016a. Li-ion Battery Separators, Mechanical Integrity and Failure Mechanisms Leading to Soft and Hard Internal Shorts. Sci. Rep. 6, 1–9. https://doi.org/10.1038/srep32578

Zhang, X., Sahraei, E., Wang, K., 2016b. Deformation and failure characteristics of four types of lithium-ion battery separators. J. Power Sources 327, 693–701. https://doi.org/10.1016/j.jpowsour.2016.07.078

Zhang, X., Sastry, A.M., Shyy, W., 2008. Intercalation-Induced Stress and Heat Generation within Single Lithium-Ion Battery Cathode Particles. J. Electrochem. Soc. 155, A542. https://doi.org/10.1149/1.2926617

Zhang, X., Shyy, W., Marie Sastry, A., 2007. Numerical Simulation of Intercalation-Induced Stress in Li-Ion Battery Electrode Particles. J. Electrochem. Soc. 154, A910. https://doi.org/10.1149/1.2759840

Zhang, X., Zhu, J., Sahraei, E., 2017a. Degradation of battery separators under charge-discharge cycles. RSC Adv. 7, 56099–56107. https://doi.org/10.1039/c7ra11585g

Zhang, X., Zhu, J., Sahraei, E., 2017b. Degradation of battery separators under charge-discharge cycles. RSC Adv. 7, 56099–56107. https://doi.org/10.1039/c7ra11585g

Zhu, J., Zhang, X., Luo, H., Sahraei, E., 2018. Investigation of the deformation mechanisms of lithium-ion battery components using in-situ micro tests. Appl. Energy 224, 251–266. https://doi.org/10.1016/j.apenergy.2018.05.007